COMPUTATIONAL COST REDUCTION OF ROBUST CONTROLLERS FOR ACTIVE MAGNETIC BEARING SYSTEMS

ALICAN SAHINKAYA

Bachelor of Science in Mechanical Engineering

Koç University

January 2013

Master of Science in Mechatronics

University of Bath

November 2014

submitted in partial fulfillment of requirements for the degree

DOCTOR OF PHILOSOPHY IN MECHANICAL ENGINEERING

at the

CLEVELAND STATE UNIVERSITY

AUGUST 2020

We hereby approve this dissertation for
ALICAN SAHINKAYA
Candidate for the Doctor of Philosophy in Engineering degree
for the Department of Mechanical Engineering and
CLEVELAND STATE UNIVERSITY'S
College of Graduate Studies by

Jerzy T. Sawicki, Ph.D., Committee Chair
Department of Mechanical Engineering, 06/16/2020

Hanz Richter, Ph.D.
Department of Mechanical Engineering, 06/16/2020

Dan Simon, Ph.D.
Department of Electrical Engineering and Computer Science, 06/17/2020

Lili Dong, Ph.D.
Department of Electrical Engineering and Computer Science, 06/17/2020

Petru S. Fodor, Ph.D.
Department of Physics, 06/17/2020

Student's Date of Defense: June 4, 2020

This student has fulfilled all requirements for the
Doctor of Philosophy in Engineering degree

Chandra Kothapalli, Ph.D., Doctoral Program Director, 06/18/2020

ACKNOWLEDGEMENT

I would like to express my deepest appreciation to my advisor, Dr. Jerzy T. Sawicki, who has continuously provided support and guidance during my time at Cleveland State University. I have grown both as an engineer and as a person thanks to your dedication to your students. I am forever grateful to have you as my advisor. I would also like to extend my gratitude to my defense committee for the valuable feedback they provided.

I am also grateful for the lab members I had a chance to work with over the years who made the journey less painful. I learnt a lot from their way of doing things and the path they follow in addressing problems.

COMPUTATIONAL COST REDUCTION OF ROBUST CONTROLLERS FOR ACTIVE MAGNETIC BEARING SYSTEMS

ALICAN SAHINKAYA

ABSTRACT

This work developed strategies for reducing the computational complexity of implementing robust controllers for active magnetic bearing (AMB) systems and investigated the use of a novel add-on controller for gyroscopic effect compensation to improve achievable performance with robust controllers.

AMB systems are multi-input multi-output (MIMO) systems with many interacting mechanisms that needs to fulfill conflicting performance criteria. That is why robust control techniques are a perfect application for AMB systems as they provide systematic methods to address both robustness and performance objectives. However, robust control techniques generally result in high order controllers that require high-end control hardware for implementation. Such controllers are not desirable by industrial AMB vendors since their hardware is based on embedded systems with limited bandwidths. That is why the computational cost is a major obstacle towards industry adaptation of robust controllers.

Two novel strategies are developed to reduce the computational complexity of single-rate robust controllers while preserving robust performance. The first strategy identifies a dual-rate configuration of the controller for implementation. The selection of the dual-rate configuration uses the worst-case plant analysis and a novel approach that identifies the largest tolerable perturbations to the controller. The second strategy aims to redesign

the controller by identifying and removing negligible channels in the context of robust performance via the largest tolerable perturbations to the controller. The developed methods are demonstrated both in simulation and experiment using three different AMB systems, where significant computational savings are achieved without degrading the performance.

To improve the achievable performance with robust controllers, a novel add-on controller is developed to compensate the gyroscopic effects in flexible rotor-AMB systems via modal feedback control. The compensation allows for relaxing the robustness requirements in the control problem formulation, potentially enabling better performance. The effectiveness of the developed add-on controller is demonstrated experimentally on two AMB systems with different rotor configurations. The effects of the presence of the add-on controller on the performance controller design is investigated for one of the AMB systems. Slight performance improvements are observed at the cost of increased power consumption and increased computational complexity.

TABLE OF CONTENTS

LIST OF FIGURES

LIST OF TABLES

CHAPTER I

INTRODUCTION

1.1 Background and Motivation

Active magnetic bearings (AMBs) are mechatronic devices that require feedback controllers to support or levitate rotors via attractive electromagnetic forces. They are an alternative to conventional bearings, such as ball-bearings and fluid-film bearings. Some of the advantages of AMBs over conventional bearings include contact-free support, higher achievable rotational speeds, reduced bearing losses at higher rotational speeds, lower maintenance costs, configurable rotordynamic characteristics, and built-in health condition monitoring capabilities. Due to their various advantages over conventional bearings, they are used in various fields such as medical devices like heart pumps [1], turbomachinery [2-4], or machine tools [5-7]. They also have their disadvantages as well, such as lower load capacity and higher capital investment [8]. However, in most cases, AMBs are an attractive option.

Adequate controllers are necessary for safe and reliable operation of AMB systems. The purpose of the controller is to maintain the rotor in the center of the bearing

clearance while gravity and machine specific operational forces are acting on the rotor. However, the design of such controllers is a challenging task due to the inherent unstable nature of AMBs, nonlinear dynamics of AMB actuators, speed dependence of the rotor dynamics, and non-collocated sensor-actuator pairs. For this reason, the research in the past few decades has focused on model-based robust control techniques to address the challenges in the controller design for AMB systems [9].

Robust control methods have been studied extensively in the literature for AMB system control [10-18], mainly due to their ability to address the control problem in its general form, i.e., specific performance objectives must be met with a controller synthesized from an imperfect model. Among the robust control methods, H_∞/μ control results in highly robust controllers where the theory is highly applicable to complex MIMO systems, such as AMB rotor systems [19]. Furthermore, the parameters of the controller design procedure are precisely the performance specifications, and the controller design procedures involve tuning these specifications to synthesize a feasible controller that achieves an acceptable compromise between performance and robustness. This is a much more direct approach compared to hand-tuning parameters of a proportional-integral-derivative (PID) controller coupled with notch filters and lead-lag filters for phase adjustment, where the relation between the achieved performance and tuning parameters are difficult to derive [20].

Sawicki et al. [21] experimentally demonstrated the advantages of μ-controllers over industry standard PID type controllers by comparing achieved tool-tip compliances on a high-speed machining spindle supported by AMBs. Maslen and Sawicki [19] discussed the rationale behind using μ-controllers where they point-out the potential of the μ-

controllers in providing well-formulated and systematic controller design processes that can enable automated commissioning. Many examples in literature show the superior performance of robust controllers compared to industry-standard PID type controllers, e.g., see [22-24].

Even though the literature shows the superiority of robust control techniques, the industry still relies heavily on PID type controllers due to the complexity of robust controllers. First, the robust controller design requires in-depth mathematical and physical knowledge to formulate and solve the control problem [25]. Moreover, an accurate system model is necessary to design a robust controller. That's why an experienced engineer is essential in the commissioning of AMB systems. Second, the robust controller design techniques result in high-order controllers which have high computational cost, hence require powerful hardware for implementation [26, 27]. The need for powerful hardware increases the cost of the necessary equipment to implement such controllers. These two aspects are the major obstacles towards the adaptation of robust controllers for AMB systems in the industry.

The first aspect has been addressed by the ongoing research on automated commissioning for AMB systems, which involves obtaining a high-fidelity model of the AMB system and designing a robust controller [20]. Lösch [28] presented one of the first works on the systematic identification of AMB systems with a stepwise procedure. The first step in the proposed procedure is to identify the rigid modes via the response of the uncontrolled system to current step inputs. Then, a simple stabilizing controller that does not excite rotors' flexible modes is designed. With the rotor levitated by the simple controller, the open-loop plant model is fully identified via measured transfer functions.

Balini et al. [29] applied predictor-based subspace identification (PBSID) method to obtain a linear model of an AMB system. Gähler et al. [30] presented a linear least squares algorithm to generate a fixed-order and fixed-structure model of AMB systems using experimentally obtained frequency response data. Noshadi et al. [31] casted the AMB model identification problem as a weighted least squares problem using pre-obtained frequency response data and solved the problem using the genetic algorithm. Wroblewski et al. [32] used an optimization algorithm to tune the physical parameters of an AMB system model to match the experimental data, where the parameters to be tuned were determined via engineering judgment. Sahinkaya and Sawicki [33] formulated the system identification problem of AMB systems as a nonlinear least squares optimization problem using a parametrized AMB model in the modal domain and applied their method to an AMB test rig. They used the identified model along with their approach from [34] that automatically tunes the weights used in H_∞ control problem formulation to design a stable and robust controller. The use of H_∞/μ control is a popular approach for automated controller design for AMB systems since they explicitly deal with modeling uncertainties [26]. Jastrzebski et al. [35] implemented a gain-scheduled signal-based H_∞ controllers to an AMB system where the weighting filters in the problem formulation were tuned via genetic algorithm.

The second aspect of using robust controllers, which is also a significant obstacle for industry adaptation of model-based robust controllers for AMBs due to the increase in hardware costs, have not been studied extensively for AMB systems. However, the computational cost of controllers has been a research interest for a very long time due to the limited hardware capabilities [36]. Three main factors are affecting the computational

cost of implementing a controller, i.e., the order of the controller, the state-space realization of the controller, and the algorithms used to perform the matrix-vector algebra. The state-space realization of the controller and the algorithms for the required matrix-vector algebra are closely related since algorithms that can be used heavily depend on the realization of the controller, i.e., the structure of the controller system matrices.

A variety of techniques are presented in the literature to reduce the controller order while preserving the same robustness and performance. Goddard and Glover [37] presented a method to reduce the order of the controller while maintaining the robustness and performance of the closed-loop system by searching within a weighted L_∞ ball of the high-order controller. The method was applied to a HIMAT advanced fighter aircraft model with 8 states. The DK-iteration method was used to design a controller resulting in a controller with 20 states. The controller was reduced to 7 states with the proposed method without losing robust performance. Enns [38] developed a technique to reduce the order of a controller via the use of so-called weighted balanced realization. The idea of the method is to scale the system with weights to give emphasis to relevant dynamics and perform balanced truncation on the scaled system. There are many examples of the application of this approach in the literature on AMB systems, e.g., [39-41], as well as some extensions to the method and it is one of the most popular methods. Dijk et al. [39] used a closed-loop balanced truncation method described in [42] to reduce the order of μ-controllers that were designed for chatter control in a high-speed milling process with an AMB as an actuator positioned close to the cutting end. They designed two controllers for different rotational speed intervals with orders 40 and 36. The orders were reduced to 24 and 16, respectively, with the method. The orders were chosen by iteratively

calculating the achieved μ-values with the reduced controllers. The idea of closed-loop balanced truncation is to determine the states of the controller that has the least effects on the closed-loop dynamics and remove them until an acceptable trade-off between closed-loop performance and controller order is achieved. Fittro and Knospe [40] designed a μ-controller of order 138 to minimize the compliance of a rotor supported by AMBs with an achieved μ-value of 1.00. Then, an iterative balanced truncation procedure was performed where the order of the controller was reduced, and the peak μ-value with the reduced controller was calculated. The procedure reduced the controller order to 26 while achieving a μ-value of 1.03.

The state-space realization of controllers has not been studied in the context of computational cost. However, the topic is slightly trivial, where sparse matrices are preferred to represent the controller system matrices since there exist efficient algorithms for sparse matrix-vector algebra, and discussion on the algorithms can be found in [43-45]. With the sparse matrix-vector algebra algorithms, the computational cost of realizing a controller in terms of the necessary number of multiply-accumulate (MAC) operations becomes proportional to the number of non-zero entries of the controller matrices. Moreover, sparse matrices require a lot less memory to be stored compared to fully populated matrices. That is why an attractive option for controller realization is the modal canonical realization [26]. It is trivial to show that for a digital controller with n states, m inputs and k outputs, the number of non-zero terms in the modal form for $\mathbf{A}$ matrix is between n and $2n$, $\mathbf{B}$ matrix is between m and nm, $\mathbf{C}$ matrix is between k and nk, and $\mathbf{D}$ matrix is between 0 and mk.

Although the computational cost of high-order controllers can be reduced significantly via order reduction techniques, along with employing sparse matrix algebra algorithms, it is highly case dependent. There might be cases where any order reduction might degrade the robustness and performance to unacceptable levels, hence prevent any computational cost reduction.

A different perspective has been the focus of research in the context of the computational cost of controllers for hard disk drives (HDD), where single-rate controllers are implemented as multi-rate controllers [46, 47]. Wu and Tomizuka [48] proposed this idea by using the knowledge that most controllers contain modes that are spread out in a wide range of frequencies. This implies that the modes can be separated into slow and fast modes, and slow modes can be implemented at a slower rate and still provide accurate response. By implementing some of the modes at a slower rate, the necessary matrix-vector algebra at each time step would be reduced uniformly with the help of the interlacing technique, which distributes the algebra for the slow modes to multiple time steps. Bhattacharya and Balas [36] investigated the effects of the dual-rate implementations of single-rate controllers. They developed a framework for closed-loop stability analysis with dual-rate controllers. They compared different decompositions of single-rate controllers into dual-rate controllers and showed the effects via the use of lifting technique described in [49]. López- López et al. [50] proposed a two-stage H_∞ optimization for dual-rate controller design. In their method, the first stage designs the single-rate controller, and the second stage modifies the slow modes to maintain similar closed-loop dynamics.

The literature on the dual-rate implementation of single-rate controllers does not offer much in the analysis of robust performance. That is why two novel methods were developed to determine the closed-loop robust performance with dual-rate implementations. The first method utilized the worst-case plant analysis along with the lifting technique to select the dual-rate configuration that would achieve most computational savings while maintaining the desired robust performance. The second method introduced a novel controller perturbation block that defined bounds on the controller frequency response. The bounds were then used to select the dual-rate configuration. Furthermore, a novel method for redesigning a single-rate controller to achieve computational savings in single-rate implementation was introduced. The method identified negligible channels of MIMO controllers in the context of robust performance using the bounds defined by the controller perturbation block. Then, the controllers were redesigned by removing the dynamics of the negligible channels to reduce the computational cost of the controller while maintaining robust performance. The developed methods were demonstrated on three different AMB systems, both in simulation and experiment. For all three AMB systems, the methods achieved significant computational savings without degrading the performance to unacceptable levels.

In the literature, a common approach to improve the achieved performance and robustness of the system with a given controller is to design an add-on controller to address a specific task, e.g., rejection of periodic disturbance forces and compensation of gyroscopic effects to eliminate the source of instability. The topic of periodic disturbance rejection is studied extensively for AMB systems where repetitive control [51, 52], generalized notch filters [53, 54], and disturbance observers [55, 56] are the primary

considerations. As for the gyroscopic effect compensation, mostly the cross-feedback control introduced by Ahrens and Kucera [57] for rigid rotor-AMB systems is studied in the literature. Hutterer et al. [58] applied the cross-feedback controller idea to cancel-out the gyroscopic effects on tilting mode and eliminated the instability caused by the gyroscopic effects. However, the cross-feedback control, as presented in [57], is not applicable to AMB systems with flexible rotors. That is why a novel add-on controller design strategy for gyroscopic effect compensation was developed in this research with the aim of improving the achievable performance with robust controllers. The compensation of gyroscopic effects reduces the robustness requirements in the robust controller design. In theory, the reduced robustness requirements increase the achievable performance due to the well-known trade-off between robustness and performance. The approach was demonstrated on an AMB test rig with a highly gyroscopic rotor, and the feasibility of the approach was discussed.

1.2 Structure of This Work

Chapter 2 briefly describes the AMB system modeling procedure, along with the models of the AMB systems used in this research. Chapter 3 presents the tools of robust control theory with a focus on the structured singular value μ, describes the computational cost of controllers, reviews the dual-rate implementation of controllers for computational saving, and presents the developed strategies to reduce the computational cost of MIMO model-based robust controllers for AMB systems. Chapter 4 discusses the controller design for the AMB systems used in this research and shows the results of applying the proposed methods for computational savings. Chapter 5 investigates the use

of gyroscopic effect compensation on the controller design procedures and performance. Chapter 6 concludes the work presented in this dissertation research.

CHAPTER II

MODELING OF AMB SYSTEMS

2.1 Overview of AMB System Modeling

Active magnetic bearing (AMB) systems, as defined by ISO [61], consists of a rotor, position sensor, controller, power amplifier, and electromagnets. The controller adjusts the amount of current supplied to each electromagnet using the information provided by position sensors to generate the necessary attractive magnetic forces to levitate and support the rotor. Figure 1 shows the block diagram of an AMB system with the controller, where the solid blocks represent the open-loop AMB system.

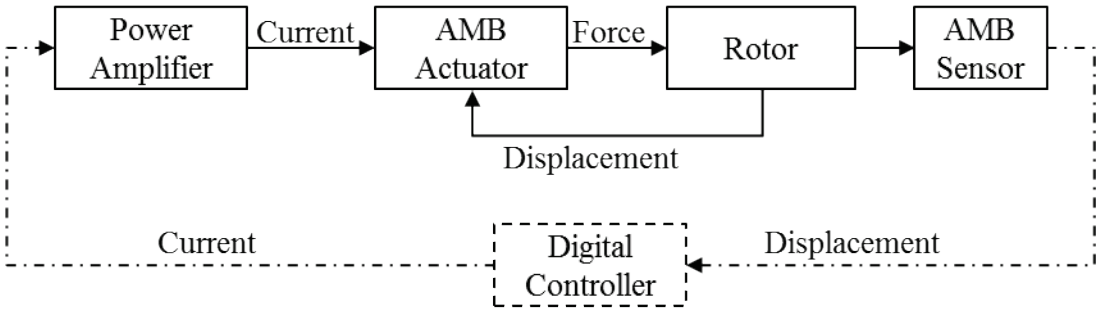

Figure 1: Block diagram of AMB system

2.1.1 Rotor Modeling

A common method to obtain a free-free rotor model is via the finite element method (FEM) [62]. By using FEM, the structure of the rotor is divided into several shaft elements. Each shaft element has two nodes, one at each end of the element, and the disks and bearings can be attached to the shaft at these points. Mathematical descriptions of each element, in terms of mass, stiffness, and gyroscopic matrices, are derived using one of the three beam theories, i.e., Euler-Bernoulli beam theory, Rayleigh beam theory, and Timoshenko beam theory, depending on exclusion or inclusion of rotary inertia and shear effects [62]. Damping is generally hard to model analytically, and modal damping is usually experimentally identified for rotor models.

For the radial dynamics of AMB systems, which was the main consideration in this research, only transverse motions are considered. This results in each node to have four generalized coordinates; transverse displacement in x- and y-directions and rotation about the x- and y-axes, assuming z-axis is the rotation axis. That is why, as the number of shaft elements increases, the order of the resulting model increases as well. Figure 2 shows the degrees of freedom of a shaft element in a single plane. For symmetric rotors, equations describing xz-plane and yz-plane are identical.

Figure 2: Degrees of freedom of a shaft element in a single plane

The mass, stiffness, and gyroscopic matrices for each shaft element can be obtained via any beam theory that is appropriate for a given rotor structure. For slender beams, the Euler-Bernoulli beam offers accurate results. As for relatively thick rotors, the Timoshenko beam theory, which includes the rotary inertia and shear effects that the Euler-Bernoulli beam neglects, is more appropriate. The derivation of the matrices is based on the geometry and material properties of the beam elements. For the exact derivation and equations for the mass, stiffness, and gyroscopic matrices, see [62].

Once the mass, stiffness, and gyroscopic matrices are derived, the state-space model of a rotor can be expressed as shown in (1), where q_{ff} is the vector for the states of the free-free rotor (i.e., position and velocity states of the nodes). A_{ff}, B_{ff}, C_{ff} and G_{ff} are the state-space matrices describing the motion of the free-free rotor in a single plane, where G_{ff} is the gyroscopic matrix to present the gyroscopic effects in the system dynamics. The output matrix C_{ff} is chosen as an identity matrix to have flexibility in defining performance criteria for controller design as well as to ease the process of connecting the rotor model with the other AMB system components. The term Ω is the rotational speed of the rotor. The motion of the rotor in two perpendicular planes, depicted with x and y subscripts, are coupled due to gyroscopic effects. An important effect of gyroscopic coupling is the bifurcation of natural frequencies. The inputs, u_{ff}, to the rotor model are the forces and moments applied at each node. The outputs of the model are the displacements and rotations of each node. That is why it is crucial to choose the shaft elements such that a node is located at every AMB sensor and actuator positions, as well as any point of interest, such as tool locations in an AMB supported spindle.

$$\begin{Bmatrix} \dot{q}_{ff,x} \\ \dot{q}_{ff,y} \end{Bmatrix} = \begin{bmatrix} A_{ff} & -\Omega G_{ff} \\ \Omega G_{ff} & A_{ff} \end{bmatrix} \begin{Bmatrix} q_{ff,x} \\ q_{ff,y} \end{Bmatrix} + \begin{bmatrix} B_{ff} & 0 \\ 0 & B_{ff} \end{bmatrix} \begin{Bmatrix} u_{ff,x} \\ u_{ff,y} \end{Bmatrix} \quad (1)$$

$$\begin{Bmatrix} q_{ff,x} \\ q_{ff,y} \end{Bmatrix} = \begin{bmatrix} C_{ff} & 0 \\ 0 & C_{ff} \end{bmatrix} \begin{Bmatrix} q_{ff,x} \\ q_{ff,y} \end{Bmatrix}$$

Although the procedures are relatively well defined for rotor modeling, the rotor models generally do not match with experimental data due to structurally unknown features and engineering simplifications [63]. That is why either model refinement, which redefines the equations of the model, or model updating, which redefines the parameters of the model, strategies are applied to match the model with experimental data. Generally, model updating strategies are preferred since they do not require exhaustive research campaigns to redefine the physics of a particular model. In rotor model updating, parameters that correspond to structurally ambiguous parts of the rotor, such as shrink fits, tapered fit connections, and multi-layer material parts, are updated via an optimization algorithm. The optimization algorithms use the error between the frequency response of the model and the frequency response data of the physical system as the cost function. Alternatively, a black-box approach can also be used to model the rotor. Sahinkaya and Sawicki [33] used nonlinear least squares optimization to tune a fixed structure modal model to generate the rotor model instead of optimizing the physical parameters that defined the beam elements.

After obtaining a reliable model of the rotor, the order of the model needs to be reduced since high order models pose difficulties for both controller synthesis and simulation studies. For this purpose, the model derived in the nodal domain is converted to the modal domain by a simple change of coordinates via the use of eigenvectors [64].

Then, only the low-frequency modes are kept in the model by truncating the high-frequency modes. Modal truncation is common in rotor dynamics because, generally, only the low-frequency modes are excited in rotor systems [65].

2.1.2 Active Magnetic Bearing Model

Active magnetic bearings (AMBs) are electromagnetic actuators with built-in sensing capabilities. The magnetic field generated by the electromagnet creates an attractive force on the ferromagnetic rotor, regardless of the direction of the current. That is why a second electromagnet is positioned at the opposite side of the rotor to apply forces in both positive and negative directions. These two electromagnets, combined with the relevant position sensors and amplifiers, constitutes a control axis of an AMB. Figure 3 shows a schematic for a single control axis of an AMB.

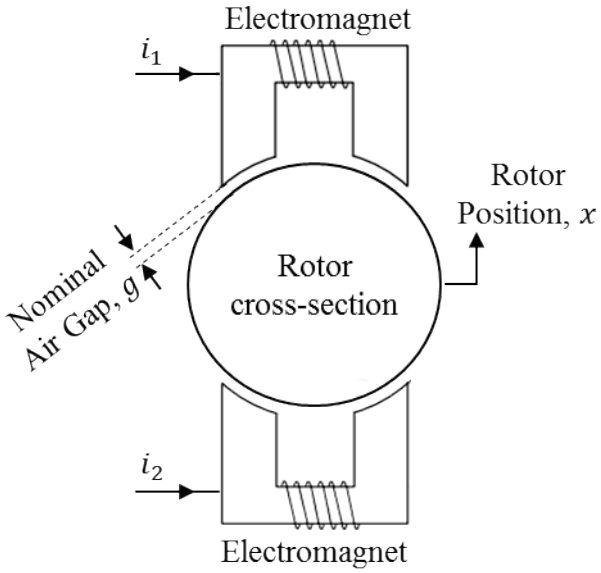

Figure 3: AMB concept in a single axis

The AMB model can be separated into two parts to capture its dynamics, i.e., AMB force model and AMB electronics model. AMB force model relates the current running through the coils to the attractive force applied to the rotor. AMB electronics model defines resistor and inductor dynamics of the AMBs.

The attraction force of the electromagnet is generated at the boundaries of differing permeability, and the magnetic force equation is derived based on the field energy. The magnetic force equation for one AMB axis is a nonlinear function of the rotor position and the currents supplied to each coil, as shown in (2).

$$F = \frac{1}{4}\epsilon\mu_0 N^2 A\cos(\alpha)\left(\frac{i_1^2}{(g-x)^2} - \frac{i_2^2}{(g+x)^2}\right) \tag{2}$$

where

F $= magnetic\ force\ on\ rotor\ [N]$

x $= rotor\ position\ [\mu m]$

g $= nominal\ gap\ [\mu m]$

i_1 $= current\ supplied\ to\ top\ coil\ [A]$

i_2 $= current\ supplied\ to\ bottom\ coil\ [A]$

μ_0 $= permeability\ of\ air\ [N/A^2]$

N $= number\ of\ coil\ windings$

A $= pole\ face\ area\ [\mu m^2]$

α $= pole\ angle [rad]$

ϵ $= derating\ factor$

Equation (2) shows two control inputs, namely i_1 and i_2, are necessary to control a single axis of the AMB. However, this is not desirable since it would complicate the controller design problem. That is why most AMB systems are modeled assuming differential control [26], where a single control current, i_c is added to one coil and subtracted from the opposing coil while a positive bias current, i_b is applied to both coils, i.e., $i_1 = i_b + i_c$ and $i_2 = i_b - i_c$. The block diagram of the differential control is shown in Figure 4 for a single control axis of AMB.

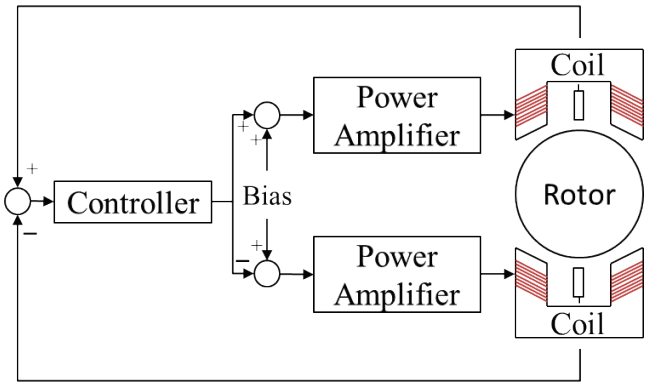

Figure 4: Differential control of an AMB axis

In differential control, the control current magnitude should not exceed the bias current magnitude for the linear force equation to hold. After applying differential control, the magnetic force equation is linearized using Taylor approximation of first order at an operating point, i.e., $x = 0$, $i_b = constant$, to obtain the linear magnetic force equation as shown in Eq. (3).

$$F(x, i_c) = k_x x + k_i i_c \tag{3}$$

In Eq. (3), k_i is the current stiffness in Newton per Amp and k_x is the position stiffness in Newton per micrometer. Both stiffnesses are obtained by the partial derivatives from the Taylor series expansion and have positive values. This means that when the rotor is at the operating point, i.e., $x = 0$ and $i_c = 0$, the rotor remains still since the net force acting on the rotor is zero. However, a small displacement of the rotor would result in a net force along the direction of the displacement; hence AMB systems are unstable without active control.

2.1.3 Position Sensors

A non-contact displacement sensor is integrated with most AMBs to measure the position of the rotor. The bandwidth of the sensors is usually chosen beyond the operational range of the AMB system and can be modeled as a constant gain. However, in the case that the bandwidth is within or close to the bandwidth of the system, a model that represents the dynamics of the sensor is derived, which is usually a second-order low pass filter.

2.1.4 Amplifiers

Each electromagnet in the AMB requires its own power amplifier, which converts the low power control input, usually in the units of Volts, to high power current. The dynamic behavior from the input voltage to output current is referred to as transconductance, or sometimes mutual conductance. Switching amplifiers are the commonly used type of amplifiers for industrial applications due to their lower losses compared to analog amplifiers [66]. The idea of switching amplifiers is that the output

voltage alternately switches between positive and negative voltages V_s, resulting in the current in the coils of the AMBs to alternately increase and decrease. The mean current supplied to coils in a given period is adjusted by adjusting the amount of time the positive voltage is supplied. One of the disadvantages of switching amplifiers comes from the oscillation of the current in the coils, which results in remagnetization losses. The remagnetization losses can be minimized by reducing the switching period [26].

The model for amplifiers for the AMBs generally can be defined as second-order low pass filters. However, since the linear model of AMBs uses only one input per control axis, instead of the physical two inputs per control axis, a single-input-single-output (SISO) amplifier model is used for each AMB control axis by assuming identical behavior. Sometimes the transconductance is identified by defining the current running through the AMB coils as the output current, which then implies the AMB electronics to be part of the amplifier model.

2.1.5 Control Hardware

The control hardware, i.e., the DAC and ADC, introduces time delays to the system model. The time delays can be represented as rational models via Pade approximates.

2.2 AMB System Models

This section provides the models of the AMB systems used in this research. The models include an AMB test rig, a 300 kW turbine generator supported by AMBs, and a high-speed machining (HSM) spindle supported by AMBs.

2.2.1 AMB Test Rig

The experimental AMB test rig manufactured by Revolve Magnetic Bearings Inc., a subsidiary of SKF, is pictured in Figure 5. The test rig consists of a configurable rotor, two identical radial bearings to control the radial position of the rotor, and one thrust bearing to control the axial position of the rotor. The dynamics of radial and axial directions are decoupled, and there is no significant axial load in the system. That is why only radial dynamics were derived for the system. The radial magnetic forces are applied to the rotor at a 45-degree angle due to the structure of radial AMBs, which distributes the gravitational load equally to both axes of control in a single bearing. The radial AMBs are also equipped with rolling element touch-down bearings with a clearance of around 190 μm to provide resting place for the rotor when the AMBs are not powered, as well as to provide safety in case of instability. A flexible coupling element provides the connection between the rotor and brush-type DC motor that drives the system.

Figure 5: AMB Test Rig

The rotor configuration used in this study consisted of two identical radial AMB rotors with laminated surfaces for driven-end (DE) and nondriven-end (NDE) AMBs, one

thrust AMB rotor, two balance disks with 1” and 0.5” thickness, and one coupling element, as shown in Figure 5. The solid shaft is made of stainless steel and had a diameter of 9.525 mm with a length of 457.2 mm. The rotors are attached to the shaft via tapered sleeves. The free-free rotor model was obtained by discretizing the shaft into 36 Timoshenko beam elements and adding the rotor components as lumped masses at their respective nodes. The FE discretization of the rotor is shown in Figure 6, where the elements were chosen to make sure a node corresponded to the connection points of the rotor components, and radial AMB sensor and actuator positions.

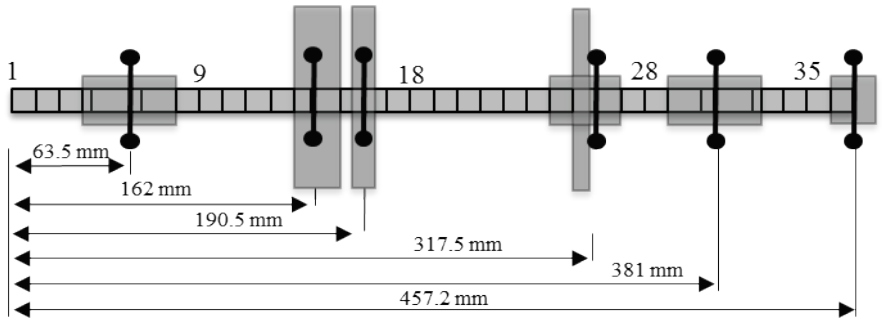

Figure 6: FE discretization of AMB test rig rotor

Since 37 nodes were present in the rotor model, the order of the resulting rotor model was 148 for a single plane and 296 for both planes. This is a high order model that is not convenient for neither controller synthesis nor simulation. That is why the rotor model was reduced via modal truncation to keep the two rigid modes and the lowest four flexible modes in the model. The order was chosen based on the bandwidth of the AMB actuators. The reduced-order modal model of the rotor was of order 24.

The AMB force model was obtained by linearizing the magnetic force equation at an operating point that was the bearing center with 1 A bias current. This yielded the linear

magnetic force equation, which is shown in Eq. (3). The resulting position stiffness and current stiffness values with 1 A bias current were 0.064 N/μm and 25.33 N/A, respectively. The AMB electronics model was embedded in the amplifier model, where the amplifier model was identified experimentally as a second order low pass filter. The sensors of the AMBs were modeled as a constant gain since their bandwidths are beyond the operational region.

The open-loop plant model of the AMB test rig was obtained by appropriately connecting the rotor model, AMB force model, and the amplifier model, which included the dynamics of AMB electronics. The resulting model was a 4-input 4-output 32-order model. Closed-loop system identification described in [20] was performed to extract the open-loop frequency response data from closed-loop measurements with careful design of the excitation signal to validate the model. For this purpose, a simple PID controller to stabilize the system and a pseudorandom binary sequence (PRBS) signal as the excitation signal was designed.

Figure 7 shows the frequency response comparison of the model and experimental data in the nonrotating case, after manually tuning the model to match the experimental data. There are some differences between the model and data, such as the dynamic coupling between the x-axis and the y-axis. However, the difference can be covered by assigning relatively low magnitude uncertainties to the parameters of the model. The discrepancies can be explained by the neglected dynamics, e.g., the cross-coupling stiffness introduced by the coupling element. Figure 8 shows the frequency response comparison of the model and experimental data at 3,000 rpm case to show the model captures the dynamics related to gyroscopic effects. The bifurcation of flexible mode

frequencies of the model closely matches the experimental data, indicating the accuracy of the modeled gyroscopic matrix. That is why the model is acceptable for both controller synthesis and simulation study. Due to the symmetry of the rotor, the y-axis outputs are not shown.

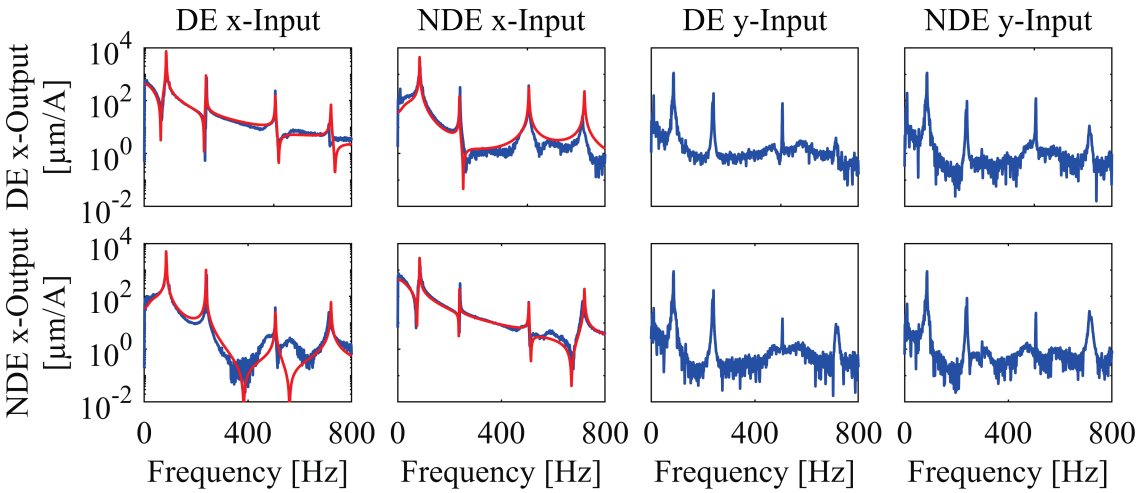

Figure 7: Comparison of model response (red) and open-loop FRD (blue), 0 rpm

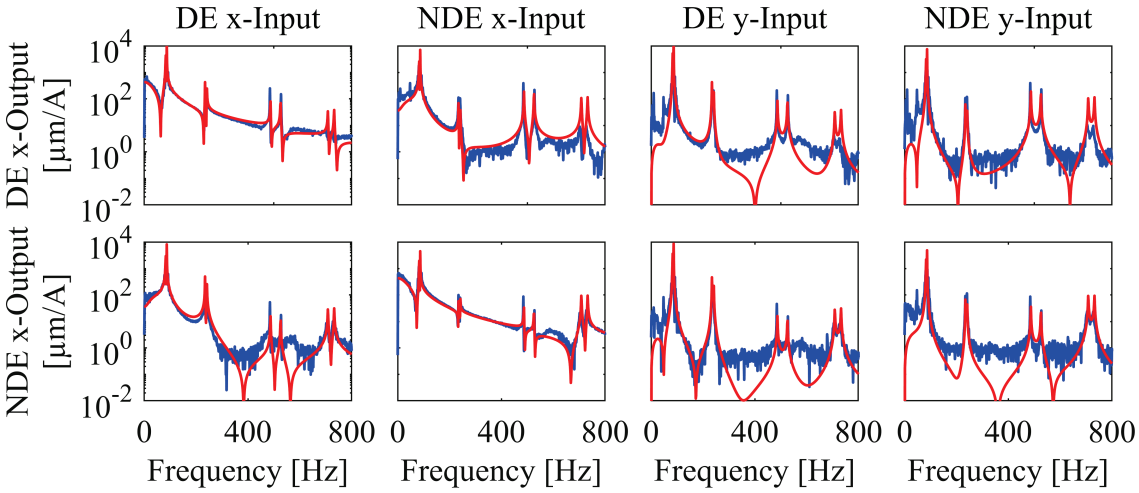

Figure 8: Comparison of model response (red) and open-loop FRD (blue), 3,000 rpm

2.2.2 300 kW Turbine Generator Model

A 300 kW turbine generator for a natural gas pressure letdown was reported by Khatri [67] and used in this research in simulation as an industrial example. The AMB system consists of two permanent magnet biased, homopolar magnetic bearings for radial axis and one thrust bearing that is integrated with one of the radial bearings. The schematic of the system is shown in Figure 9. The rotor of the system is fully supported by two radial AMBs, named Combo Endbell bearing on the impeller side and Radial Endbell bearing on the other side. The impeller is not shown in the picture.

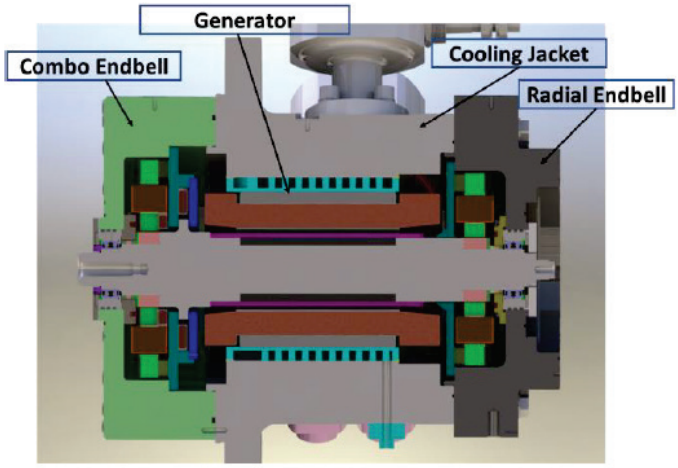

Figure 9: Schematic of the 300 kW turbine generator without the impeller [67]

The AMB system model was recreated from the information provided by Khatri [67]. The FE of the rotor model provided in the paper was reconstructed using XLRotor software. The reconstructed FE model of the rotor is shown in Figure 10. The impeller mass and inertia parameters were modeled as lumped masses at their respective nodes, whereas the stiffness contribution due to diameter increase was modeled via the Young's

modulus parameter of the impeller material, as was done in [67]. Not all parameters were reported in [67]. That is why some parameter values were tuned to match the flexible mode frequencies with the reported values. The AMB sensor and actuator position were also defined in the FE discretization.

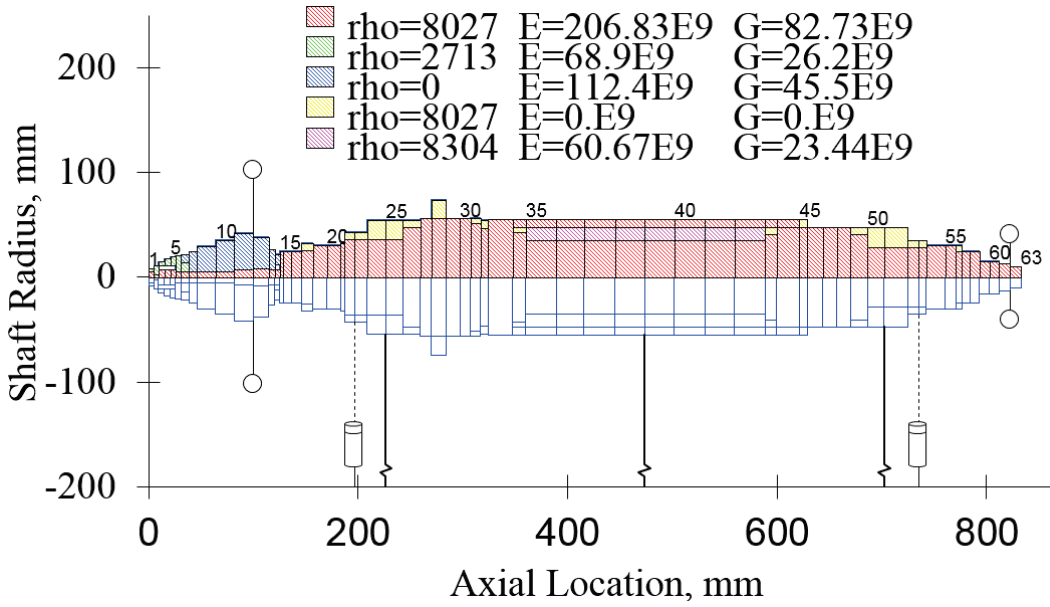

Figure 10: FE discretization of the rotor for modeling

The generated model closely matched the one from [67] with some discrepancies for the flexible mode frequencies. The main reasons behind the discrepancies are: 1) the dimensions of the rotor were extracted from a picture, which is a procedure that is prone to errors, and 2) the parameters for the lumped mass at the Radial Endbell side of the rotor was not mentioned in the paper. However, the errors between the natural frequencies of the generated model and the natural frequencies reported in [67] were less than 6%.

XLRotor software does not provide state-space matrices. That is why a MATLAB script was written to obtain the state-space matrices of the rotor based on the FEM matrix descriptions shown in [62] for Timoshenko beam elements. A modal truncation was applied to the rotor model to keep the two rigid modes and the lowest five flexible modes where 0.5% modal damping was applied to each flexible mode. Amplifiers were assumed to have a sensitivity of 2.8 A/V, and sensors were assumed to have a sensitivity of 19,685 V/m. The axial and radial dynamics were assumed to be decoupled, and only radial dynamics were considered, which resulted in a 4-input 4-output 44 state model. Figure 11 shows the frequency response of the model in one plane from the control input voltage to amplifiers to the position output voltage. The Radial Endbell side AMB is referred to as B1 and the Combo Endbell side AMB is referred to as B2. The rotor exhibits high gyroscopic effects due to the overhung impeller. This is apparent from the significant bifurcation of flexible mode frequencies.

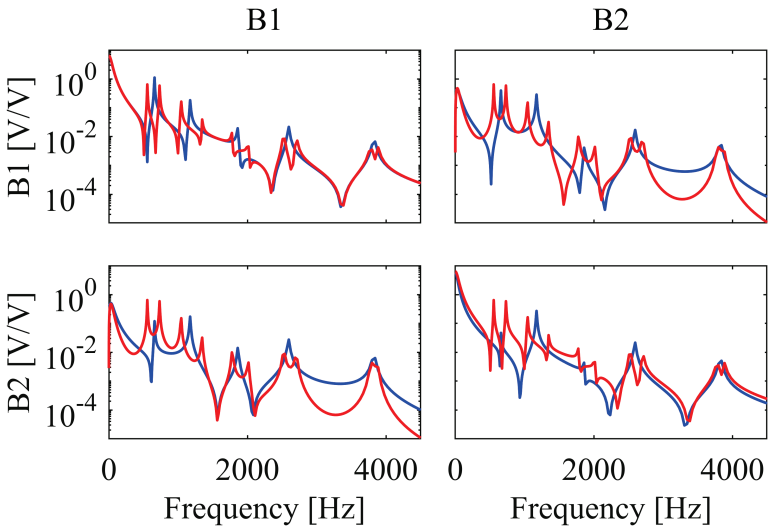

Figure 11: The 300 kW turbine generator model response, nonrotating (blue) and rotating at 32,000 rpm (red)

2.2.3 High-Speed AMB Machining Spindle

The high-speed AMB machining spindle (HSM AMB spindle), pictured in Figure 12, is located at Cleveland State University's Center for Rotating Machinery Dynamics and Control (RoMaDyC) lab. It is a prototype spindle system for boring operations. The high-speed spindle is supported by two radial AMBs and one thrust AMB. The control of the AMBs are done either by the manufacturer supplied control unit, which allows the implementation of industry-standard PID-type controllers, or dSPACE control unit, which allows the implementation of advanced control strategies.

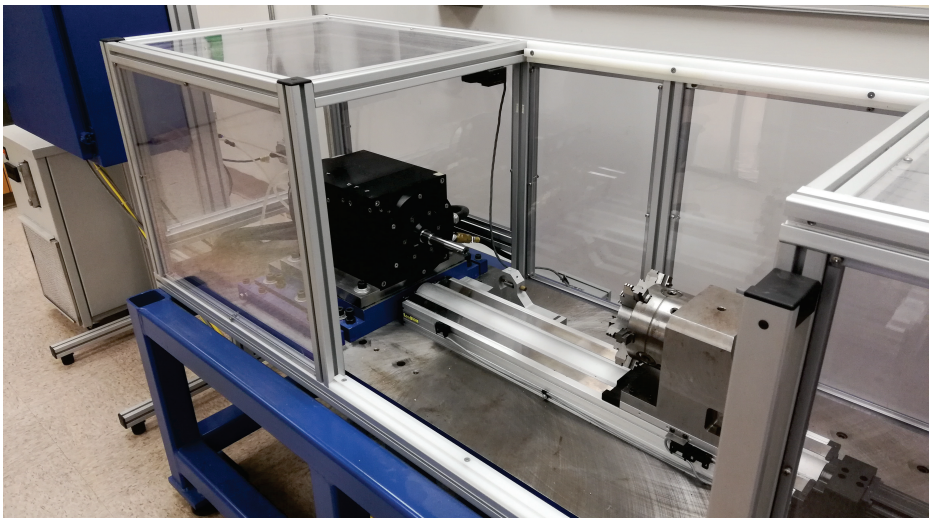

Figure 12: High-speed AMB machining spindle

The model of the system was previously obtained by Wroblewski et al. in [68] and the same model was used in this work after adjusting the AMB force constants based on the bias current of 4 A. The modeling procedure followed in [68] for the spindle system followed the same steps described in the previous sections. The FE model of the rotor was tuned via an optimization using experimental data to adjust for complex interactions

due to various interfaces present in the spindle rotor. For this purpose, Young's modulus parameter for the beam elements that corresponded to the hard-to-model parts, e.g., the motor section due to squirrel cage structure for the induction motor, the tool holder connection section due to the tapered fit, and both front and back radial AMB sections due to shrink fitted laminations, were adjusted to match the rotor model response to the experimental data obtained via a sine-sweep experiment on all four axis of the radial AMBs. After the optimization, the mass, stiffness, and gyroscopic matrices were derived for the rotor. Then the nodal model was converted into modal coordinates, where a modal truncation was applied to keep the two rigid modes and the lowest three flexible modes. The FE model of the rotor and its dimensions are shown in Figure 13. More information on the exact parameters used in each beam element is described in [69]. The AMB model was obtained via manufacturer supplied specifications. The amplifier model was experimentally identified and included the dynamics of the AMB electronics. Figure 14 shows the frequency response comparison of the AMB system model and the open-loop system response in the nonrotating case. The model accurately captures the dynamics of the physical system. The flexible mode frequencies, as well as the zeros of the system, match almost perfectly.

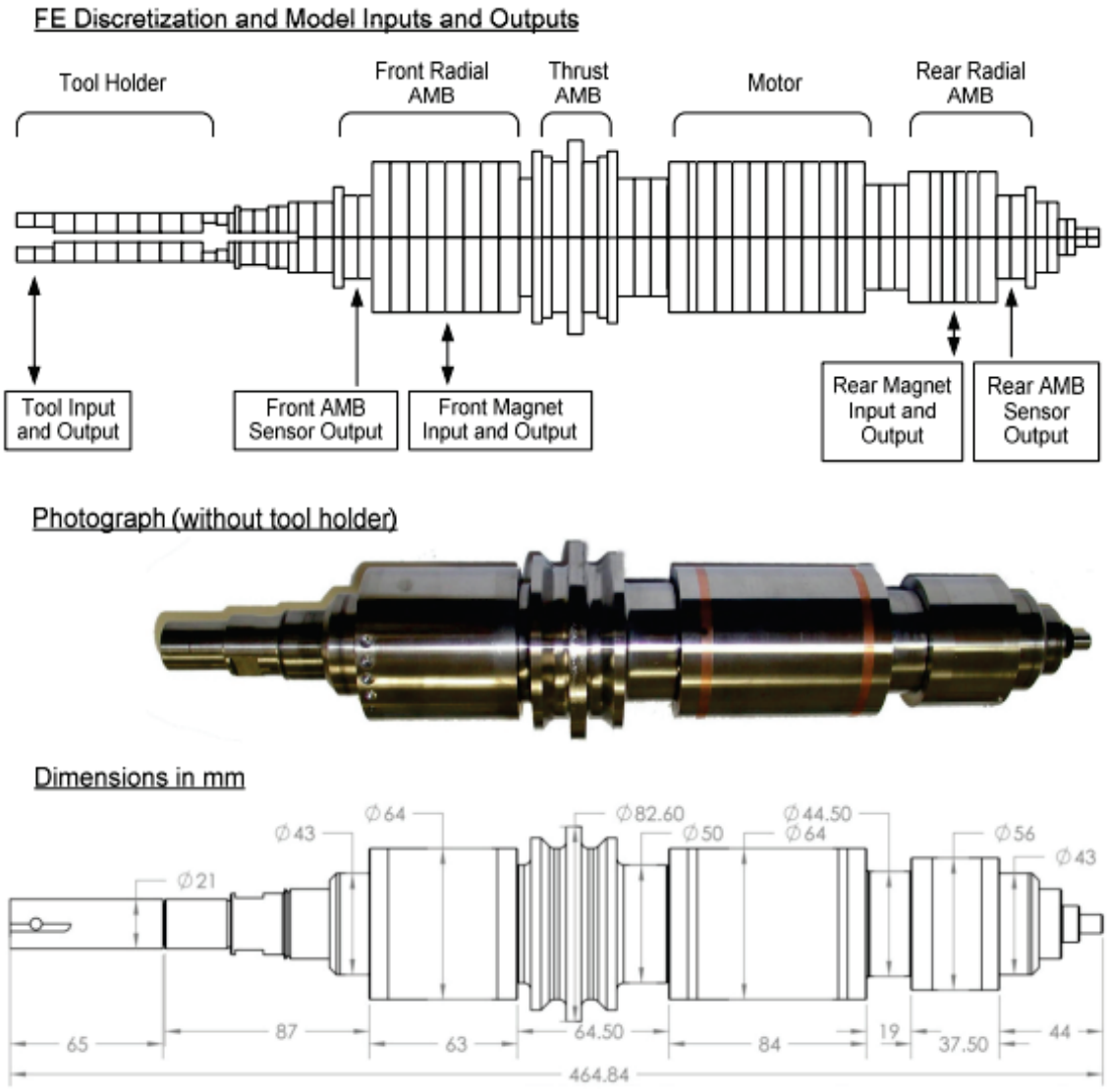

Figure 13: FE discretization of the spindle rotor with model inputs and outputs [69]

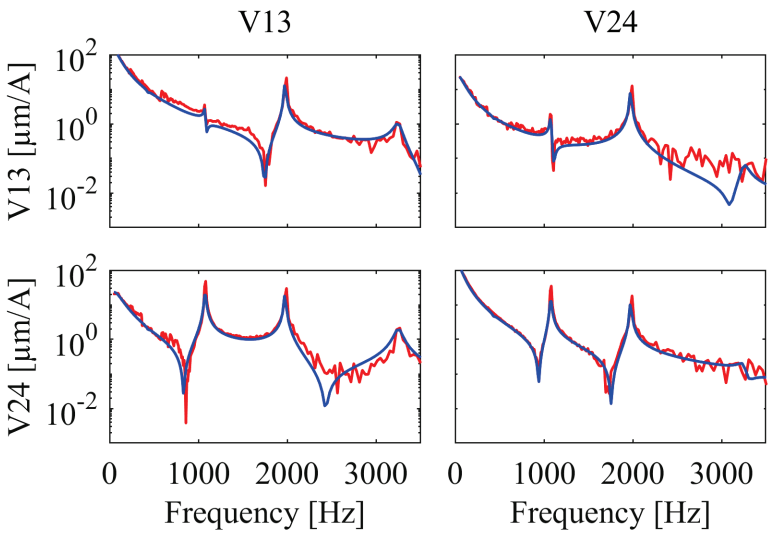

Figure 14: Comparison of HSM spindle model response (blue) and experimental data (red)

CHAPTER III

ROBUST CONTROL OF AMB SYSTEMS

3.1 Introduction and Background

In control theory, robust control refers to controller design techniques that account for inherent uncertainties in the plant model. The main goal of robust control is to design a controller that provides desired performance to a system in the presence of modeling uncertainties and disturbances. Robust control offers many powerful tools to describe plant uncertainties, analyze robustness, and synthesize robust controllers. The robust control techniques used in this research the H_∞ control and μ-control, both of which rely on H_∞ control theory and is the focus of this subsection.

3.1.1 Uncertainty

Uncertainties in plant models arise from many sources, e.g., imperfect plant data due to manufacturing tolerances, sensor noises, non-linearities, and neglected high-frequency dynamics. There are two ways to model the uncertainties in literature; parametric uncertainty and dynamic uncertainty [25]. Parametric uncertainties are used when some

of the parameters of a known structure of the plant are not known precisely. In parametric uncertainty, the model parameter is defined as an interval that has the value of the physical parameter. On the contrary, dynamic uncertainties do not require the knowledge of the structure of the plant model and are used to define frequency response bounds that encapsulate the frequency response of the physical system.

There are different representations for either class of uncertainty. The most common ways of representing uncertainty are in feedforward form as an additive or a multiplicative uncertainty [25]. Figure 15 shows the block diagram of three common uncertainty representations, where G is the model part with uncertainty, *w* is the weight that defines the magnitude of the uncertainty, and Δ is the so-called perturbation matrix where $\bar{\sigma}\big(\Delta(j\omega)\big) \leq 1$ for mathematical convenience. For parametric uncertainty, G represents the uncertain parameter, *w* is a scalar that defines the magnitude of the uncertainty, and Δ is any real scalar satisfying $|\Delta| \leq 1$. For dynamic uncertainty, G represents the nominal plant model, *w* is usually a stable and minimum-phase transfer function of appropriate dimension that defines the magnitude of the uncertainty at each frequency, and Δ is any stable transfer function of appropriate dimension with $\|\Delta\|_\infty \leq 1$.

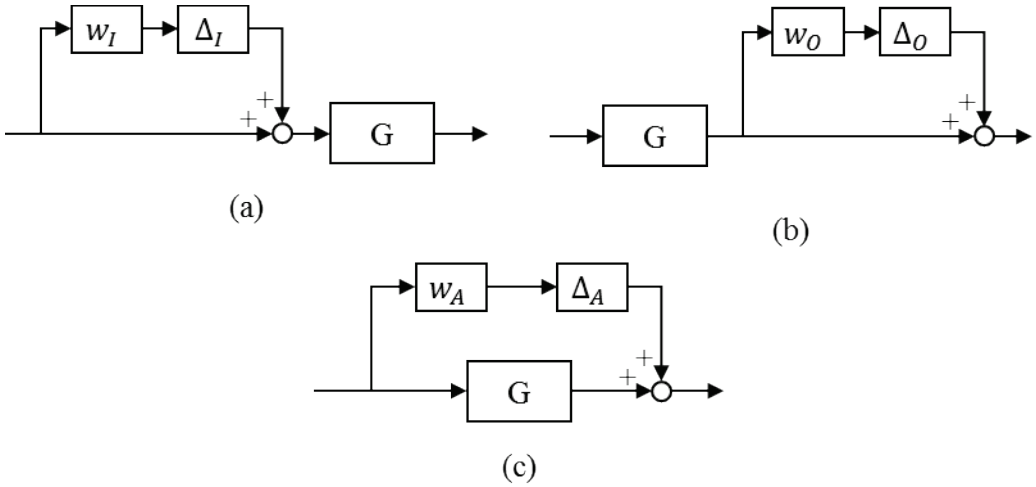

Figure 15: Block diagram of different uncertainty representations; (a) input multiplicative uncertainty, (b) output multiplicative uncertainty, (c) additive uncertainty

The uncertainties associated with each subsystem that is a part of the plant model are generally lumped into one uncertainty block [25]. The moving of uncertainties to a single uncertainty block is done via linear fractional transformation (LFT). Figure 16 shows the uncertainty representation for a plant model formed by upper LFT (i.e., $F_u(.,.)$ operator) with respect to the overall uncertainty block, Δ. If the overall uncertainty block, Δ, is a fully populated matrix of appropriate dimensions, it is called unstructured uncertainty. If Δ is a block diagonal matrix of appropriate dimensions, it is called structured uncertainty.

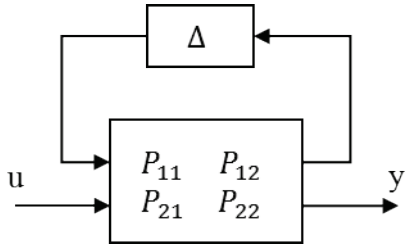

Figure 16: Uncertain plant representation as upper LFT

In Figure 16, P_{22} is the nominal plant model, u is the control input to the plant model, y is the output of the plant model, and the rest of the entries of P represent the relations between uncertainty channels and input-output channels of the plant model. It is common practice to lump the weights of uncertainties into the model, P, for mathematical convenience. It is trivial to show that the transfer function from u to y is

$$T_{yu} = F_u\left(\begin{bmatrix} P_{11} & P_{12} \\ P_{21} & P_{22} \end{bmatrix}, \Delta\right) = P_{22} + P_{21}\Delta(I - P_{11}\Delta)^{-1}P_{12} \tag{4}$$

The overall uncertainty matrix for the plant model is always structured, whether the uncertainty matrices of the subsystems are structured or unstructured. The difference in the presence of structured and unstructured uncertainty is significant in the analysis of robustness, which is discussed in the next section.

3.1.2 Robust Stability and Robust Performance Analysis

After representing the uncertain set of plants in PΔ-form shown in Figure 16, the controller to be analyzed for robustness is connected to the system to form the so-called MΔ-structure, as shown in Figure 17. MΔ-structure is used to determine robust stability, i.e., determine whether the closed-loop system is stable for all the plant models defined by the uncertainties.

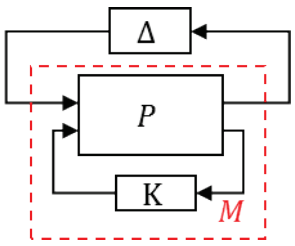

Figure 17: MΔ-structure for stability analysis

If the uncertainty block, Δ, is a full complex matrix satisfying $\|\Delta\|_\infty \leq 1$, which is often referred to as unstructured uncertainty, it can be shown via small gain theorem that the MΔ-system is stable if

$$\bar{\sigma}\big(\mathrm{M}(j\omega)\big) < 1, \forall\omega \;\; \Leftrightarrow \;\; \|\mathrm{M}\|_\infty < 1 \tag{5}$$

The condition in Eq. (5) is sufficient for robust stability in the case that the uncertainty block is unstructured. However, for structured uncertainty, which is commonly used in practice, the condition is conservative. For structured uncertainty, the fact that the uncertainty block is block diagonal, i.e., $\Delta = diag\{\Delta_i\}$, can be exploited to obtain tighter robust stability condition. This is done by rescaling the inputs and output of the M and Δ blocks of MΔ-structure with a block diagonal matrix D of appropriate size and structure, as shown in Figure 18.

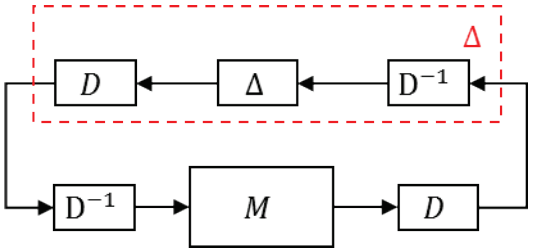

Figure 18: Scaled MΔ-structure

The scaling matrix D has no effect on the stability of the MΔ-system. Since the D matrix is chosen as block diagonal that is appropriately constructed for a given Δ, it can be shown that $\Delta_i = d_i \Delta d_i^{-1}$, hence $\Delta = \mathrm{D}\Delta\mathrm{D}^{-1}$. This means that the condition shown in Eq. (5) also applies to the rescaled case. The MΔ-system is stable if

$$\overline{\sigma}(\mathrm{D}(j\omega)\mathrm{M}(j\omega)\mathrm{D}(j\omega)^{-1}) < 1, \forall\omega \tag{6}$$

The condition in Eq. (6) applies to any scaling matrix D that corresponds to a particular Δ structure. That is why a less conservative robust stability condition for any MΔ-system, as shown in [25], is

$$\exists \mathrm{D}(j\omega) \in \mathcal{D} \text{ s.t. } \overline{\sigma}(\mathrm{D}(j\omega)\mathrm{M}(j\omega)\mathrm{D}(j\omega)^{-1}) < 1, \forall\omega \tag{7}$$

where $\mathcal{D}$ represents the set of block diagonal matrices that have a compatible structure to the given Δ block, i.e., $\Delta\mathrm{D} = \mathrm{D}\Delta$. This scaling is also applicable to unstructured uncertainty, however in the case of unstructured uncertainty, $\overline{\sigma}(\mathrm{DMD}^{-1}) = \overline{\sigma}(\mathrm{M})$. When the uncertainties have structure, there are more degrees of freedom in the D matrix and $\overline{\sigma}(\mathrm{DMD}^{-1})$ has the potential to become much smaller than $\overline{\sigma}(\mathrm{M})$. This is the main difference between the robustness analysis in the presence of structured uncertainty and unstructured uncertainty, i.e., the ability to obtain tighter robust stability conditions.

The robust stability condition in Eq. (7) for structured uncertainties motivated the development of the structured singular value [70, 71], which is a function that provides a scalar value to determine the robust stability. For a given MΔ-structure, where M is a complex matrix and Δ is a block diagonal complex matrix with $\overline{\sigma}(\Delta) \leq 1$, the real non-negative function $\mu(\mathrm{M})$, which is called the structured singular value, is defined as

$$\mu(\mathrm{M}) \triangleq \frac{1}{min\{\, k_m | \, det(\mathrm{I} - k_m\mathrm{M}\Delta) = 0 \; for \; structured \; \Delta, \bar{\sigma}(\Delta) \leq 1\}} \tag{8}$$

A $\mu(\mathrm{M})$ value of 0 implies that it is not possible to destabilize the system with the given uncertainty structure, and a $\mu(\mathrm{M})$ value of 1 means that there exists a perturbation

with $\overline{\sigma}(\Delta) = 1$ that is large enough to make $\mathrm{I} - \mathrm{M}\Delta$ singular. That is why the goal of μ-synthesis is to minimize the $\mu(\mathrm{M})$ value to be less than 1 to make sure of the robustness of the closed-loop system to the defined ranges of uncertainty. The μ-value cannot be calculated directly. However, it can be easily shown that $\mu(\mathrm{M}) \leq \min_{D \in \mathcal{D}} \overline{\sigma}(\mathrm{DMD}^{-1})$, where the optimization is convex in D [25]. Moreover, the inequality is an equality if Δ block consists of three or fewer blocks.

The structured singular value can also be used in robust performance analysis. Robust performance means that the performance specifications are satisfied for all possible plant models defined by the uncertainties. Robust performance analysis is an extension of robust stability analysis. For robust performance analysis, first, the system is put into PΔ-form, meaning the uncertainties are pulled out of the system. Then, the channels for the performance criteria are added along with weights that define the frequency content of the channels. The goal of the control is to keep the H_∞ norm of the transfer function for the performance channels to be less than unity for all possible plant models defined by the uncertainty. Assessment of robust performance via the structured singular value requires a modified MΔ-structure that is formed by closing the performance channels with a fictitious full complex "uncertainty" block, Δ_P. After forming the modified MΔ-structure, the structured singular value can be calculated to determine the robust performance, where the μ is computed with respect to $\widehat{\Delta} = diag\{\Delta, \Delta_P\}$. The block diagram of the modification is shown in Figure 19.

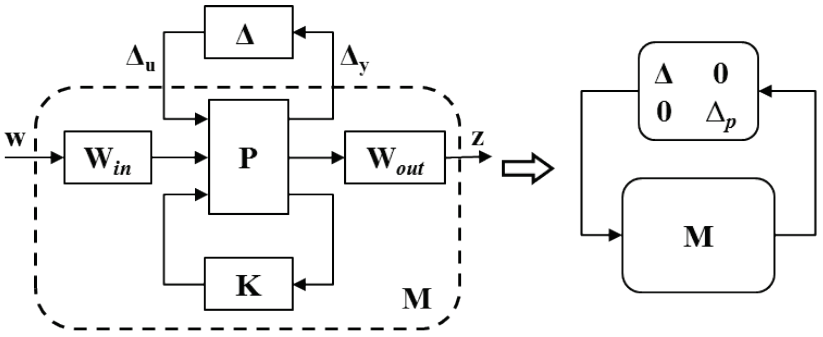

Figure 19: Robust performance analysis

3.1.3 Robust Controller Design

One of the most powerful control design techniques for plants with uncertainties is the μ-synthesis [25]. As the name suggests, the technique finds a controller that minimizes the μ value of the closed-loop system. The controller design procedure is performed by the so-called DK-iterations, which is a two-step optimization problem. The D optimization part tries to find the scaling matrices mentioned in the previous section that minimizes the maximum singular value of the closed-loop model M. The K optimization is the controller synthesis part where an H_∞ controller is synthesized for the scaled system. The following steps are followed in a DK-iteration algorithm.

1) Design an initial controller, K (usually H_∞ controller for the unscaled system)
2) Form $M = F_l(P, K)$, where F_l refers to lower LFT operator
3) Find discrete values for D matrix at each frequency of interest that minimizes the upper bound on μ, i.e., $\min_D \|DMD^{-1}\|_\infty$
4) Fit a rational transfer function to the frequency data of D found in step 3

5) Design an H_∞ controller for the scaled system, i.e., $\min_K \|DF_l(P,K)D^{-1}\|_\infty$

6) Go to step 2 until some convergence criteria are met

If DK-iteration results in a controller that achieves a μ-value that is less than unity, then the controller provides robust performance to the system assuming the plant model with uncertainties encapsulates the dynamics of the physical system.

There are a few disadvantages to μ-synthesis. First, although the two-step optimization, namely finding the D and K, are convex optimizations individually, it is not the case for the whole procedure. That is why sometimes, DK-iteration does not converge. The common practice to mitigate this problem is to run the DK-iterations multiple times with different initial controllers. Second, because the D matrix is found by fitting a rational transfer function to a frequency response data, it can result in high order transfer functions, which increases the resulting controller order. High-order controllers are not desirable from a practical implementation point of view. Lastly, the synthesized controllers can be unstable controllers, which introduces additional challenges for implementation.

3.2 Computational Cost of Controllers

The computational cost of controllers refers to the amount of necessary computational power to run a controller in real-time on hardware. There are three main factors that affect the computational cost of controllers, i.e., the order of the controller, the structure of the matrices that define the discrete-time matrix difference equations of the controller, and the algorithms used in performing the necessary matrix-vector multiplications. The

state-space realization of the controller and algorithms for matrix-vector algebra are closely related since the structure of the system matrices determine the available algorithms.

3.2.1 Controller Order Reduction

In the implementation of linear model-based MIMO controllers, it is common practice to employ a controller order reduction technique to reduce the overall computational cost of implementing the controller. The most common technique for AMB controllers that has been reported in the literature is the balanced truncation method introduced in [72] and its variations. The idea behind balanced truncation is to remove the states of a balanced realization of the controller that correspond to small Hankel singular values. In other words, the balanced truncation is a method that removes the states with energies below a chosen threshold. One of the reasons for the popularity of the method is its ability to provide error bounds between the full order model and the reduced-order model. Some application examples of balanced order reduction in AMB systems can be found in [39-41]. However, there is a limit on the achievable reduction in controller order before the closed-loop robustness and performance degrade to an unacceptable level.

3.2.2 Controller Realization and Algorithms for Matrix-Vector Algebra

The implementation of a controller on hardware can be made optimal by exploiting the structure of the state-space matrices since the state-space representation of a system is not unique. For this purpose, any state-space realization that gives matrices with high sparsity is a good choice (e.g., modal canonical form), since the sparsity of the matrices

allows the use of algorithms developed for sparse matrix-vector multiplication that are much more efficient compared to naive algorithms. In sparse matrix algebra, the zero entries of matrices are ignored completely, reducing not only the necessary number of multiply-accumulate (MAC) operations to calculate the output of the controller, but also the amount of space necessary to store the controller matrices.

There are different methods of implementing a sparse matrix-vector algebra, mostly due to the different types of available data structures. Common data structures for sparse matrices are coordinate format (COO), compressed sparse row format (CSR), compressed sparse column format (CSC), and diagonal format (DIAG) [43]. Simulink Coder also utilizes the sparse matrix algebra in implementing the discrete state-space blocks. A few more possible optimizations in sparse matrix-vector multiplication algorithms are discussed in [45].

3.2.3 Dual-rate Implementation of Single-rate Controller

Dual-rate implementation of a single-rate controller has been investigated in the literature to reduce the computational cost of implementing controllers, where computational cost refers to the necessary number of MAC operations to be performed at each time step. The early works on the topic mostly involve hard-disk drives [46-48]. Bhattacharya and Balas [36] developed a theoretical framework to analyze the stability of closed-loop systems with the dual-rate controller implementations, along with a comparison of the effects of different dual-rate configurations.

The modes of controllers, especially model-based controllers, are generally distributed in a wide range of frequencies. That is why the main idea behind the dual-rate

implementation of a single-rate controller is the fact that the controllers can be decomposed into fast modes and slow modes, where slow modes can be implemented at a slower rate to reduce the computational cost. Let $K(z)$ be a digital controller with a sampling rate of T_s for a continuous plant $P(s)$. $K(z)$ can be represented as the sum of its modes, as shown in Eq. (9), where $K_i(z)$ represents the individual modes of the controller with frequencies in ascending order.

$$K(z) = \sum_{1}^{r} K_i(z) \tag{9}$$

A threshold frequency can be chosen relatively arbitrarily such that n modes have frequencies less than the threshold and referred to as slow modes and $r - n$ modes that have frequencies higher than the threshold frequency and referred to as fast modes. Then, the controller can be decomposed in a parallel form as

$$K(z) = K_s(z) + K_f(z) \tag{10}$$

where $K_s(z) = \sum_{i=1}^{n} K_i(z)$ and $K_f(z) = \sum_{i=n+1}^{r} K_i(z)$. The dual-rate implementation of the controller $K(z)$ is shown in Figure 20, where S_f and S_s are fast and slow samplers that convert continuous-time signal to discrete-time signal using a low sampling period and high sampling period, respectively, and H is the zero-order hold operator.

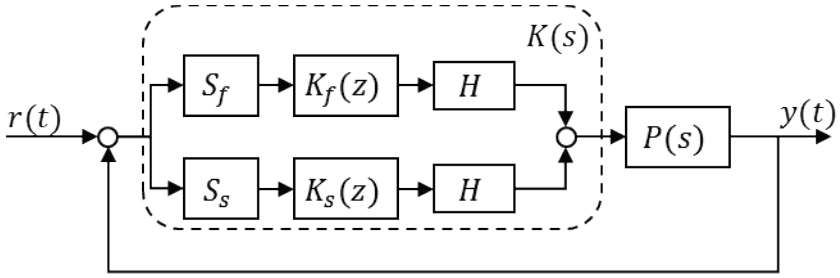

Figure 20: Dual-rate implementation of a controller

The slow modes, $K_s(z)$, in Figure 20, can be accurately implemented m times slower than fast modes, where m is an integer. This would mean that the calculations to update the states of $K_s(z)$ do not need to be performed at each time step, hence reducing the computational cost of the controller. However, at every m^{th} time step, the computational cost would be equal to the computational cost of the single-rate implementation, which would create periodic spikes in the computational cost. The spikes can be avoided by distributing the slow modes computations over m time steps to achieve a uniform reduction in the computational cost, which is referred to as interlacing. One method to distribute the computations of slow modes to multiple time steps is to further decompose the slow modes into the individual modes (assume $m = n$ for simplicity).

$$K_s(z) = K_1(z) + K_2(z) + \cdots + K_n(z) \tag{11}$$

Then, computations for each mode can be distributed over the m time steps, which would equalize the number of MAC operations at each time step. The performed algebraic operations of the single-rate implementation, along with the dual-rate implementation with and without interlacing, are shown in Table I, assuming each mode

requires the same number of MAC operations, and the slow modes are implemented m times slower.

Table I: Performed algebra at each time step for different implementations

	Time Step	0	1	2	…	m-1	m	$m+1$
Performed Operations	Single-rate	K_f, K_s	K_f, K_s	K_f, K_s	...	K_f, K_s	K_f, K_s	K_f, K_s
	Dual-rate w/o interlacing	K_f, K_s	K_f	K_f	...	K_f	K_f, K_s	K_f
	Dual-rate w/ interlacing	K_f, K_1	K_f, K_2	K_f, K_3	...	K_f, K_n	K_f, K_1	K_f, K_2

At this point, there are a couple of options for the actual implementation. One can choose to update the output of the slow modes as soon as K_i updates or wait until the n^{th} time step to combine all updates to K_i. This decision affects the representation of the dual-rate controller for analysis purposes. In this document, it is chosen to update the output of K_s all at once at every n^{th} time step.

Since the dual-rate controller includes two systems with different sampling rates, it is not possible to connect them directly. That is why a technique called lifting technique is commonly used to analyze the response of the dual-rate implementations [49].

Lifting technique is a powerful method that enables the use of tools developed for single-rate LTI systems in multi-rate systems. The main idea behind the technique is to represent a signal/system with a high sampling rate at a low sampling rate by increasing the dimensions of the signals. Assume a continuous-time signal $v = \{v(0), v(1), v(2), ...\}$ is sampled at every h seconds. The same signal can be represented as if it is sampled at every nh seconds, where n is an integer, via the lifting technique. The lifted signal, $\bar{v}$, can be rewritten as

$$\bar{v} = \left\{ \begin{bmatrix} v(0) \\ v(1) \\ \vdots \\ v(n\text{-}1) \end{bmatrix}, \begin{bmatrix} v(n) \\ v(n\text{+}1) \\ \vdots \\ v(2n\text{-}1) \end{bmatrix}, \dots \right\} \tag{12}$$

It is trivial to show that the operator, called lifting operator, that maps v to $\bar{v}$ is norm preserving, i.e., $\|v\|_2 = \|\bar{v}\|_2$. A system can also be lifted by simply adjusting the system matrices to match the lifted signals. A discrete-time finite-dimensional system G implemented with a sampling time of h seconds can be lifted to correspond to a sampling time of nh seconds and the lifted system $\overline{\mathrm{G}}$ can be written as

$$\mathrm{G} = \begin{bmatrix} \mathrm{A} & \mathrm{B} \\ \mathrm{C} & \mathrm{D} \end{bmatrix} \rightarrow \overline{\mathrm{G}} = \left[\begin{array}{c:ccc} \mathrm{A}^n & \mathrm{A}^{n-1}\mathrm{B} & \mathrm{A}^{n-2}\mathrm{B} & \cdots & \mathrm{B} \\ \hdashline \mathrm{C} & \mathrm{D} & 0 & \cdots & 0 \\ \mathrm{CA} & \mathrm{CB} & \mathrm{D} & \cdots & 0 \\ \vdots & \vdots & \vdots & & \vdots \\ \mathrm{CA}^{n-1} & \mathrm{CA}^{n-2}\mathrm{B} & \mathrm{CA}^{n-3}\mathrm{B} & \cdots & \mathrm{D} \end{array}\right] \tag{13}$$

3.3 New Strategies for Selecting the Optimal Dual-rate Configuration

The literature on dual-rate implementation of controllers for computational savings does not provide much information on robust performance analysis. That is why two novel methods are proposed where the lifting technique and μ-analysis are used to assess the closed-loop performance. The first method uses the worst-case plant model in the analysis of the robust performance of a dual-rate configuration of a single-rate controller. The second method defines perturbation on the controller response that is large enough to compromise robust performance. The magnitudes of the perturbations at each frequency are found utilizing the μ-analysis.

3.3.1 Optimal dual-rate configuration via worst-case plant

The dual-rate implementation can reduce the computational cost significantly, as shown in the literature [36, 46]. However, There is no systematic procedure to select the dual-rate configuration that maintains robust performance. That is why a method is developed and presented in this section that uses lifting technique along with the worst-case plant to determine the optimal dual-rate configuration to maximize computational saving while maintaining robust performance.

In robust control, the worst-case plant model refers to the uncertain plant parameters that result in the largest H_∞ norm with a given controller. In other words, the worst-case plant is the most challenging plant model within the uncertain set of plants for the controller to provide robust performance. The worst-case plant parameters can be found via a simple search algorithm. In this study, the Matlab function *wcgain* [73] is used.

After identifying the worst-case plant model, possible dual-rate configurations need to be determined using some engineering knowledge. This involves selecting the number of modes to be included in the slow modes and the rate at which the slow modes are going to be implemented. Other than the choices limited by the control hardware, the possible configurations are relatively easy to determine. They are determined by calculating the lower bounds on the implementation rate for each mode of the controller and choosing the possible configurations by making sure high enough discretization rates are used for each of them. For each dual-rate configuration of the controller, a lifted closed-loop system is formed by appropriately lifting the worst-case plant model, fast modes of the controller, and slow modes of the controller to match the sampling rate of the slow modes.

Then, since the lifting operation is norm preserving, the largest singular value analysis is performed on the lifted closed loop system to determine if the analyzed dual-rate implementation of the controller still maintains the robust performance, i.e., is the largest singular value of the lifted closed loop system less than unity. It is also worth mentioning that aliasing issues are a common problem in the dual-rate implementation of controllers. However, the issue would show up in the singular value analysis, and the proposed method would yield unsatisfactory results for any dual-rate configuration that might cause significant aliasing, see [74] for more information. The number of multiply-accumulate (MAC) operations can be used to estimate the computational cost in terms of the CPU time for the hardware to perform the required controller algebra.

The proposed method to select the optimal dual-rate configuration can be summarized with the following five steps.

1. Synthesize a robust controller.
2. Find the worst-case plant model.
3. Form the lifted closed-loop system with possible dual-rate configurations and calculate the largest singular value for each of them.
4. Identify the dual-rate configuration that maintains robust performance and achieves the largest reduction in computational cost in terms of the number of MAC operations.
5. Implement the chosen dual-rate controller in step 4 in modal canonical form while utilizing the sparse matrix algebra. Apply the interlacing technique to decrease the computational cost uniformly.

This approach was applied to the AMB test rig. The results are presented in Section 4.1.

3.3.2 Optimal dual-rate configuration via controller perturbation

The worst-case plant approach for selecting the dual-rate configuration has one major assumption that might not be true for some systems. The approach assumes that the difference in the dynamic response between the single-rate and dual-rate implementations of the same controller has the most significant effect in the worst-case plant. The main idea behind the assumption is that the worst-case plant would be the first plant model to lose robust performance due to the changes in the controller dynamics. However, this might not be true for some systems. That is why a more general approach is proposed to identify the optimal dual-rate configuration via defining controller perturbation.

The developed approach first finds the largest perturbation to the controller that pushes the μ-value to unity at all frequencies. This perturbation defines bounds in the frequency domain for the controller, where if the response of an implemented controller is within the bounds, the implemented controller maintains robust performance. Similar to the worst-case plant approach, the different dual-rate configurations are identified first. Then, their frequency responses can be compared to the bounds to determine whether they are feasible or not to maintain the desired robust performance. Figure 21 shows the block diagram of the approach where w and z are the exogenous inputs and performance outputs, respectively, u and y are the control input and sensor outputs, respectively, P is the nominal plant, K is the robust controller, Δ represents the plant uncertainties, Δ_k represent the controller perturbation that pushes the μ-value to unity at each frequency, and the red dashed part represents the uncertain set of plants. The introduced controller perturbation block can be thought of as a fictitious modeling uncertainty.

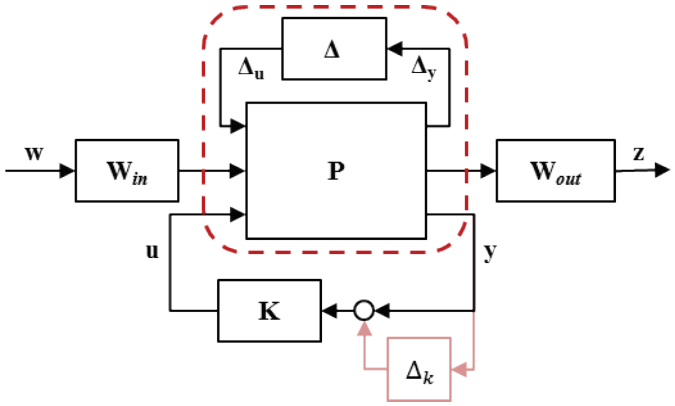

Figure 21: Block diagram of a controlled system with the proposed controller perturbation block

Since all inputs to the controller, signal *y*, goes through the same dual-rate sampling procedure, their frequency response would be altered similarly. That is why the structure of the controller perturbation block is chosen as an input multiplicative diagonal complex perturbation with different magnitudes at each frequency. A simple bisection algorithm is used to find the magnitudes of the perturbation block.

This method is applied to the 300 kW turbine generator and HSM AMB spindle, where the results are shown in Section 4.2 and Section 4.3, respectively.

3.3.3 Comments on the proposed methods

The first method, i.e., the worst-case plant approach, is relatively straight-forward to apply to any system. The challenging parts of the method are the identification of the worst-case plant model, which can be done with MATLAB function *wcgain* [73], and the determination of possible dual-rate configurations, which relies on engineering knowledge in the effects of sampling rate in the dynamic system discretization. The method has one major assumption that any closed loop system formed with the worst-

case plant model has the maximum largest singular value regardless of the dual-rate configuration used for the controller. This assumption considers the difference between the single-rate and dual-rate implementations of the controller to be representable by an increase in the uncertainty magnitudes in the plant model. Although the assumption holds for most AMB systems since various sources of uncertainty exist in the models that can cover the difference, there might be cases where the uncertainties cannot represent the difference between the single-rate and dual-rate implementations of the controller responses. This is what motivated the second method, i.e., finding the largest perturbation to the controller that pushes the μ-value to unity. Since perturbations are defined directly on the controller, the assumption to represent the difference in the controller response with the model uncertainties is not needed in the second method. However, with the second method, the structure of the perturbation block needs to be defined. The choice of the structure of the perturbation block, which is chosen as diagonal perturbation in this research, has an impact on the results since it defines the magnitude and direction of the bounds on the controller response.

3.4 Redesign of Robust Controllers for Computational Savings

The idea of using the largest perturbation to the controller that maintains the robust performance is introduced in the previous section to identify the feasible dual-rate configurations. Another use is to assess the importance of each controller channel. In other words, negligible channels of the controller in the context of robust performance can be identified. Then, the controller can be redesigned by removing the negligible channels.

To determine if a controller channel can be ignored is equivalent to determining if removing the channel would alter the controller response to an extent where the response would lie outside of the bounds defined by the largest perturbation. Although not necessary, two assumptions are made to ease the analysis procedure: 1) isotropic behavior is expected in the AMB bearings, and 2) disturbance forces are not dominant in one plane. These assumptions can be removed by appropriately scaling controller channels such that the inputs to the scaled controller satisfies the assumptions. The rest of the section explains the proposed method of controller redesign based on a generalized MIMO controller to achieve computational saving.

For a given 4-input 4-output controller K that achieves robust performance (which is the case for most AMB systems with two radial AMBs to support the rotor), the output of the controller, y, is calculated by the transfer matrix algebra shown in Eq. (14).

$$\begin{bmatrix} y_1 \\ y_2 \\ y_3 \\ y_4 \end{bmatrix} = \begin{bmatrix} K_{11} & K_{12} & K_{13} & K_{14} \\ K_{21} & K_{22} & K_{23} & K_{24} \\ K_{31} & K_{32} & K_{33} & K_{34} \\ K_{41} & K_{42} & K_{43} & K_{44} \end{bmatrix} \begin{bmatrix} u_1 \\ u_2 \\ u_3 \\ u_4 \end{bmatrix} \tag{14}$$

The transfer matrix elements K_{ij} defines the effects of the input signal u_j on the output of the controller y_i. Previously mentioned largest perturbation to the controller defines bounds on each element, which in return defines bounds on the singular values of the frequency response of the controller. The assessment of whether the effect of a channel is negligible or not is based on whether the singular values of the frequency response of the controller lies within the bounds after removing the channel. The diagonal channels cannot be removed since they represent almost collocated actuator-sensor interaction.

The proposed approach analyzes each row of the controller individually to determine the channels that can be removed in that row. This is done by checking if neglecting a channel causes the singular value of the frequency response of that row to go over the bounds defined by the controller perturbation. The two assumptions stated earlier is useful because, with the assumptions, the expected magnitudes of each input signal to the controller is similar. This allows direct comparison of the controller singular values when a channel is removed, instead of the need to scale certain channels.

To illustrate the proposed method, let K_{in} be the i^{th} row of the controller where certain channels are equated to zero, hence removed. Then, if the singular values of the response of K_{in} stays within the bounds defined by the perturbation, the said channels are deemed negligible and can be removed from the controller. This can be checked easily by comparing the error between the singular value of the i^{th} row of the controller and K_{in} to the bounds defined by the perturbation. Let $p_i(\omega)$ be the magnitude of the bounds on the singular values of the i^{th} row of the controller defined by the controller perturbation block, $a(\omega) = \sigma([K_{i1}\ K_{i2}\ K_{i3}\ K_{i4}])$, and $b(\omega) = \sigma(K_{in})$, where σ refers to the singular value response of a system. Then the removed channels in K_{in} have negligible effects on robust performance if following inequality holds

$$p_i(\omega) \geq |a(\omega) - b(\omega)| \tag{15}$$

The negligible channels then can be found by a simple trial-error based method where each channel can be removed one at a time, and the inequality (15) can be used to assess their importance, repeating the same procedure for all the rows of the controller. For AMB systems, starting from off-diagonal channels of the controller, i.e., channels for x-

output y-input and y-output x-input, is a good starting point. Also, the diagonal channels, i.e., the same control axis input-output channels, are always non-negligible.

Although the method finds the negligible channels in the controller, it is not simple to remove the effects of an input on a particular output in a MIMO system. For this reason, after the negligible channels are identified, a decision on how to fit a dynamic system to the remaining channels needs to be made. For most AMB systems with symmetric rotors and AMBs, the perpendicular axes of the same radial bearing are almost identical. This results in controller synthesis procedures to generate similar, if not identical, control dynamics for the perpendicular axes of the same bearing. With this knowledge, depending on how many channels are deemed negligible, there are system-specific choices.

There might be cases where none of the controller channels might be negligible. In that case, a desired order controller might be fitted within the bounds defined by the MIMO controller and the perturbation block. The model-fitting approach is a tedious and trial-error based approach which might not even result in any computational savings.

This method is applied to the 300 kW turbine generator and HSM AMB spindle, where the results are shown in Section 4.2 and Section 4.3, respectively.

CHAPTER IV

APPLICATION OF THE PROPOSED METHODS

The proposed methods to reduce the computational cost of robust controllers were demonstrated on three AMB systems, i.e., the AMB test rig, 300 kW turbine generator, and HSM AMB spindle.

4.1 AMB Test Rig, Worst-Case Plant Approach

As a first step in the control problem formulation for the AMB test rig, standard uncertainties for AMB systems were defined, as shown in Table II. The uncertainties for flexible mode frequencies and damping were determined by a simple examination of the frequency response comparison between the model and the data shown in Figure 7. The uncertainties for the AMB force constants were identified analytically such that the linearized AMB force model would encapsulate the non-linear force model within the operating region. Lastly, the uncertainty for the rotational speed was chosen arbitrarily as from 0 to 3,000 rpm for this study, since 3,000 rpm was chosen as the highest operating speed.

Table II: Uncertainties for the AMB test rig

Parameter	Nominal Value	Uncertainty	Type
Flexible modes	[94,721,506,721] Hz	±1.5%	Complex
Current stiffness	25.33 N/A	±10%	Real
Position stiffness	0.064 N/μm	±15%	Real
Rotational speed	1500 rpm	±100%	Real

The second step in the control problem formulation is to define the desired performance via the weights that represent the frequency contents of performance outputs and exogenous inputs in the frequency domain. For this reason, exogenous inputs were chosen to be sensor noise and general disturbance forces acting on AMB locations that represent unbalance forces and forces that arise due to misalignment between the rotor, motor, and bearing centers. The performance outputs were chosen to be vibration amplitudes at sensor locations to control orbit sizes and control current magnitudes to prevent actuator saturations. The parameters that were used to describe the frequency content of these signals are shown in Table III.

Table III: Parameter describing the performance criteria

Weights	Low frequency	High frequency	Cross-over frequency	Roll-off frequency
Disturbance force	6 N	4 N	0.01 Hz	90 Hz
Noise level	0.6 μm	0.6 μm	-	-
Vibration amplitude	3 μm	30 μm	1 Hz	-
Control current magnitude	1 A	1 A	-	750 Hz

The method described in [34] was applied to solve the signal-based H_∞ control problem, which uses the genetic algorithm (GA) to tune the weights to synthesize a stable controller that satisfies the desired robust performance. In summary, the method separates the weights used in controller synthesis, referred to as synthesis weights, and weights

used in performance analysis referred to as performance weights. The synthesis weights are then tuned via GA where the cost function is the μ-value of the closed-loop system with performance weights plus a penalty term for unstable controllers. The order of the resulting controller with this method is always equal to the order of the plant model plus the order of performance weights. With the given plant model and performance weights for the AMB test rig, the synthesis resulted in a 52-order controller with an achieved μ-value of 0.94. Controller order reduction was tried, however removing two states of the controller pushed the achieved μ-value to unity. That is why the 52-order controller was used as the single-rate implementation.

For the second step of the worst-case plant approach, *wcgain* function of Matlab was used to obtain the uncertain parameters of the AMB system model that resulted in the largest singular value of the closed-loop system with the designed controller. The third step requires engineering judgment to identify possible dual-rate configurations. Considering the hardware of the AMB system, which allowed a maximum of 10 kHz sampling rate, up to 5 times slower sampling rates were considered for the slow modes. The considered slow modes sampling rates were chosen based on the natural frequencies of the controller modes, where the first 14 lowest frequency modes required at least 2 kHz sampling rate. Then, a table was created for the considered dual-rate configurations, and is shown in Table IV.

The largest singular values for each dual-rate configuration, as well as the normalized computational costs, were analytically calculated using the lifting technique. The rows of Table IV represent the number of modes considered in the slow modes at ascending frequency. The columns represent the frequency ratio between the fast modes and the

slow modes of the controller. The dual-rate configurations in the first row and first column are practically identical to the single-rate implementation of the controller. The computational cost was calculated by determining the necessary number of MAC operations to perform the necessary matrix-vector multiplications for a given implementation using the modal canonical form and sparse-matrix algebra. The number of MAC operations of each dual-rate implementation was then normalized with respect to the single-rate implementation. For reference, the single-rate implementation of the designed robust controller using modal canonical form along with sparse-matrix algebra required 520 MAC operations at each time step.

Each considered dual-rate configuration was implemented experimentally. Peak-to-peak vibration amplitudes at various rotational speeds, as well as the control currents, were compared to the performance specifications. The experimental assessment of each dual-rate configuration are shown with colors in Table IV, where green color represents satisfactory performance, orange color represents satisfactory performance up to a rotational speed below the maximum design speed, and red color represents the configuration cannot stabilize the system, even in the nonrotating condition. The experimental results match with the analytical results, demonstrating the feasibility of the proposed method in choosing the dual-rate configuration.

Table IV: Robust performance analysis with dual-rate controller

Number of Modes in Slow Modes	Highest Frequency in Slow Modes [Hz]	Maximum Singular Value / Normalized Computational Cost				
		1x 10 kHz	2x 5 kHz	3x 3.$\bar{3}$ kHz	4x 2.5 kHz	5x 2 kHz
0	-	0.94/1.00	0.94/1.00	0.94/1.00	0.94/1.00	0.94/1.00
4	1.5	0.94/1.00	0.94/0.92	0.94/0.89	0.94/0.88	0.94/0.87
9	227	0.94/1.00	0.94/0.82	0.94/0.77	0.94/0.74	0.94/0.78
10	235	0.94/1.00	0.94/0.80	0.94/0.74	0.94/0.71	0.94/0.69
11	525	0.94/1.00	1.36/0.78	3.60/0.71	6.33/0.68	5.76/0.66
12	557	0.94/1.00	1.98/0.76	- /0.69	- /0.65	- /0.63
26	2386	0.94/1.00	- /0.50	- /0.33	- /0.25	- /0.20

From Table IV, it is clear that the configuration 5x-10 achieved the most computational saving while maintaining robust performance and was chosen to be compared in performance with the single-rate implementation of the controller. Both single-rate and dual-rate controllers were implemented using dSPACE MicroLabBox. As a first test, the computational cost of single-rate implementation and dual-rate implementation with and without interlacing was compared and is shown in Figure 22. As mentioned in previous sections, without the interlacing technique, the computational cost of dual-rate implementation would be equal to the single-rate implementation at every m^{th} time step, which can be observed in Figure 22 where m is equal to 5. The interlacing simply distributes the overhead calculations to multiple time steps. That is why the CPU time for dual-rate implementation with interlacing is slightly higher than without interlacing, with the exception of every 5th-time step. The average CPU time for single-rate implementation is around 1.14 µs, and the dual-rate implementation is around 0.74 µs, which implies a 35% reduction in computational cost. There is a slight discrepancy between analytically determined 31% reduction, which can be explained

either by the way the average times are determined and/or the low-level optimization the software used to program the hardware.

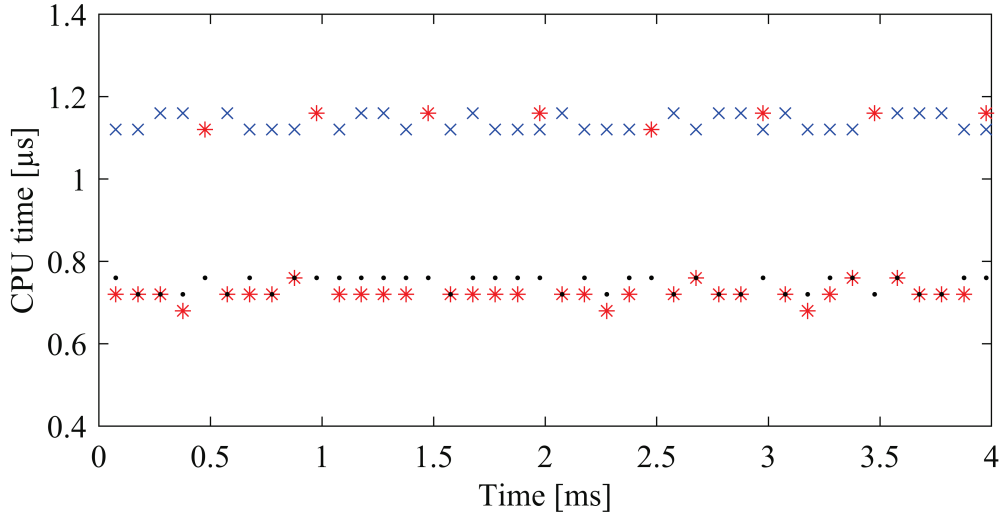

Figure 22: Computational cost comparison of single-rate (blue -x), dual-rate without interlacing (red-star*), and dual-rate with interlacing (black-dot.) implementations of the controller

The second test was performed to observe the step response of the system with the single-rate and the dual-rate implementations. For this reason, the trajectory at initial levitation was compared. Figure 23 shows the trajectories at each AMB axis. Before the tests, the rotor was manually positioned at similar initial positions to have a meaningful comparison, since the resting position of the rotor can be anywhere on the backup bearings, which have a clearance of 190 µm when the rotor is at the center of the bearing. The overall step response was similar, if not identical, with both controllers. The coupling element between the rotor and the motor provided a slight lift to the DE side. However, the main reason behind the faster settling time between DE and NDE side was the larger stiffness provided by the controller. On the NDE side, the stiffness did not seem to be enough to push the rotor to center, and the modes that provide high-stiffness at low

frequencies slowly drove the rotor towards the center of the bearing. There is high overshoot at both bearing responses. The reason is that the performance criteria were determined by assuming the rotor would be positioned at the center of the bearing, which was not the case during initial levitation. The overshoot can be overcome by providing a ramp reference input for levitation instead of a step reference input.

Lastly, AMB system orbit sizes and shapes at various speeds were compared. For this reason, data was collected at 1,000, 2,000, and 3,000 rpm. Figure 24 shows the achieved orbits with single-rate and dual-rate implementations. Both controllers achieved similar orbits, with the exception of NDE bearing at 3,000 rpm. However, the dual-rate implementation still kept the orbits within the desired magnitude with a reduced computational cost.

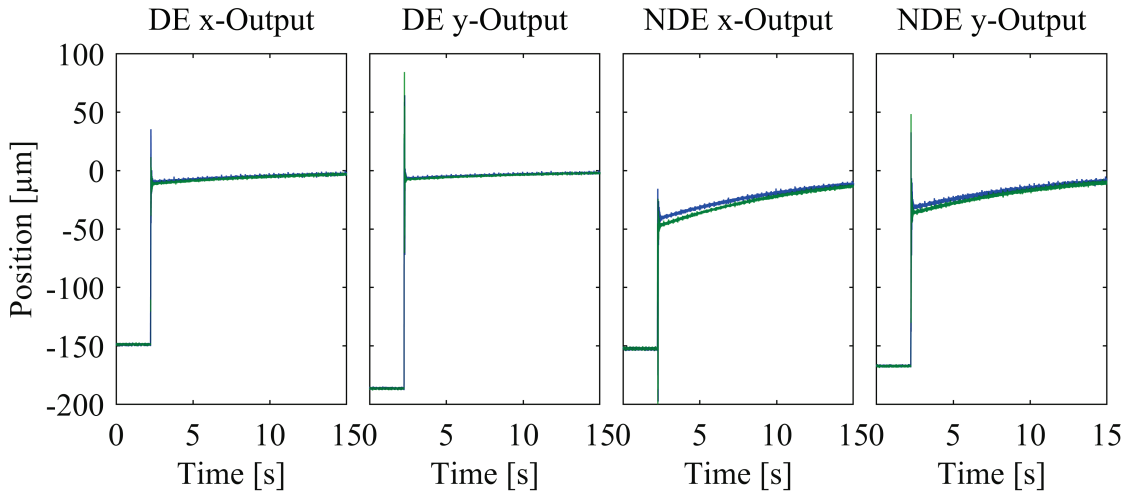

Figure 23: Initial levitation comparison of single-rate implementation (blue) and dual-rate implementation (green)

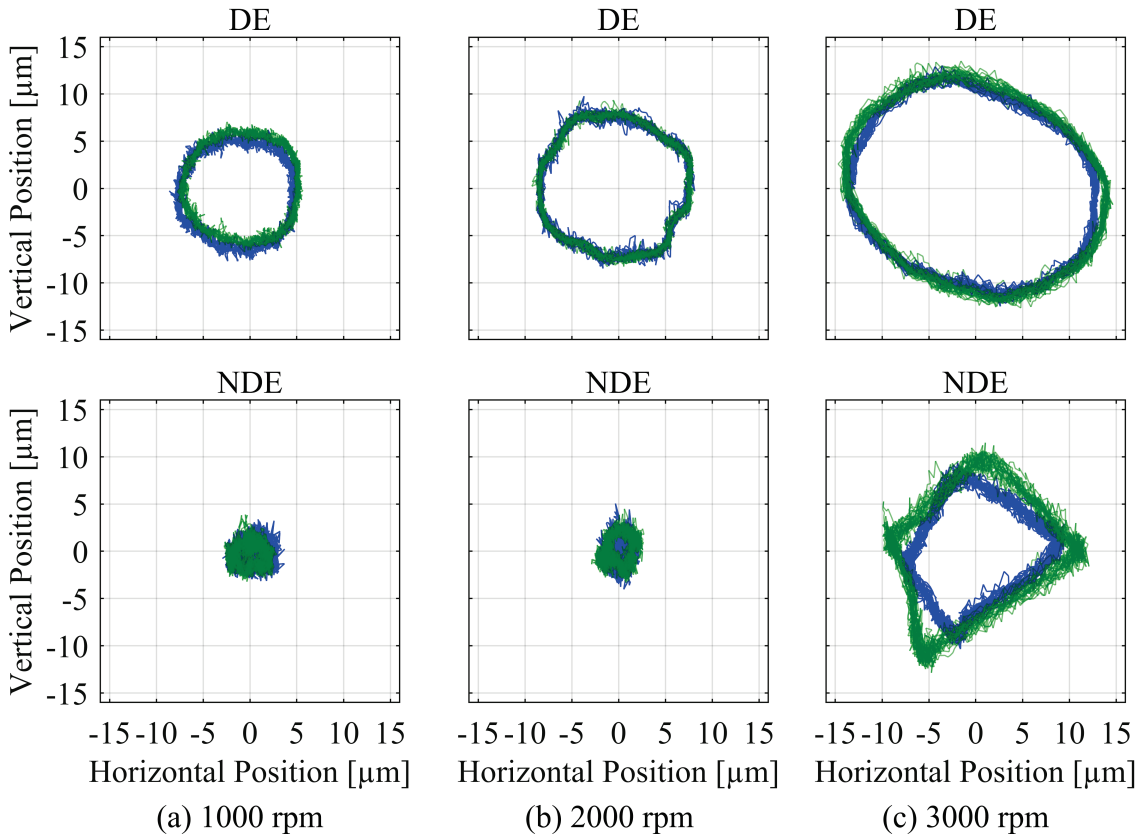

(a) 1000 rpm (b) 2000 rpm (c) 3000 rpm

Figure 24: Orbit sizes with single-rate implementation (blue) and dual-rate implementation (green)

4.2 300 kW Turbine Generator, Dual-rate Controller Implementation and Redesign of Robust Controller via Controller Perturbation [76]

The approaches presented in Sections 3.3.2 and 3.4 were applied to the model of 300 kW turbine generator [76]. A robust controller for the model was first designed. For this purpose, standard uncertainties for AMB systems were defined for the 300 kW turbine generator model, i.e., 1% uncertainty on flexible mode frequencies, 15% uncertainty on flexible mode damping, 10% uncertainty on current stiffness, 5% uncertainty on position stiffness, and rotational speed to cover the whole operating range from 0 rpm to 32,000 rpm. Then, the performance weights were constructed in a disturbance rejection scheme

where the goal was set to keep the vibrations at AMB sensor locations within a certain magnitude without saturating the AMBs while the system was under the influence of sensor noise and disturbance forces. Although there are multiple sources of disturbance forces acting on the system, they were assumed to act at AMB actuator positions to simplify the problem formulation. Special attention was given to the magnitude of the weights such that the closed-loop sensitivity magnitude would be less than 10 dB as per ISO standards [61]. The robust controller was synthesized using *dksyn* function of MATLAB, which resulted in a stable 62-order controller with a μ-value of 0.91. Figure 25 shows the closed-loop sensitivity functions at each bearing with the full-order controller. As per the design requirement, the sensitivity function never goes above 10 dB.

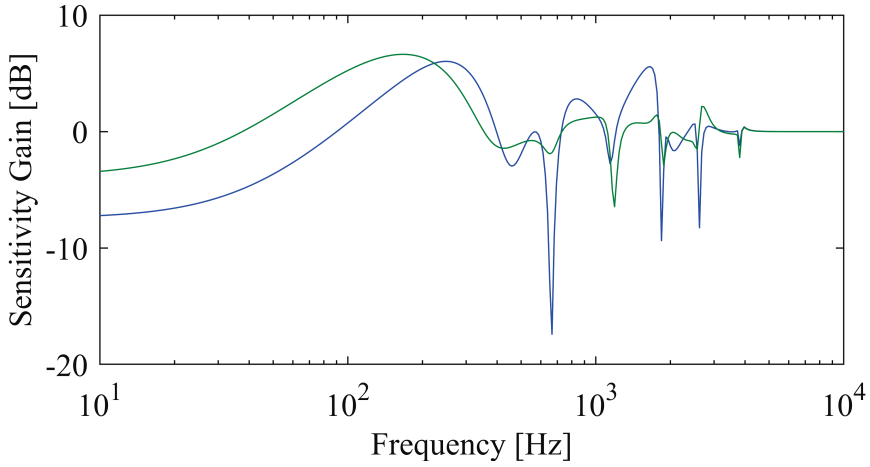

Figure 25: Sensitivity function of 300 kW turbine generator with the designed μ-controller; B1 (blue) and B2 (green)

After synthesizing the controller, the order of the controller was reduced to 42 via balanced truncation, which was the smallest order the controller could be reduced to while keeping the μ-value below unity. The reduced-order controller had 42 states,

corresponding to 21 modes, and required 418 MAC operations, which is the number used to normalize computational cost.

As a first step for the proposed methods, the controller perturbation block that pushed the μ-value to unity was identified via a simple bisection algorithm. The controller perturbation block was assumed to be input multiplicative diagonal complex perturbation. Figure 26 shows the μ plot of the closed-loop system with the full order controller with and without the controller perturbation block, which indicates robust performance if the value stays below unity. The found perturbation block does not exactly make the μ-value equal to unity at all frequencies, as seen in Figure 26. There is a slight chatter, especially around the natural frequencies of the AMB system. The amount of deviation from unity can be controlled by defining lower tolerances in the bisection algorithm.

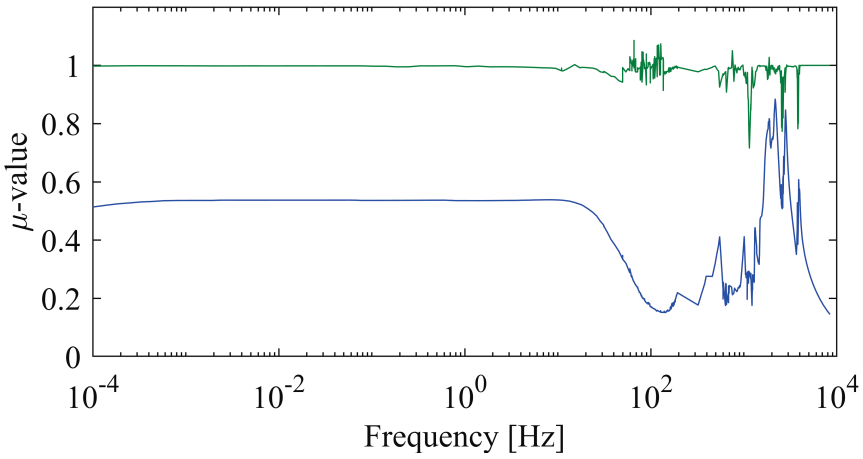

Figure 26: μ-value comparison of the closed loop system w\ (blue) and w\o (green) the controller perturbation block

The bounds defined by the controller perturbation block is shown in Figure 27 for one of the controller channels. If a controller's dynamic response lies within the region, the said controller achieves robust performance once implemented.

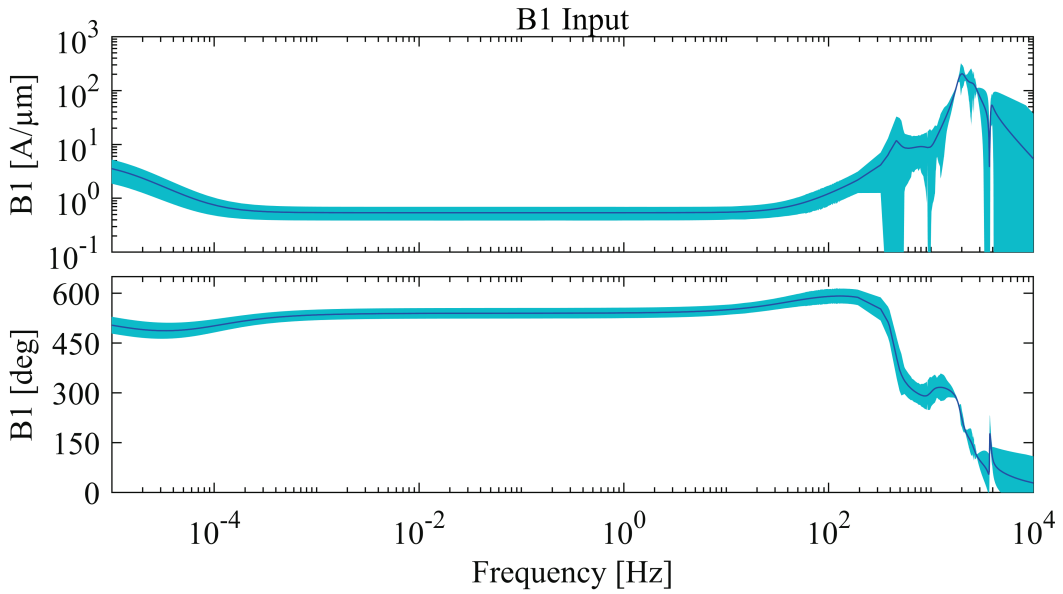

Figure 27: Bounds on the controllers B1-B1 channel defined by the perturbations

Once the perturbation block is defined, the next step was to determine the feasible dual-rate configurations by checking the frequency responses of possible dual-rate configurations to the bounds defined by the perturbation block. Table V shows the considered dual-rate configurations, along with the normalized computational cost. The dual-rate configurations with dynamic responses within the bounds are highlighted green, and outside the bounds are highlighted red. From Table V, the configuration that achieved the most computational saving while maintaining robust performance was identigied as the 40x-2 configuration with a 9% reduction in computational cost, where the two modes that are considered in the slow modes are the low-frequency modes that were meant to mimic integral action. In addition, up to 40 times slower rates were considered as the maximum ratio between fast and slow mode implementation rates since only 40 MAC operations were necessary for the first two modes.

Table V: Dual-rate implementation feasibility and computational cost for 300 kW turbine generator

Number of Modes in Slow Modes	Highest Natural Frequency in Slow Modes [Hz]	Maximum Singular Value / Normalized Computational Cost			
		1x 12.5 kHz	2x 6.25 kHz	3x 4.16 kHz	40x 312.5 Hz
0	-	1.00	1.00	1.00	1.00
2	$1.16*10^{-5}$	1.00	0.95	0.94	0.91
3	419	1.00	0.93	0.90	0.86
4	528	1.00	0.90	0.87	0.81
21	3843	1.00	0.50	0.33	0.03

For the redesign of the controller approach, each row of the controller transfer matrix was examined to identify the negligible channels in the context of robust performance. The procedure is demonstrated below for the first row.

Let $a(\omega) = \sigma([K_{11}\ \ K_{12}\ \ K_{13}\ \ K_{14}])$ be the singular values of the first row of the controller. The first thing to check is if including only the diagonal element would satisfy inequality (15). For this purpose, let $b_1(\omega) = \sigma([K_{11}\ 0\ 0\ 0])$. Figure 28 is the graphical representation of the inequality. The figure shows that neglecting everything but the diagonal term of the controller is sufficient to achieve robust performance for the first row of the controller. For demonstration purposes, let $b_2(\omega) = \sigma([K_{11}\ 0\ K_{13}\ 0])$, where K_{13} is the channel for the other AMB in the same plane. The graphic representation of the inequality (15) for $b_2(\omega)$ is also shown in Figure 28. This demonstrates that including more channels reduces the magnitude of the error, as expected.

The same analysis was repeated for the rest of the rows of the controller, which resulted in similar conclusions where only the diagonal terms were deemed necessary to achieve robust performance. This implied that a decentralized controller that has the same dynamic response as the diagonal channels of the μ-controller could provide the same

robust performance. For this reason, although the controllers' order was reduced previously, balanced truncation was applied again to each diagonal channel of the μ-controller individually to further reduce the controller order. In the first application of the model reduction, the model needed to match all 16 channels simultaneously, whereas in this case, it only needed to match one channel at a time. Each diagonal channel transfer function was reduced to orders 18, 22, 17, and 21 with minimal distortion to the dynamic response. The orders were chosen by manual inspection of the frequency responses. The redesigned controller was 72-order and required 306 MAC operations. Although the order of the controller increased, the necessary MAC operations decreased due to the decoupled nature. Figure 29 shows the μ-value plot of the 42-order controller and the redesigned 72-order controller.

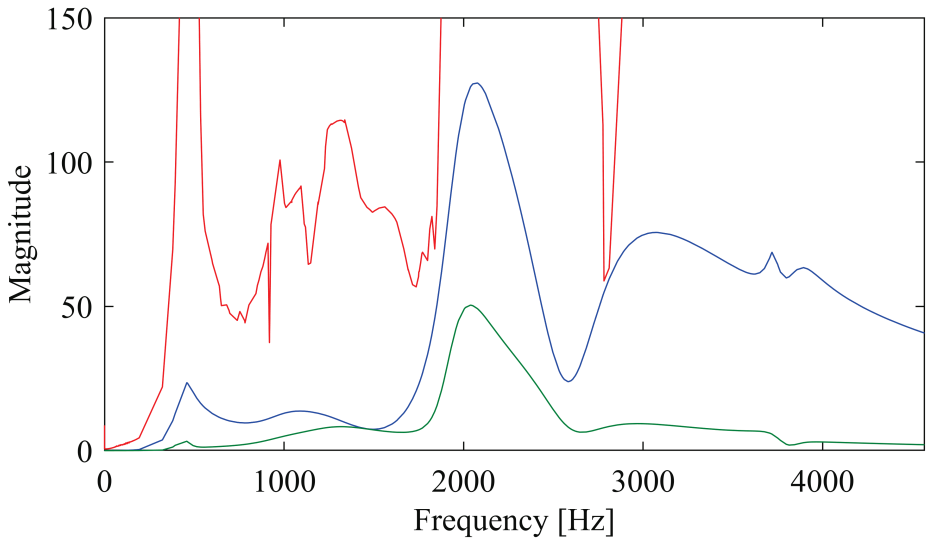

Figure 28: Graphic representation of inequality (15) for the first row of the controller; bounds $\pm\mathrm{p}(\omega)$ (red), error $a(\omega) - b_1(\omega)$ (blue), and error $a(\omega) - b_2(\omega)$ (green)

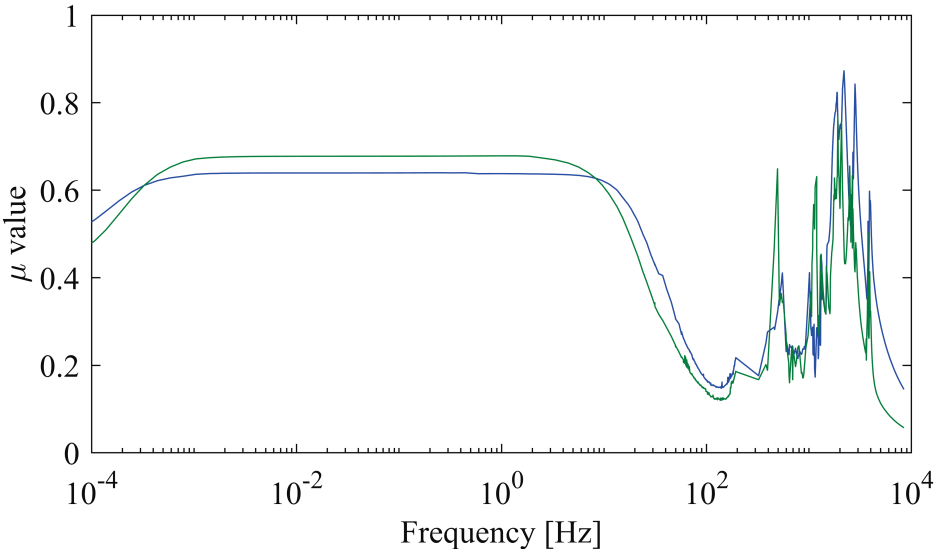

Figure 29: μ-value of the closed-loop system with the 42-order controller (blue) and with the redesigned controller (green)

There is a slight increase in the μ-value with the redesigned controller. However, the overall μ-value does not significantly change. More importantly, it always stays below unity, indicating robust performance. The increase in the μ-value at low frequencies can be explained by the lack of crosstalk. Figure 30 shows the achieved sensitivity function with the redesigned controller using the nonrotating nominal plant model. There are some minor differences in the achieved sensitivity function compared to the original controller. However, the difference does not violate the performance criteria, as concluded with the proposed method.

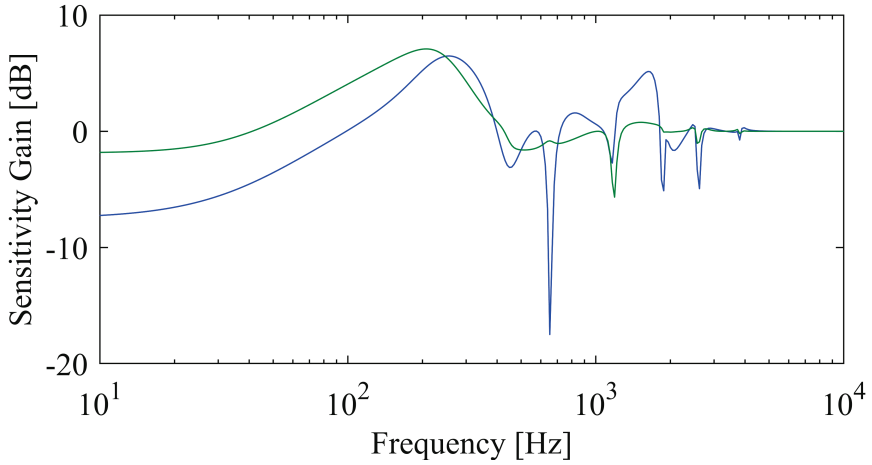

Figure 30: Sensitivity function of Calnetix turbine generator with the redesigned controller; B1 (blue) and B2 (green)

A Simulink model was created to compare the system response with the three controllers presented so far, i.e., the 42-order controller obtained via balanced truncation, the 40x-2 dual-rate implementation, and the redesigned controller. Each controller was discretized at 12.5 kHz, while the slow modes were discretized at 312.5 Hz. MATLAB built-in solver *ode15s* was used to simulate the system responses.

The first test was performed to compare the closed-loop system response to a step trajectory input to drive the system to 1 V. This is analogous to the initial levitation of the rotor. A random nonrotating model was chosen from the set of uncertain models, and the same model was used for all three controllers. The responses of the closed-loop systems are shown in Figure 31. The response of the 42-order controllers single-rate and dual-rate implementations are identical, whereas the redesigned controller differs from them significantly for the B1 bearing. Both 42-order controller and dual-rate controller seems to have a more aggressive response, but the settling time of each controller seems to be similar. Steady-state error is slightly larger with the redesigned controller. The steady-

state error can be reduced by feeding the trajectory signal to a low order filter before supplying it to the closed-loop system to adjust the DC gain of the closed-loop system. This would slightly increase the overall computational cost due to the computations for the additional filter.

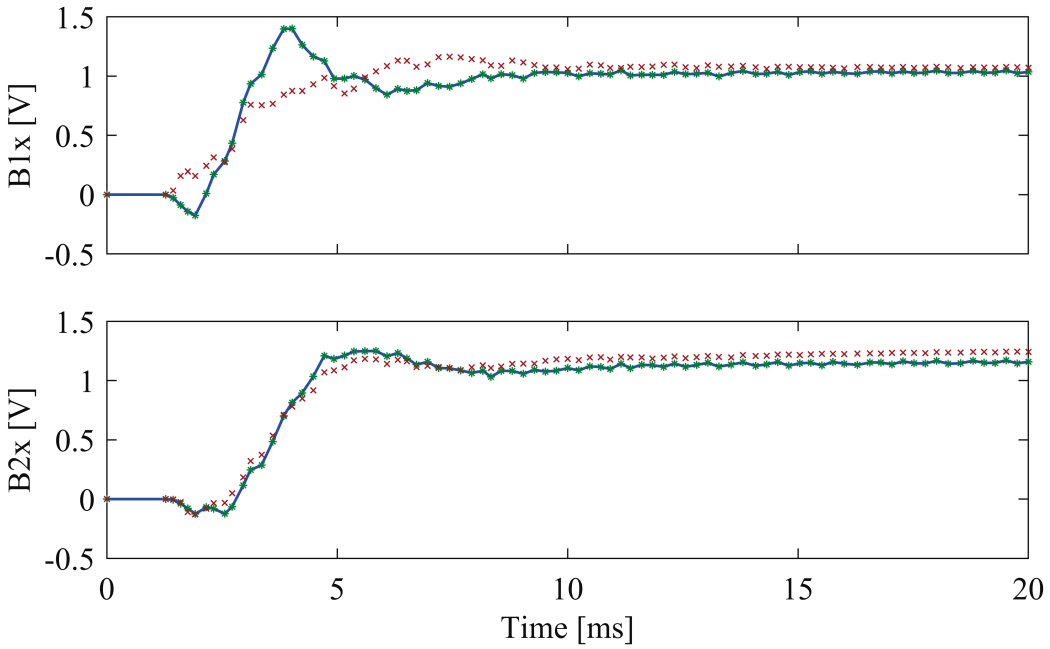

Figure 31: Step response of the closed-loop 300 kW turbine generator model with 42-order controller (blue-line), dual-rate controller (green-star), and redesigned controller (red-cross)

The second test was performed to compare the closed-loop system responses to periodic disturbance forces, analogous to unbalance force. A random plant model with 100 Hz rotational speed was chosen from the uncertain set of plant models to form the closed-loop systems. The disturbance forces were applied at actuator positions at a frequency of 100 Hz and a magnitude of 1 V with a 90-degree phase difference between the perpendicular control axes of AMBs. The same model was used for all three controllers. The outputs of each closed-loop system are shown in Figure 32. The single-

rate and dual-rate implementations of the controller gave identical results, as expected since the change in the dynamic response of the controller due to dual-rate implementation was negligible for this case. The redesigned controller differed from them in both magnitude and phase. Given the difference in achieved sensitivity functions between the 42-order controller and the redesigned controller, identical closed-loop behavior was not expected.

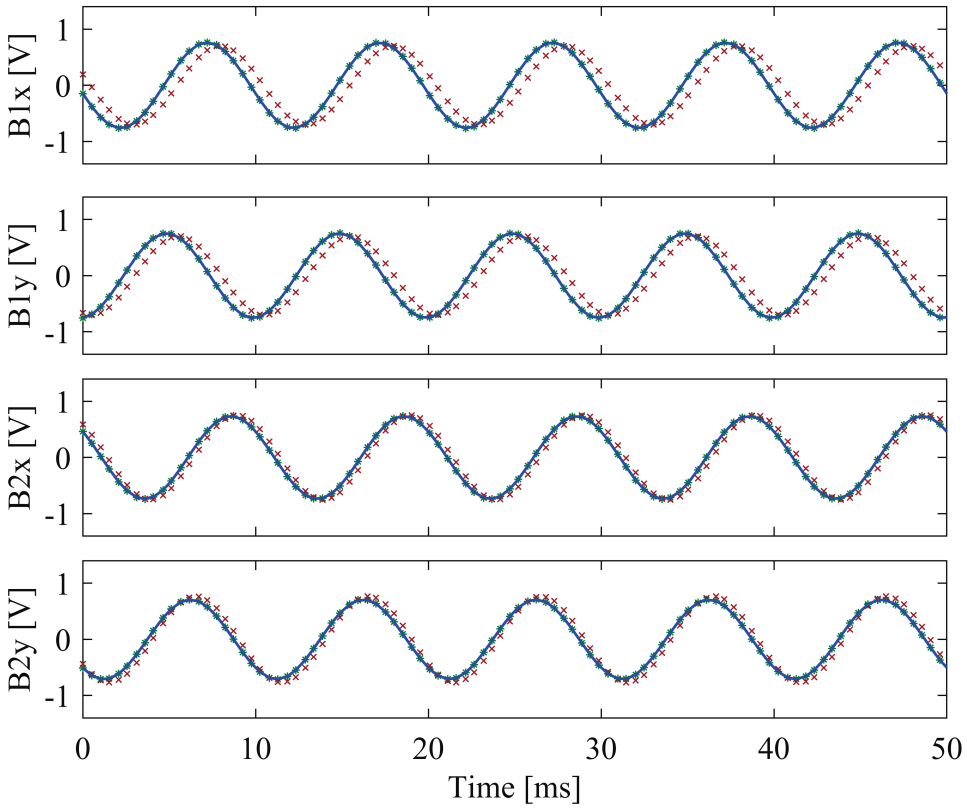

Figure 32: Force response of the closed-loop 300 kW turbine generator model with 42-order controller (blue-line), dual-rate controller (green-star), and redesigned controller (red-cross)

Significant computational cost reduction was achieved with the proposed methods without losing robust performance, especially with the redesigned controller. The

necessary number of MAC operations to run the controller was reduced by 9% with the dual-rate implementation and 27% with the controller redesign approach. Both proposed approaches provided similar desired robust performance and are a viable option.

4.3 HSM AMB Spindle, Dual-rate Controller Implementation and Redesign of Robust Controller via Controller Perturbation

A μ-controller was synthesized for the HSM AMB spindle. First, model uncertainties that are common for AMB systems were defined as the model uncertainties, i.e., 1% for flexible mode frequencies, 30% for flexible mode damping, 5% for current stiffness, 10% for position stiffness, and the rotational speed to cover the whole operating range from 0 rpm to 50,000 rpm. System-specific performance criteria were defined in a disturbance rejection scheme using signal-based control problem formulation. For this purpose, disturbance forces were defined at AMB actuator locations and tool-tip, and the vibration levels at sensor locations and tool-tip were chosen to be regulated without saturating the actuators. The *dksyn* function of MATLAB was used to synthesize the controller, which resulted in a controller of order 72 with an achieved μ-value of 0.71. Through balanced truncation, the order of the controller was reduced to 32, which was the smallest order of the controller that kept the μ-value below unity. 320 MAC operations were necessary for the single-rate implementation of the controller in modal canonical form and using the sparse matrix algebra. The number was used to normalize the computational cost.

After designing a controller to achieve the desired performance, dual-rate implementation was investigated first to realize computational savings. For this purpose, the controller perturbation magnitudes at each frequency were found via a bisection

algorithm. Figure 33 shows the bounds defined by the controller perturbation block on the V13-V13 channel. As stated before, if the response of a dual-rate configuration of the controller stays within these bounds, the said controller would achieve robust performance.

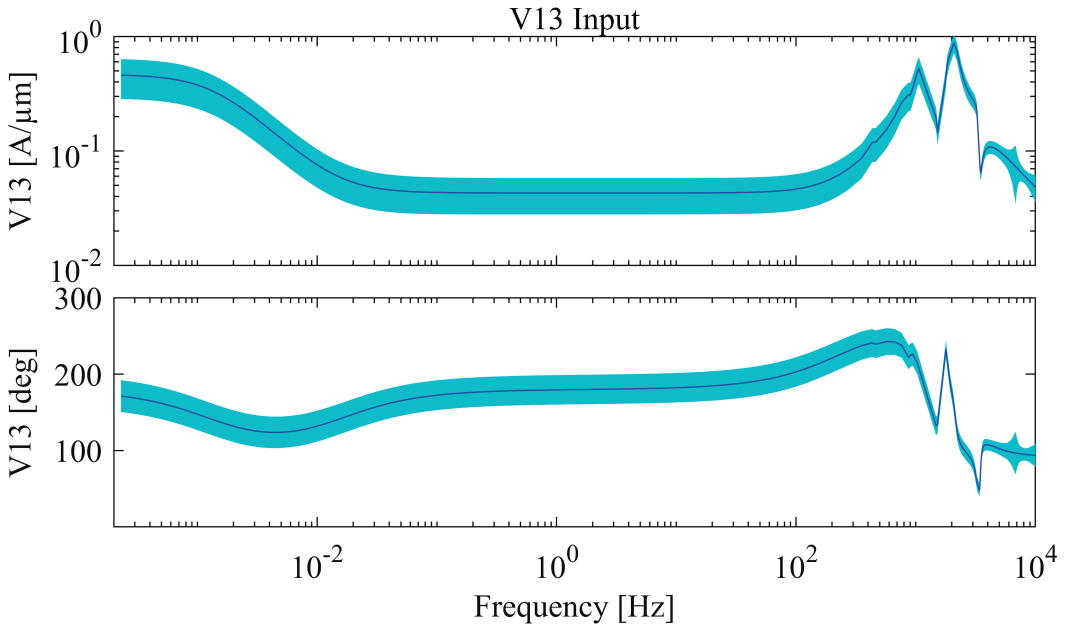

Figure 33: Bounds on the controllers V13-V13 channel
defined by the controller perturbation

The next step in the dual-rate implementation approach was to identify the feasible dual-rate configurations and to check the dynamic responses of the dual-rate configurations with the bounds to determine if they maintain the robust performance. Table VI shows the considered dual-rate configurations with their normalized computational cost. The configurations which had their response lie within the bounds are highlighted green, and the ones that lie outside at some points are highlighted red. From Table VI, it was concluded that the configuration 40x-2 would result in the most

computational savings, a 12% reduction in computational cost, while maintaining robust performance.

Table VI: Dual-rate implementation feasibility
and computational cost for the HSM AMB spindle

Number of Modes in Slow Modes	Highest Natural Frequency in Slow Modes [Hz]	Maximum Singular Value / Normalized Computational Cost			
		1x 10 kHz	2x 5 kHz	3x 2.5 kHz	40x 250 Hz
0	-	1	1	1	1
2	0.0014	1	0.94	0.91	0.88
3	877	1	0.91	0.86	0.82
4	880	1	0.87	0.81	0.76
16	3811	1	0.50	0.25	0.03

The redesign of the controller approach was also applied to HSM AMB spindle. The channels that were not necessary for robust performance were identified via removing one channel at a time from each row of the controller and using inequality (15) for robust performance assessment, similar to the previous study on the 300 kW turbine generator. Through repeating the procedure for all four rows of the controller, it was found that the crosstalk channels between the perpendicular planes, V- and W-planes, of the system were not necessary. Moreover, the controller for V-plane was identical to the controller of W-plane. That is why a controller model was fit to the V-plane control channels through the application of balanced reduction to the controller once again. This process resulted in a 16-order controller for V-plane, and an identical controller was used for the W-plane. The order was chosen such that distortions to dynamic response for the respective channels were minimal by manual observation. The new controller was of order 32 and required 188 MAC operations. Although the order stayed the same, the

required number of MAC operations decreased by 41% due to the decoupled nature of the redesigned controller.

The theoretical results indicated that all three controllers, i.e., single-rate and dual-rate implementation of 42-order controller, and the redesigned controller, would maintain robust performance, while each of them having a different computational cost. Experimental verification of the theoretical results was done via comparison of CPU time, transfer function at tool-tip via impact hammer test, and orbit sizes at 20,400 rpm. For this purpose, each controller was implemented via dSPACE 1005 system using 10 kHz sampling rate, where the slow mode of dual-rate configuration was implemented at 250 Hz with interlacing technique.

The first test was performed to compare the computational cost of each controller via the amount of CPU time spend for their respective matrix-vector algebra, as shown in Figure 34. The single-rate implementation of the controller took around 1.67 μs, dual-rate implementation took around 1.51 μs, and the redesigned controller took around 0.83 μs. The experimental results are in line with the theoretical results, with slightly better results for the redesigned controller. The discrepancy in the theoretical reduction and observed reduction can be explained by the low-level optimization done by the software in implementation.

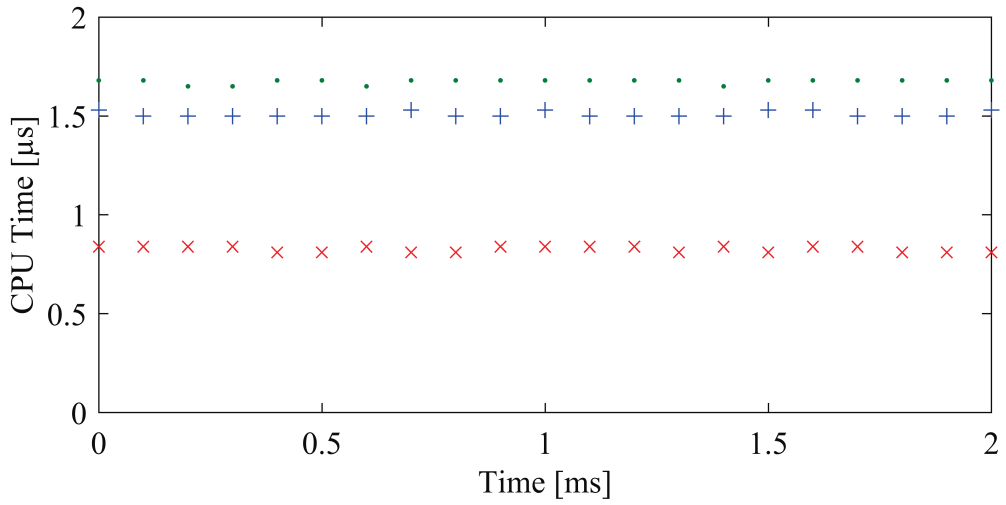

Figure 34: CPU time comparison of the single-rate (green-dot) and dual-rate implementation (blue-plus), the redesigned controller (red-cross)

The second test was performed to compare the tool-tip compliance with each controller. Since the system is a machining spindle, tool-tip compliance is an important performance indicator and provides feasible machining operation parameters. The compliance of the tool-tip was measured by using an external capacitance-based displacement sensor, along with an impact hammer. The setup for the experiment is shown in Figure 35. The force and displacement measurements were fed to an HP 25670 signal analyzer to convert the readings to transfer functions, where an average of 10 measurements was used for each controller. Figure 36 presents the resulting frequency responses of the closed-loop system at tool-tip with the three controllers, along with their respective coherence plots. Identical compliances were observed with all three controllers, indicating each controller resulted in the same closed-loop dynamics.

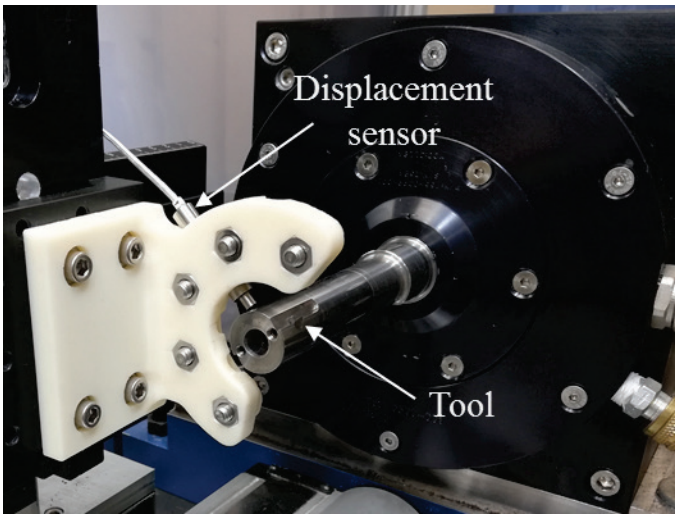

Figure 35: Impact hammer test setup

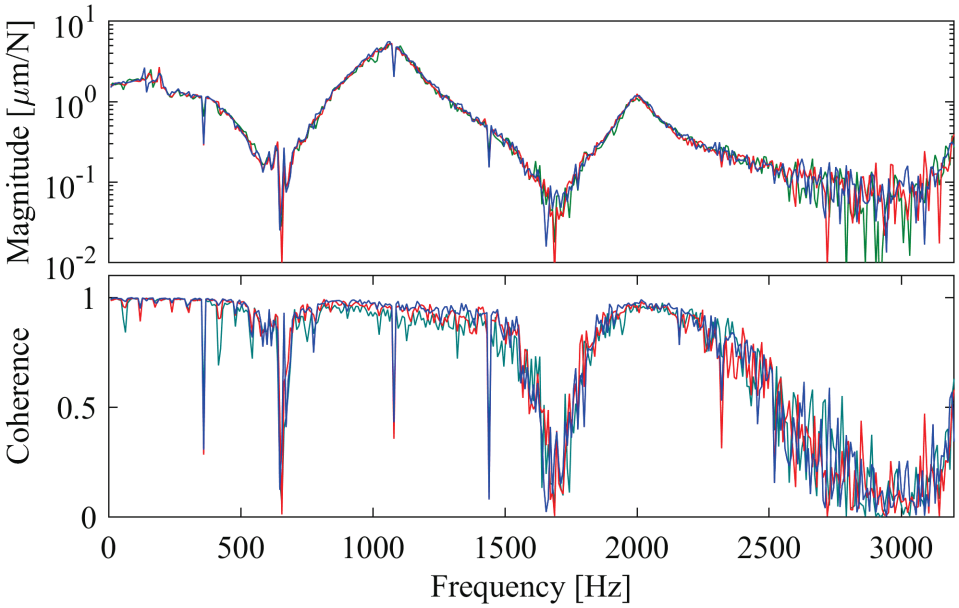

Figure 36: Closed-loop tool-tip frequency response with single-rate (green) and dual-rate (blue) implementation of the controller, and redesigned controller (red)

The last experiment was performed to observe the orbit sizes and shapes while the rotor was rotating at 20,400 rpm, without machining. The chosen rotational speed is above the first two rigid mode critical speeds but below the first bending mode critical

speed. The main disturbances acting on the system during the experiment were the unbalance forces due to mass eccentricity and the unbalance magnetic pull due to asymmetry in the magnetic field between the rotor and motor stators. The orbits are shown in Figure 37. All three controllers achieved similar size and shape orbits, with single-rate implementation slightly differing from them at the front bearing. The difference might be due to the nature of experimental work. However, slight differences are expected with the proposed methods since the methods are meant to make sure robust performance is maintained rather than achieving identical dynamics.

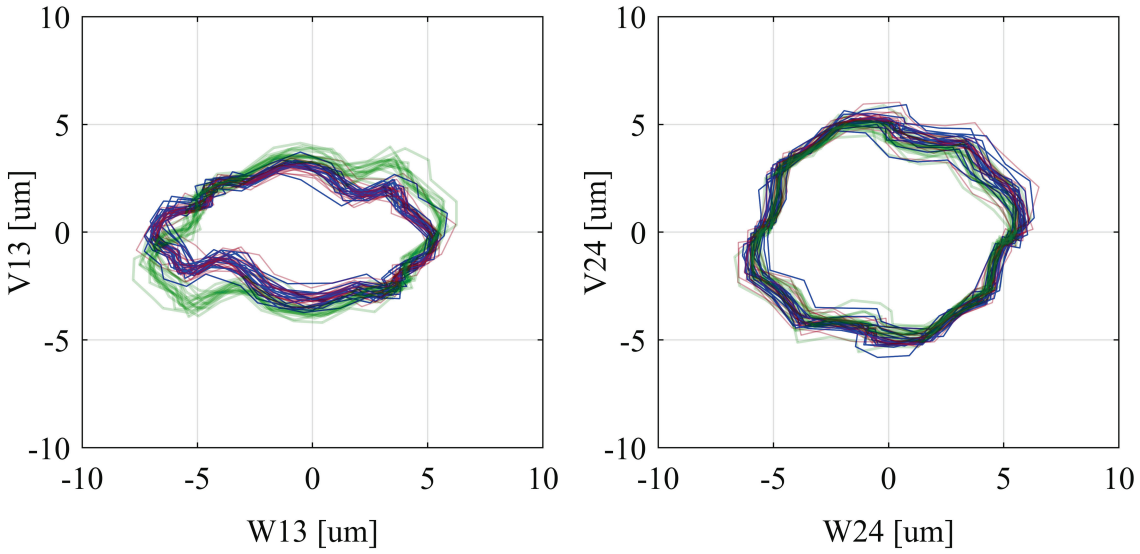

Figure 37: Orbit size at 20,400 rpm with single-rate (green) and dual-rate (blue) implementation of the controller, and redesigned controller (red)

CHAPTER V

PERFORMANCE-DRIVEN GYROSCOPIC EFFECT COMPENSATION VIA ADD-ON CONTROLLER AND ITS EFFECTS ON ROBUST CONTROLLER DESIGN AND IMPLEMENTATION

The performance of robust controllers can be improved by introducing an add-on controller to address a specific task. For AMB systems, the add-on controllers are designed either to reject disturbance forces [51-56] , or to compensate the gyroscopic effects for rigid rotor-AMB systems [57, 58]. By introducing an add-on controller for gyroscopic effect compensation, the robustness requirements in the performance controller design can be relaxed, enabling a potential increase in the achievable performance. This section presents a novel approach for gyroscopic effect compensation for flexible rotor-AMB systems and investigates its effects on the robust controller design and achieved performance.

5.1 Add-on Controller for Gyroscopic Effect Compensation

The reduced-order equation of motion of an AMB-rotor system in modal coordinates can be written as

$$\begin{aligned} M_m\ddot{q}_m + (D_m + G_m(\omega))\dot{q}_m + K_m q_m &= B_m(K_x q_m + K_i i_c \ ) \\ y &= C_m q_m \end{aligned} \tag{16}$$

where q_m is the modal states of the rotor, M_m is the modal mass matrix (e.g., identity matrix with appropriately chosen coordinate transformation matrix), K_m is the modal stiffness matrix that presents information on the natural frequencies of the system, D_m is the modal damping matrix, G_m is the skew-symmetric modal gyroscopic matrix, B_m is the input matrix that defines the effects of inputs on the modes of the system, K_x and K_i are the matrices of appropriate size and structure for the AMB force constants, and C_m is the modal output matrix that constructs the position of the rotor at the AMB sensor positions from the modal displacements.

The effects of the gyroscopic matrix, G_m can be compensated with an appropriately chosen control current i_c as

$$i_c \ = \ (B_m K_i)^{-1} G_m(\omega)\dot{q}_m \tag{17}$$

The control law in Eq. (17) is the basic idea behind the cross-feedback control introduced in [57] to compensate the gyroscopic effects in rigid-rotor AMB systems. In order to derive the control law, the necessary inverse needs to exist. The inverse only exists if the AMB system has the same number of modes as the number of radial AMBs.

For AMB systems with two radial AMBs, the inverse only exists when rigid rotor assumption holds. That is why the control law in Eq. (17) in its current form cannot be used for the flexible rotor-AMB systems. However, the control law can be modified to remove the effects of the gyroscopic matrix for selected modes of the system. This can be accomplished by using a modified B_m matrix, where only the rows corresponding to the selected modes remain. The modified version of the control law can compensate the gyroscopic effects for *n* modes of the system, where *n* is the number of radial AMBs in the system. The modified control law can be written as

$$i_c = K_i^{-1}\tilde{B}_m^{+}G_m(\omega)\dot{q}_m = T(\omega)\dot{q}_m \tag{18}$$

where $\tilde{B}_m$ is the modified B_m matrix, and $\tilde{B}_m^{+}$ is the pseudoinverse of the matrix. It is important to note that the control law shown in Eq. (18) relies on the modal state information, namely $\dot{q}_m$. However, $\dot{q}_m$ is not readily available from the sensor information. That is why a modal state observer is necessary for implementation. Kalman estimator is used in this research with the estimator equation as

$$\dot{\hat{q}} = A\hat{q} + Bi_c + L(y - C\hat{q}) \tag{19}$$

with

$$A = \begin{bmatrix} 0 & I \\ -M_m^{-1}(K_m - K_x) & -M_m^{-1}(D_m + G_m(\omega)) \end{bmatrix}, \quad B = \begin{bmatrix} 0 \\ B_m K_i \end{bmatrix} \tag{20}$$

where $\hat{q}$ is the estimated modal states, and L is the filter gain designed to achieve optimal state estimation with imperfect information which is calculated via the *kalman* function

of MATLAB [73]. The block diagram of the add-on controller and its implementation is shown in Figure 38. With the add-on controller, the gyroscopic effects of the selected modes are compensated from the controller perspective, i.e., the open-loop system dynamics from input u to output y in Figure 38. That is why the performance controller can be designed with a modified open-loop system model with a reduced gyroscopic matrix to relax the robustness requirements and potentially achieve better performance.

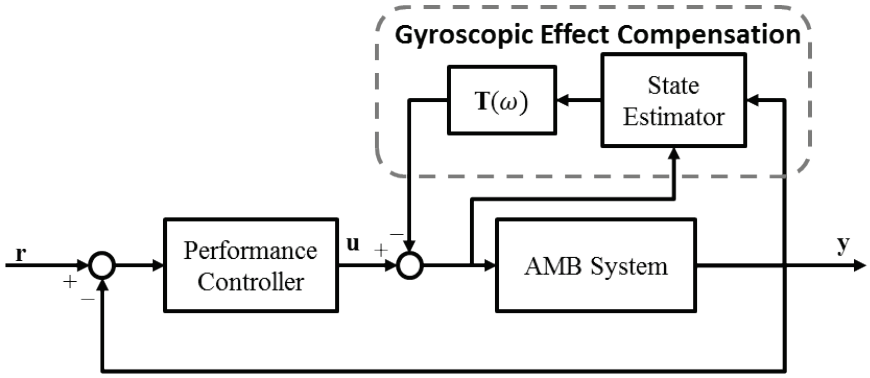

Figure 38: Gyroscopic effect compensation with and add-on controller

There are a few limitations of the proposed method to design an add-on controller for gyroscopic effect compensation. First, the method only considers the effects of the add-on controller on the selected modes of the system, and its effects on the other modes are not taken into account in the design process. The add-on controller might get rid of the frequency bifurcation at the selected modes as per the design objective at the expense of altering the dynamics of other modes. That is why, before implementation, the effects of the add-on controller on the whole system dynamics need to be determined analytically to make sure the add-on controller does not significantly affect the other modes. Second, the method relies on the observability and controllability of the selected modes. That is why

if one of the AMBs is located near a node of the system, the necessary inverse might not exist. Hence the add-on controller for gyroscopic effect compensation cannot be applied.

5.2 Application of the Gyroscopic Effect Compensation

The proposed add-on controller for gyroscopic effect compensation was applied to the AMB test rig shown in Section 2.2.1. For the system, gyroscopic effects had negligible effects on the first and second flexible mode of the system, as seen by the lack of bifurcation of the first and second flexible mode frequencies in Figure 8. However, both third and fourth flexible modes exhibited significant bifurcation. Hence, gyroscopic effect compensation was applied to third and fourth flexible modes.

As mentioned previously, the design of the compensation neglects the effects of the add-on controller on the other modes. That is why the effects of compensating third and fourth flexible modes individually and simultaneously were analyzed analytically before implementation. For this reason, a Kalman estimator was designed to estimate the necessary state information via choosing a diagonal Q and R matrices with appropriate values that represented the variance of the process noise and measurement noise, respectively. The Kalman estimator was tested experimentally to confirm the accuracy of the estimation by comparing the observer outputs for AMB sensor positions to the AMB sensor outputs. The outputs of the estimator and physical system, while the system ran at 3,000 rpm, is shown in Figure 39 for one of the output channels. The main disturbance forces acting on the system during rotation were the unbalance forces due to mass eccentricity and forces due to the misalignment of the motor center and bearing centers. The error in output estimation stayed below 2 μm, as seen in the figure. Considering the

noise levels of the system, which was around 1 μm, it is concluded that the designed estimator could provide accurate modal state estimations.

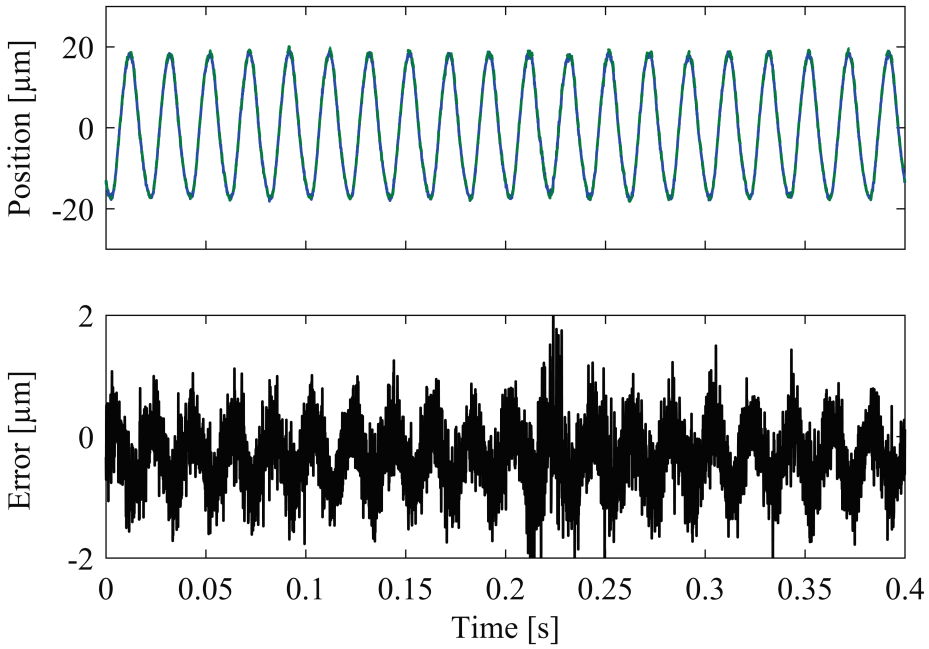

Figure 39: Comparison of estimator output (green) and AMB system (blue) at 3,000 rpm

After the design of the modal state estimator, three cases were examined analytically: 1) compensating only the third flexible mode, 2) compensating only the fourth flexible mode, and 3) compensating both the third and fourth flexible modes simultaneously. For each case, the compensated open-loop system was obtained by connecting the Kalman estimator and the modal feedback gain to the open-loop system model. The analysis was done for both a perfect estimator, where the system matrices used for the AMB system and the estimator were identical, and an imperfect estimator, where the AMB system matrices were randomly chosen from the set of uncertain plant models.

First, the compensation of the third flexible mode was analyzed. The modal feedback gain, T(ω), was designed using the fifth row of the B_m matrix. The bode diagram of the

open-loop system at 3,000 rpm for the perfect estimator case is shown in Figure 40a for one of the planes. The add-on controller eliminated the bifurcation of the third flexible mode as expected. The effects of the add-on controller on the other modes can also be observed in the figure. The bifurcation of the fourth flexible mode slightly increased with the add-on controller. The effects were relatively negligible for the first and second flexible modes, where neither the bifurcation amount nor the peak magnitudes changed. The bode diagram of the open-loop system at 3,000 rpm for the imperfect estimator case is shown in Figure 40b for one of the planes. The figure shows that the add-on controller for gyroscopic effect compensation tolerates typical inaccuracies in AMB system models. However, a slight change in the modal damping of the fourth flexible mode and a slight bifurcation increase in the first flexible mode can be seen due to mismatch between the estimator and the AMB system matrices.

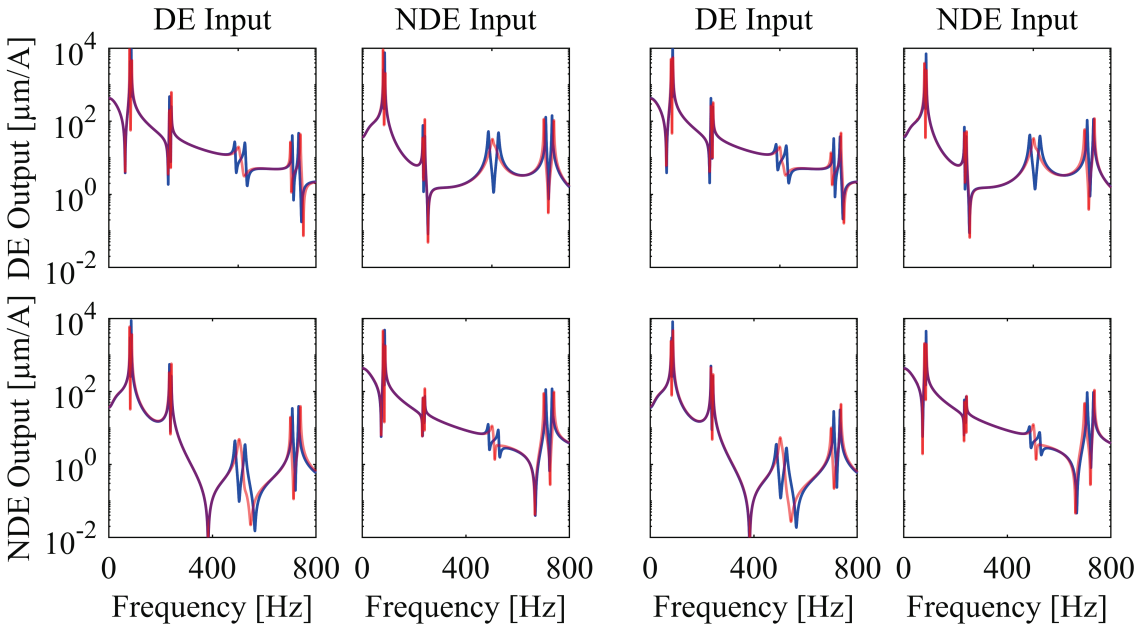

(a) with perfect observer (b) with imperfect observer

Figure 40: Analytical results of individual compensation of the third flexible mode at 3000 rpm; the system w/o the compensation (blue), w/ the compensation (red)

The same analysis was done for individual compensation of the fourth flexible mode, where the modal feedback gain was constructed using the sixth row of the B_m matrix. The conclusion of the analysis for compensation of the fourth flexible mode was the same as the conclusions from the compensation of the third flexible mode. The add-on controller was able to compensate the gyroscopic effect for the fourth flexible mode, where the bifurcations were eliminated for the fourth flexible mode without significant effect on the other modes. Using a different model for the estimator and AMB system to mimic reality did not affect the conclusions significantly.

However, the compensation of the third and fourth flexible modes simultaneously significantly increased the bifurcations of the first and second flexible modes, as shown in Figure 41. The add-on controller eliminated the bifurcations of both the third and fourth flexible modes. However, it significantly altered the dynamics of the first and second flexible modes, as seen from the significant increase in the bifurcations and the change in the peak magnitudes. This is not desirable since the aim is to reduce the overall robustness requirements. This is one of the limitations of the method where each AMB system needs to be analyzed individually to determine which modes can be selected for the gyroscopic effect compensation.

Given the analytical results, it was clear that individual compensation of the third and fourth flexible modes were feasible options, while simultaneous compensation of the third and fourth flexible modes was not. That is why two cases, i.e., individual compensations of the third and individual compensation of the fourth flexible modes, were pursued experimentally. For this reason, a PID controller was designed for the system that can provide stable levitation and rotation up to 3,000 rpm. For each case, the

closed-loop system identification technique described in the previous sections was used to obtain the open-loop FRD for the compensated cases at 2,000 and 3,000 rpm, which represents the dynamics from the controllers' perspective, i.e., from input u to output y in Figure 38.

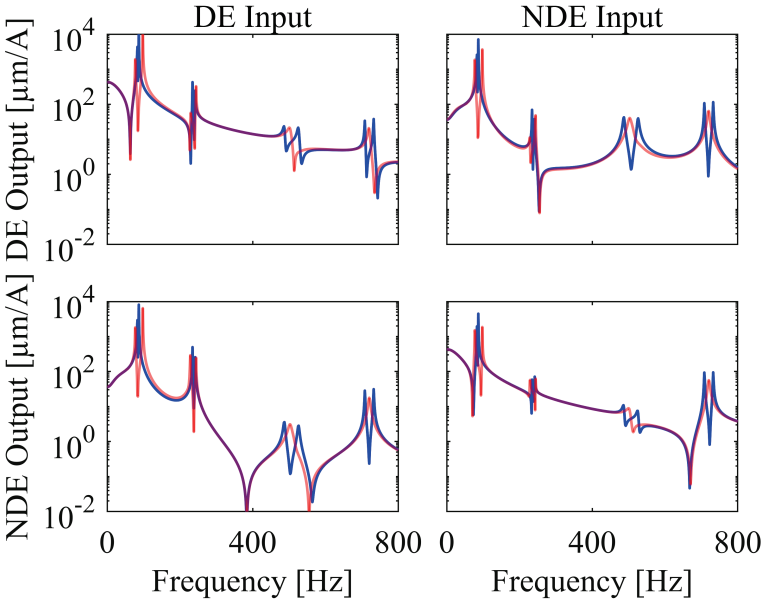

Figure 41: Analytical results of simultaneous compensation of the third and fourth flexible modes with the perfect model at 3000 rpm; the system w/o the compensation (blue), the system w/ compensation (red)

Figure 42 shows the open-loop FRD comparison of the AMB system with and without the add-on controller for gyroscopic compensation for the third flexible mode at 2,000 and 3,000 rpm. The experimental results are in line with the analytical conclusions. The bifurcation of the third flexible mode frequency was eliminated. The compensation had relatively small effects on the other modes. The most significant effect was the increase in the amplitude at the fourth flexible mode frequency, an indication of reduced modal damping. However, no noticeable increase in vibration amplitudes, instability, or audible noise was observed.

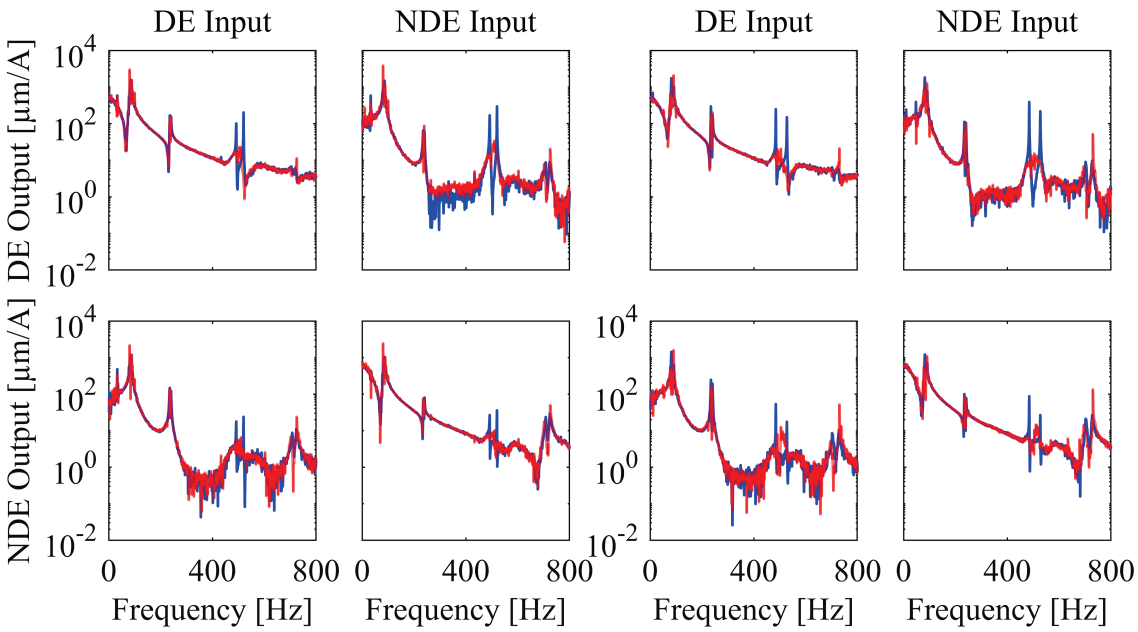

Figure 42: FRD comparison of the AMB system with (red) and without (blue) the add-on controller for gyroscopic effect compensation of the third flexible mode

Similar conclusions were obtained for the individual compensation of the fourth flexible mode. Figure 43 shows the open-loop FRD comparison of the AMB system with and without the add-on controller for gyroscopic effect compensation at 2,000 and 3,000 rpm. The add-on controller eliminated the bifurcation at the fourth flexible mode frequency. However, there were slight amplitude changes in the other modes, an indication of reduced modal damping.

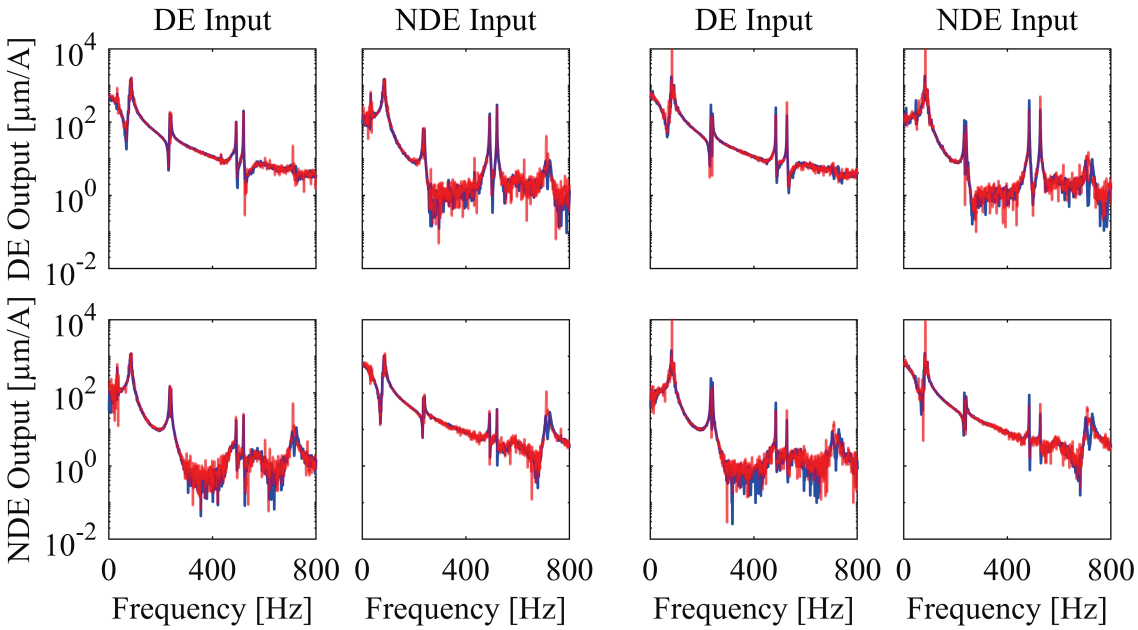

Figure 43: FRD comparison of the AMB system with (red) and without (blue) the add-on controller for the gyroscopic effect compensation of the fourth flexible mode

5.3 Effect of Gyroscopic Effect Compensation on Controller Design and Implementation

The effectiveness of the add-on controller to compensate the gyroscopic effects for the selected modes is shown in the previous section. That is why the controller design procedures can be modified to include the effects of the add-on controller on the system dynamics by reducing the values in the gyroscopic matrix rows that correspond to the compensated modes. This would reduce the robustness requirements in the control problem formulation and, in theory, increase the achievable performance.

A new rotor configuration was used for the AMB test rig, as shown in Figure 44, to investigate the effects of compensating the gyroscopic effects of selected modes on the designed controllers [60]. The new configuration included an overhang disk to achieve a

relatively high gyroscopic effect presence. The rotor was still supported by two radial AMBs and one thrust AMB. The DE side AMB control axes are referred to as V13-W13, and NDE side control axes are referred to as V24-W24. The naming convention is changed to make it clear that the system is different from the one used previously.

Figure 44: The new configuration of the AMB test rig

The new configuration of the rotor was modeled by FEM first, and then modal model parameters were tuned for the rigid modes and the first three flexible modes to match the experimental FRD. For the radial AMBs, 1 A bias current was used, which resulted in force constants of 25.33 N/A and 0.064 N/μm. Through the examination of the model response and frequency response data, an unknown dynamic was identified around 400 Hz. The source of the unknown dynamics wasn't clear but assumed to be related to coupling between axial and radial dynamics, given that it is not affected by rotational speed. The unknown dynamics were modeled as a lightly damped second order system with no speed dependence, and its parameters were obtained via nonlinear least square optimization. Figure 45 shows the comparison of the model response and experimental FRD for both nonrotating and rotating at 3,000 rpm cases. The model matched the frequency response data relatively well, both in nonrotating and rotating at 3,000 rpm

cases. The flexible mode frequencies were on-point, the zero locations were accurate, and the model of the unknown dynamics at 400 Hz fitted well.

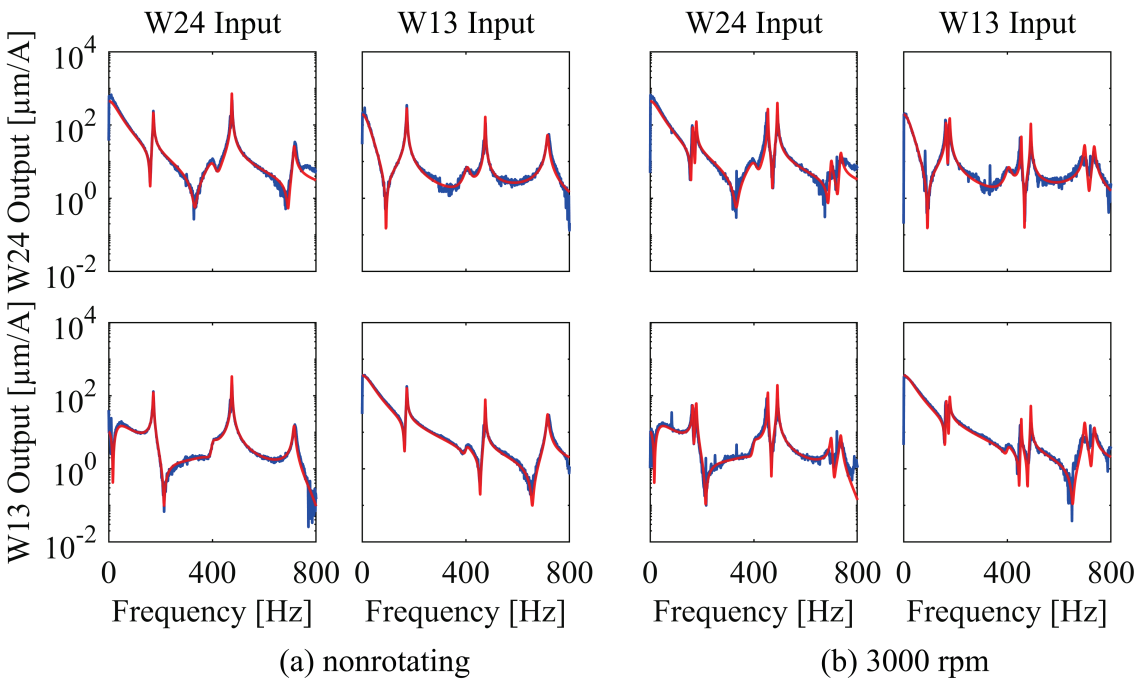

Figure 45: Comparison of the model response (red) and experimental FRD (blue)

The add-on controller was designed to compensate for the gyroscopic effects for the first and second flexible modes of the rotor since the first flexible mode frequency is around the maximum rotational speed of 10,000 rpm, and the second flexible mode exhibited large bifurcations. Figure 46 shows the experimental FRD of the system with and without the add-on controller at 4,000 rpm. The bifurcations of the first and second flexible modes were significantly reduced. However, the add-on controller did not eliminate the bifurcations. This was due to errors in state estimation and speed measurements. That is why the gyroscopic effects for the selected modes should not be removed entirely from the model but instead should be reduced significantly. In this

research, the values in the rows of the gyroscopic matrix that correspond to first and second flexible modes were reduced by 90% to allow a cumulative 10% error in state estimation and speed measurement.

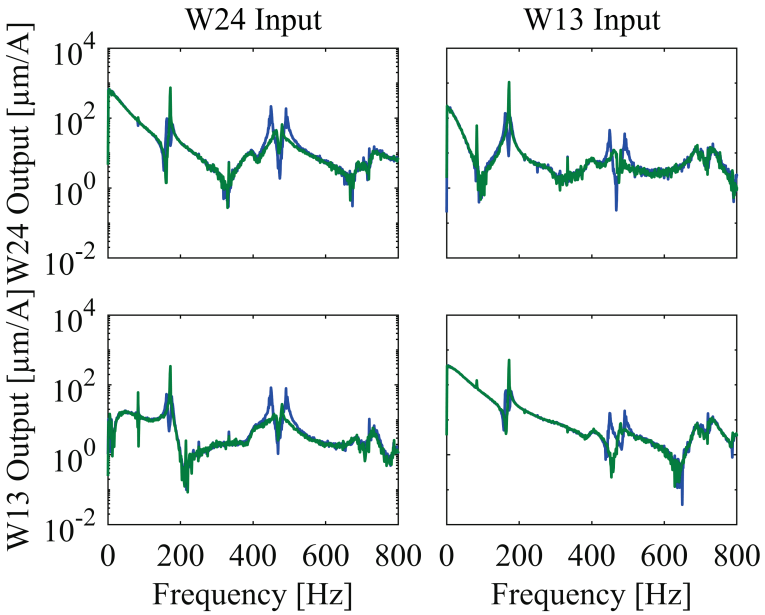

Figure 46: Effects of the add-on controller on the open-loop system dynamics at 4,000 rpm, w/o the add-on controller (blue) and w/ the addon controller (green)

Typical uncertainties were assigned to the model of the system for the robust control problem formulation, i.e., 1% uncertainty in flexible mode frequencies, 20% uncertainty in flexible modes modal damping values, 10% and 15 % uncertainties in the current and position stiffness values, and 100% uncertainty in rotational speed with 5,000 rpm nominal value to cover the full operating range of 0-10000 rpm. The performance criteria were chosen based on standard disturbance rejection problem where the goal was to keep the orbits within a certain radius without saturating the amplifiers in the presence of disturbance forces and sensor noise. Table VII shows the parameters for the weights.

Table VII: Performance specification

Weights	Low frequency	High frequency	Cross over frequency	Roll-off frequency
Disturbances	8 N	1 N	1 Hz	170 Hz
Noise	0.6 µm	0.6 µm	-	-
Vibrations	4 µm	80 µm	1 Hz	-
Control Mag.	1 A	1 A	-	400 Hz

The plant model was augmented with the performance weights to form the augmented plant model for the *dksyn* function of MATLAB [73]. Two controllers were designed for the AMB system: 1) standard μ-controller to serve as a benchmark controller, and 2) μ-controller that was synthesized using a modified plant model that had reduced value for the gyroscopic matrix to include the presence of the add-on controller.

For the first controller, the benchmark controller, a standard μ-controller was designed, which resulted in a controller of order 94 with an achieved μ-value of 0.94. The controller order was reduced to 62 via balanced truncation, where the order was chosen to keep the μ-value around 0.92. This controller is referred to as K_1. For the second controller, the model was modified to include the effects of the add-on controller for gyroscopic effect compensation. However, augmenting the add-on controller to the plant model increases the order of the model significantly, hence increases the order of the controller and the time to synthesize the controller, both of which are not desirable. That is why the effects of the add-on controller were mimicked by reducing the values of the gyroscopic matrix that correspond to the first and second flexible modes by 90% instead of augmenting the add-on controller with the plant model. The modified model was then augmented with the same weighting filters shown in Table VII. The modified augmented

plant model was then used to synthesize a μ-controller, resulting in a controller of order 92 with an achieved μ-value of 0.67. The controller order was reduced to 57 via balanced truncation, where the order was chosen to keep the μ-value around 0.67. This controller is referred to as K_2.

Figure 47 shows the comparison for the V13-V13 channels of controllers K_1 and K_2, which corresponds to one of the DE AMB control channels. The effects of using the modified model in the designed controller are apparent in the figure. Controller K_1 was designed without compensating the gyroscopic effects, hence had a notch filter like dynamic around the second flexible mode frequency that covered a broad frequency range to handle the bifurcation of the second flexible mode frequency. As for the controller K_2, the notch filter like dynamic was in a narrower frequency range since the bifurcations were reduced with the add-on controller. Moreover, the gain of the controller K_2 was slightly higher up-to 100 Hz, which might be due to the less restrictive robustness requirements. The low-frequency dynamics of both controllers were similar, since the add-on controller, or its effects, only affect relatively high-frequency dynamics.

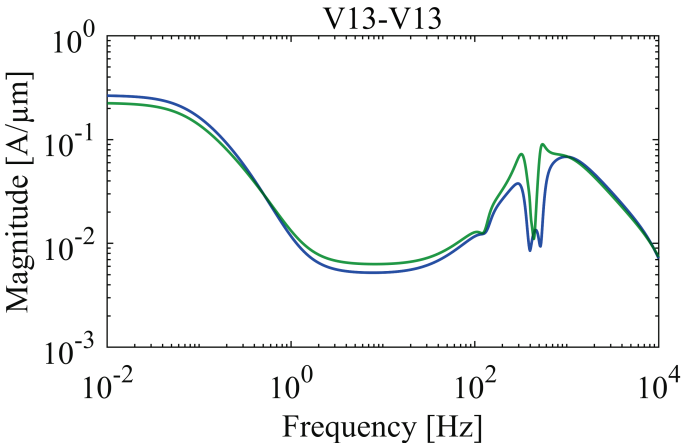

Figure 47: Frequency response comparison of controller K_1 (blue) and K_2 (green)

Both controllers, i.e., K_1 and K_2 with the add-on controller, were implemented via dSPACE MicroLabBox. Controllers K_1 and K_2, and the state-observer were discretized at 10 kHz using the zero-order hold (ZOH) method, and modal canonical form was used for the state-space realization to reduce the computational cost via enabling the use of sparse-matrix algebra algorithms.

The initial levitation trajectories achieved with both controllers are shown in Figure 48, where the system was energized after 1 sec. The rotor was manually positioned in similar initial resting positions before energizing the system to have a meaningful comparison. The VW13 channels' initial resting positions were relatively close to the bearing center due to the flexible coupling element slightly supporting the DE side. Since both controllers had similar low-frequency dynamics, the achieved initial levitation dynamics were similar as well. Both controllers provided relatively smooth levitation at each channel without significant overshoot or oscillations. Both controllers provided a stable levitation in the nonrotating case and achieved a settling time of around 0.75 seconds and had a steady-state error of less than 2 μm.

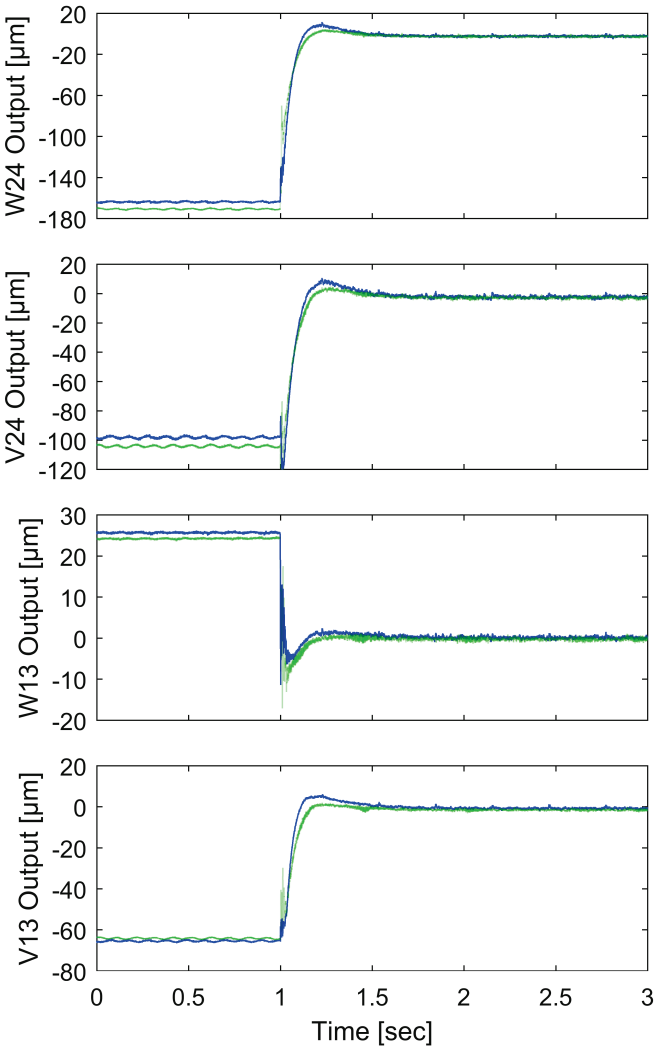

Figure 48: Initial levitation trajectory with K_1 (blue) and K_2 (green)

After confirming the controllers' stability in the non-rotating case, the next comparison was a run-up test. A run-up test is a relatively simple experiment that provides information on the achieved robustness and performance for the whole operating range. For the studied system, the system was run from 0 to 10,000 rpm with 200 rpm/sec acceleration while the displacement and control current magnitudes were observed. Figure 49 shows the observed displacements at each AMB sensor with respect to time.

Up-to 20 sec., i.e., 4,000 rpm, controller K_2 provided better performance, as indicated by the low vibration amplitudes. Then, the performance of both controllers became similar up-to 7,000 rpm. The performance of controller K_2 degraded significantly between 7,000 rpm to 9,500 rpm, which corresponds to 37 sec and 47 seconds, respectively. However, the performances of both controllers became quite similar at the maximum design speed of 10,000 rpm. The main reason behind the performance degradation of the controller K_2 was the error in the state-estimations. For an unidentified reason, the observer did not provide accurate output estimation between 7,000 rpm and 9,500 rpm. Figure 50 shows the observed control currents during the same run-up tests. For the controller K_2, control current refers to the sum of the output of the controller K_2 and the output of the add-on controller for the gyroscopic effect compensation. The main reason behind the relatively lower control currents at the VW13 channels, i.e., the DE side control channels, in both cases was the slight lift provided by the flexible coupling element that connected the rotor to the motor. This connection reduced the necessary current at the VW13 channels to overcome the weight of the rotor. Neither controller saturated the actuators during the run-up test, where the saturation would have happened if over 1 A control current magnitudes were demanded. Both controllers used similar control currents at low rotational speeds. However, at high rotational speeds, the control currents used by the controller K_2 was significantly higher, since control current required to compensate the gyroscopic effects increases with the rotational speed. The increased current magnitudes for operation was not desirable since it indicates higher power consumption. Also, the controller K_2 used almost 1 A magnitudes at high rotational speeds. That is why special care must be given to the desired control current magnitudes in the control problem

formulation to account for the necessary control current magnitudes for the gyroscopic effect compensation.

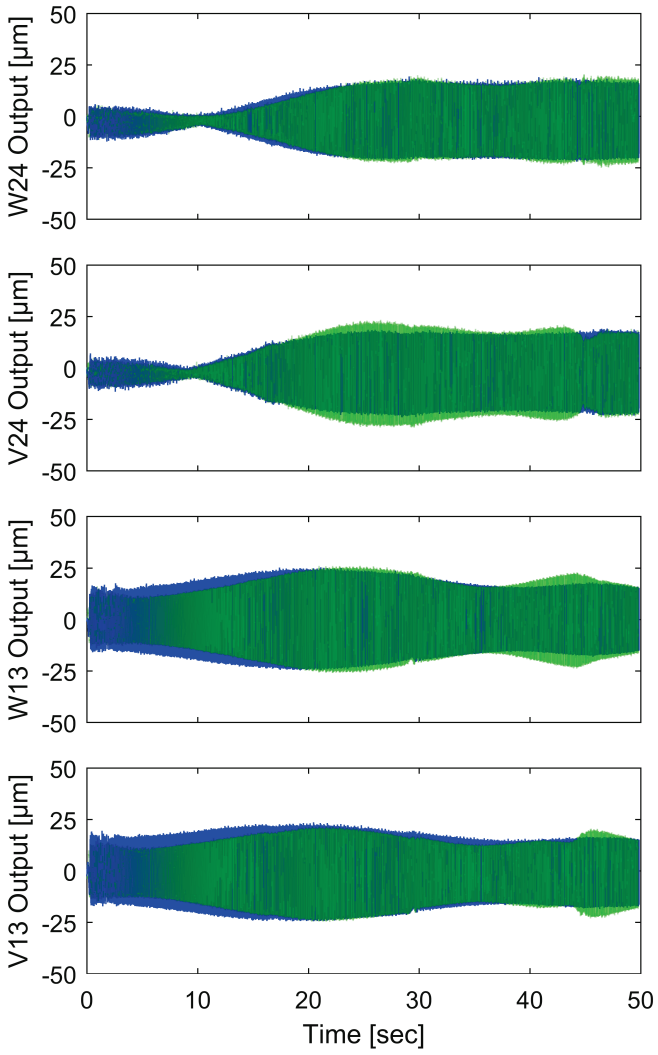

Figure 49: Displacements at AMB sensor positions during the run-up test with K_1 (blue) and K_2 (green)

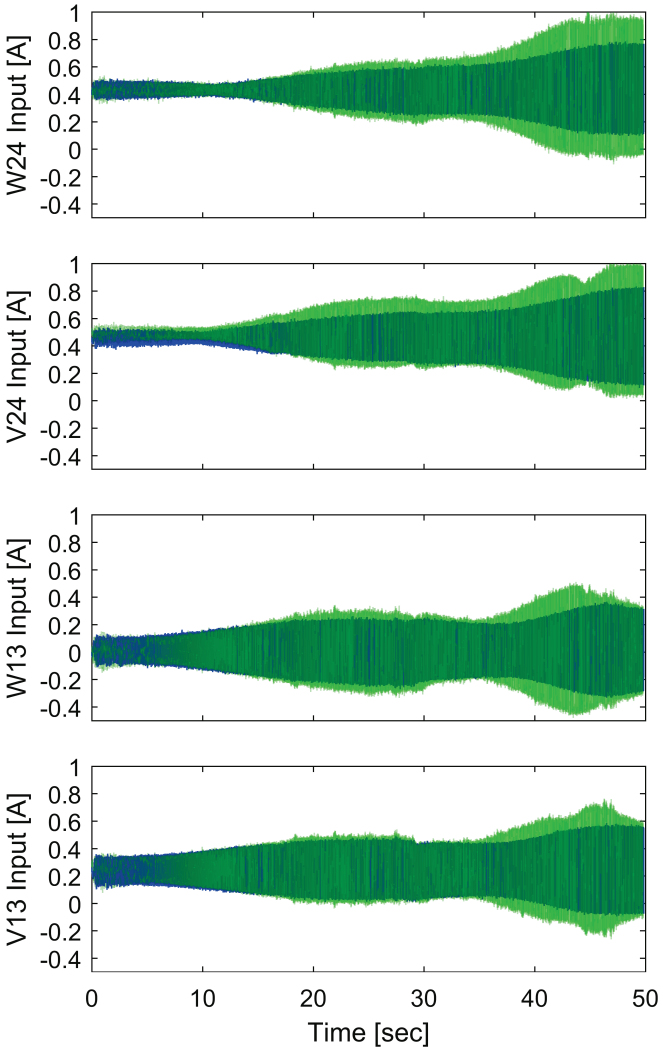

Figure 50: Control currents during the run-up test with K_1 (blue) and K_2 (green)

The steady-state response of the system at various rotational speeds are shown in Figure 51. The orbits confirm the conclusions of the run-up test. Controller K_2 provided better performance up-to 4,000 rpm, i.e., smaller radius orbits. Then, the orbits of both controllers became similar at 6,000 rpm. After 7,000 rpm, controller K_2 degraded in performance, and the performance difference became the largest at 9,000 rpm. At 10,000 rpm, both controllers provided similar performances once again.

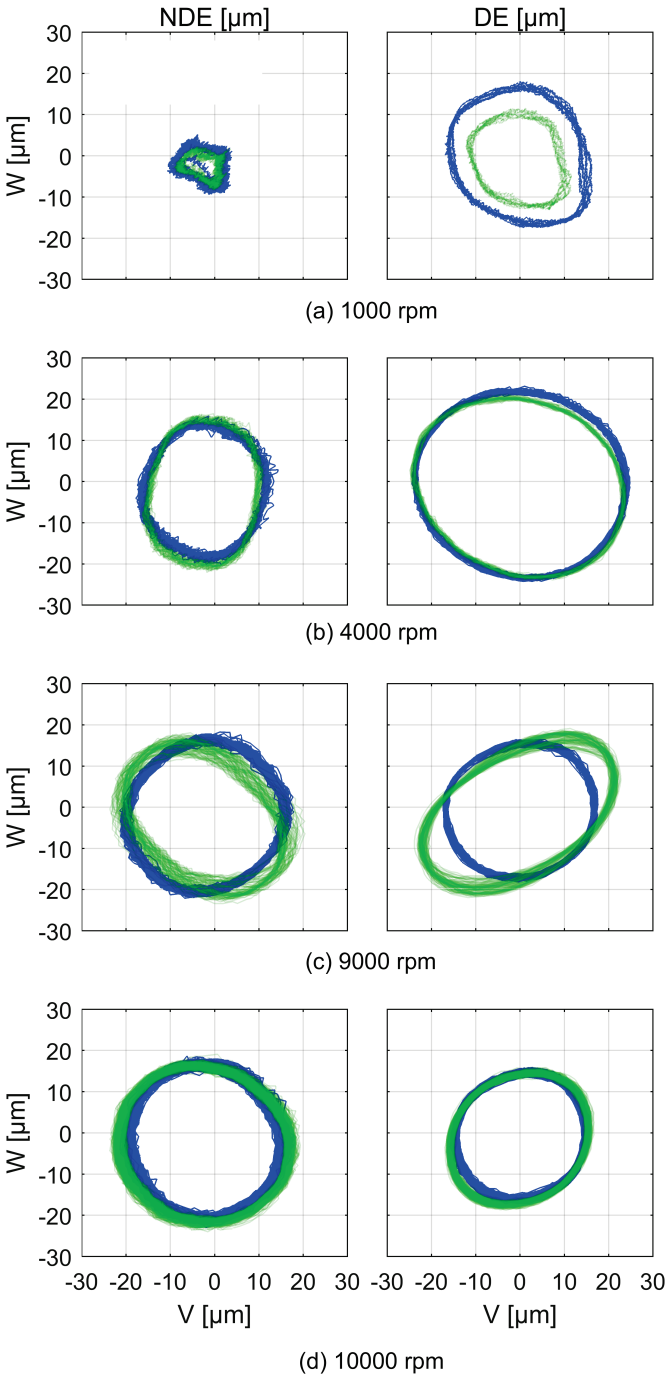

Figure 51: Comparison of orbits at various speeds with K_1 (blue) and K_2 (green)

5.4 Discussion on the Deployment of the Gyroscopic Effect Compensation

The feasibility of gyroscopic effect compensation for flexible rotor-AMB systems to increase achievable performance is investigated. Compensation of gyroscopic effects on selected modes means the bifurcations of the frequencies for the modes are either eliminated or reduced significantly. Hence, the robustness requirements in the control problem formulation can be relaxed, enabling better performance. However, the use of gyroscopic effect compensators not only increase the current magnitudes during operation, hence increasing the power consumption of the system, but also increase the computational cost of implementing the controller. For the system with the add-on controller, the control hardware needs to run both the performance controller and the add-on controller for gyroscopic effect compensation that require the implementation of a relatively high-order state-observer and a modal feedback gain. For comparison, implementation of controller K_1 required 604 MAC operations, where the system matrices were implemented in modal canonical form along with sparse matrix algebra algorithms. On the other hand, controller K_2 required 885 MAC operation with the same implementation method, since it required the algebra for both the controller K_2 and the add-on controller. This implies that the necessary control hardware for the controller K_2 needs to be ~1.5 times more powerful than the control unit for the controller K_1. Moreover, the accuracy of the state-estimation significantly affects the performance of the system, as seen with the controller K_2 where its performance degraded significantly due to errors in the state-estimation between 7,000 rpm and 9,500 rpm. Although the error only affected the performance, it could also cause instability, since the controller K_2

was not designed to be robust to state estimation errors. However since the design of controller K_2 achieved a low μ-value, indicating it could provide robustness to larger than defined uncertainties, the error did not cause instability.

The study does not justify the use of gyroscopic effect compensation to improve the performance of the designed controller by relaxing the robustness requirements. The use of the add-on controller improved the achieved performance at low speeds and gave similar performances at high speeds at the cost of increased power consumption and computational complexity. However, the achieved μ-value with the gyroscopic compensation (0.67) is a lot less than the achieved μ-value with the standard approach (0.94). That is why the performance criteria can be made stricter for the case with gyroscopic effect compensation, which might improve the achieved performance significantly.

A significant performance increase is necessary for the gyroscopic compensation to be valuable. In its current stage, the compensation provides slight performance increase at the cost of increased power consumption and increased computational cost. From a practical point of view, the add-on controller for gyroscopic compensation is not viable.

CHAPTER VI

CONCLUSIONS

6.1 Summary

This research has addressed the high computational cost of generalized MIMO controllers for AMB systems, which is one of the primary barriers for the industry adaptation of model-based robust controllers, and has investigated the effectiveness of add-on controllers for gyroscopic effect compensation on achievable performance.

Two novel methods were developed to reduce the computational cost of controllers while maintaining robust performance; 1) selecting a dual-rate configuration for the controller implementation, and 2) redesign of the controller via identifying and removing unnecessary channels for robust performance in MIMO controllers.

Two approaches were developed for choosing a dual-rate configuration for the controller implementation to achieve maximum computational savings while maintaining robust performance. The first approach used worst-case plant analysis along with lifting technique that is used for multirate system analysis to determine the optimal dual-rate

configuration. Possible dual-rate configurations of the controller were assembled with the worst-case plant model via the lifting technique, and the maximum singular values of the closed-loop systems were calculated to determine the feasibility of each dual-rate configuration. The computational cost of each dual-rate configuration was assessed by calculating the necessary number of MAC operations assuming modal canonical form for the controller system matrices and sparse matrix algebra algorithms for the computations. Then, the optimal dual-rate configuration was selected as the configuration that achieved an acceptable maximum singular value with the least computational cost. The second approach introduced perturbations to the controller and identified the maximum perturbation magnitudes to the controller that would compromise the robust performance. The perturbations defined bounds on the controller response. The responses of the possible dual-rate configurations were then compared to the bounds to assess their robust performance. Then, the optimal dual-rate configuration was chosen as the configuration with the response that stayed within the bounds and required the least number of MAC operations for its matrix-vector algebra. Moreover, the same bounds were used to determine the necessity of each controller channel on achieving robust performance and the controller was redesigned by removing the negligible channels to achieve computational savings.

The developed methods for computational cost reduction were demonstrated on three AMB systems, i.e., AMB test rig, 300 kW turbine generator, and HSM AMB spindle. The results for both dual-rate implementation approaches and the redesign approach achieved computational savings without degrading the performance to unacceptable levels, where the redesign approach provided better computational savings. These

methods for computational savings in controller implementations are applicable to any AMB system and might provide an incentive for the industry to consider using robust controllers for AMB systems.

Moreover, a novel method has been developed to design a modal feedback controller as an add-on controller to compensate the gyroscopic effects at selected modes of a flexible rotor-AMB system. The aim was to increase the achievable performance with robust controller by reducing the robustness requirements in robust control problem formulation. The add-on controller was designed based on the inverse dynamics of the AMB system. The proposed method was first validated on an AMB test rig, where the add-on controller was designed to eliminate the bifurcations due to the gyroscopic effects of the third and fourth flexible modes, individually. The experimental work confirmed the reduction in the bifurcations, hence confirmed the compensation of the gyroscopic effects. Then, the effects of the add-on controller on the achievable performance was investigated on a new AMB system with different rotor configuration. For the new AMB system, the add-on controller was designed to compensate gyroscopic effects of the first and second flexible modes. A robust controller was designed for the new AMB system using a modified model of the system that had reduced gyroscopic effects for its first and second flexible modes. The designed controller with the modified model was compared in performance with a benchmark controller. Some performance improvements were observed at the cost of increased power consumption and computational cost. Also, the necessity for a robust observer was realized. The controller for the case with the add-on controller had the potential to be designed for stricter performance criteria since it

resulted in smaller μ-values compared to the benchmark controller, hence could achieve better performance.

6.2 Future Work

A natural extension to the work on the computational cost reduction via dual-rate implementation is to consider multirate implementations with three or more different rates. This would potentially increase the achievable reduction in computational cost due to the flexibility it provides in implementing each mode of the controller at a carefully chosen rate that is fast enough to obtain accurate response of the mode, but slow enough to achieve computational savings. However, there would be many possible options to analyze and the developed robust performance analysis strategy to select the multirate implementation would take too long. That is why a systematic way of selecting the multirate configuration can be addressed.

One of the shortcomings of the developed strategy for gyroscopic effect compensation is related to the observer design. The developed controller design strategy for gyroscopic effect compensation requires a highly accurate modal state estimation and errors in the modal state estimation results in unexpected performance degradation, as seen in Section 5.3, and might even cause instability. That is why the observer design can be improved via robust observer design techniques that can tolerate parameter variations in the system dynamics, modeling uncertainties and errors in measurements, e.g., the observer design strategies presented in [77-79].

REFERENCES

[1] T. Masuzawa, "Magnetically suspended motor system applied to artificial hearts and blood pumps," *Proceedings of the Institution of Mechanical Engineers, Part I: Journal of Systems and Control Engineering,* vol. 231, no. 5, pp. 330-338, 2016.

[2] A. J. Voigt, C. Mandrup-Poulsen, K. K. Nielsen and I. F. Santos, "Design and Calibration of a Full Scale Active Magnetic Bearing Based Test Facility for Investigating Rotordynamic Properties of Turbomachinery Seals in Multiphase Flow," in *Proceeding of ASME Turbo Expo 2016: Turbomacninery Conference and Exposition (GT2016)* , Seoul, South Korea, 2016.

[3] R. Shultz and A. Narayanaswamy, "Magnetic Bearings for Supercritical CO2 Turbomachinery," in *The 6th Internationl Supercritical CO2 Power Cycles Symposium*, 2018, 2018.

[4] M. Gizelska, "Monitoring and Diagnostics of Special-purpose Turbomachines," *Open Engineering,* vol. 5, pp. 500-508, 2015.

[5] H. Rong and K. Zhou, "Nonlinear zero-bias current control for active magnetic bearing in power magnetically levitated spindle based on adaptive backstepping sliding mode approach," *Proceedings of the Institution of Mechanical Engineers, Part C: Journal of Mechanical Engineering Science,* vol. 231, no. 20, pp. 3753-3765, 2016.

[6] H.-J. Ahn and D.-C. Han, "System modeling and robust control of an AMB spindle: Part I Modeling and validation for robust control," *KSME International Journal,* vol. 17, no. 12, pp. 1844-1854, 2003.

[7] C. R. Knospe, "Active Magnetic Bearings for Machining Applications," *Control Engineering Practice,* vol. 15, no. 3, pp. 307-313, 2007.

[8] R. Gouws, "A review on Active Magnetic Bearing System Limitations, risks of failure and Control Technologies," *Internationl Journal of Engineering & Technology,* vol. 7, no. 4, pp. 6615-6620, 2018.

[9] R. Siva Srinivas, R. Tiwari and C. Kannababu, "Application of active magnetic bearings in flexible rotordynamic systems – A state-of-the-art review," *Mechanical Systems and Signal Processing,* vol. 106, pp. 537-572, 2018.

[10] M. Fujita, K. Hatake and F. Matsumura, "Loop Shaping Based Robust Contorl of a Magnetic Bearing," *IEEE Control Systems Magazine,* vol. 13, no. 4, pp. 57-65, 1993.

[11] A. Noshadi, J. Shi, W. Lee and et al., "High Performance Hinf Control of Non-minimum Phase Active Magnetic Bearing System," in *Proceedings of the 40th annual conference of the IEEE Industrical Electronics Society* , Dallas, TX, USA, 2014.

[12] H. Kang, S. Oh and O. Song, "Hinf Control of a Rotor-magnetic Bearing System Based on Linear Matrix Inequalities," *Journal of Vibration and Control,* vol. 17, no. 2, pp. 291-300, 2011.

[13] I. Kuseyri, "Robust Control and Unbalance Compensation of Rotor/Active Magnetic

Bearing Systems," *Journal of Vibration and Control,* vol. 18, no. 6, pp. 817-832, 2012.

[14] M. Goto, T. Mizuno and I. Takami, "Robust Hinf Control for Active Magnetic Bearing System with Imbalance of the Rotor," in *IEEE 14th International Workshop on Advanced Motion Control*, Auckland, NZ, 2016.

[15] S. Ran, Y. Hu and H. Wu, "Design, Modeling, and Robust Control of the Flexible Rotor to Pass the First Bending Critical Speed with Active Magnetic Bearing," *Advances in Mechanical Engineering,* vol. 10, no. 2, pp. 1-13, 2018.

[16] H. Song, W. Lin, M. Zhou, G. Liu, H. Pan and M. Tong, "Robust Hinf Control for Disturbance Rejection in a Magnetic Levitation Device," in *Proceeding of the IEEE 28th International Symposium on Industrial Electronics*, Vancouver, BC, Canada, 2019.

[17] S. Zhang, C. Wei and J. Wu, "Robust Hinf Controller Based on Multi-objective Genetic Algorithms for Active Magnetic Bearing Applied to Cryogenic Centrifugal Compressor," in *Proceedings of the 29th Chinese Control Conference (CCDC)*, Chongqing, China, 2017.

[18] E. Koroishi, F. A. Lara-Molina, A. S. Borges and V. Steffen Jr, "Robust Control in Rotating Machinery Using Linear Matrix Inequalities," *Journal of Vibration and Control,* vol. 22, no. 17, pp. 1-12, 2015.

[19] E. H. Maslen and J. T. Sawicki, "μ-Synthesis for Magnetic Bearings: Why Use Such a Complicated Tool?,"," in *Proceedings of ASME International Mechanical Engineering Congress & Exposition (IMECE2007)*, Seattle, WA, USA, 2007.

[20] J. T. Sawicki and E. H. Maslen, "Toward Automated AMB Controller Tuning: Progress in Identification and Synthesis," in *The 11th Internationl Symposium on Magnetic Bearing (ISMB-11)*, Nara, Japan, 2008.

[21] J. T. Sawicki, E. H. Maslen and K. R. Bischof, "Modeling and Performance Evaluation of Machining Spindle with Active Magnetic Bearings," *Journal of Mechanical Science and Technology,* vol. 21, no. 6, pp. 847-850, 2007.

[22] W. Ding, Z. Changsheng, T. Ming and Z. Bin, "The Effect of Controllers on the Dynamic Behaviour of a Rotor Supported on Active Magnetic Bearings," in *International Conference on Electrical and Control Engineering*, 2010.

[23] B. Riemann, E. A. Perini, K. L. Cavalca, H. F. de Castro and S. Rinderknecht, "Oil Whip Instability Control Using mu-synthesis Technique on a Magnetic Actuator," *Journal of Sound and Vibration,* vol. 332, no. 4, pp. 654-673, 2013.

[24] I. Arredondo and J. Jugo, "2-DOF Controller Design for Precise Positioning a Spindle Levitated with Active Magnetic Bearings," *European Journal of Control,* vol. 18, no. 2, pp. 194-206, 2012.

[25] S. Skogestad and I. Postlethwaite, Multivariable Feedback Control: Analysis and Design, 2nd ed., Chichester: John Wiley & Sons, 2007.

[26] G. Schweitzer and E. Maslen, Magnetic Bearings: Theory, Design, and Application To Rotating Machinery, New York: Springer, 2009.

[27] M. S. Whorton, H. Buschek and A. J. Calise, "Development of Homotopy

Algorithms for Fixed-Order Mixed H2/H(infinity) Controller Synthesis," NASA TP-3507, 1994.

[28] F. Lösch, *Identification and Automated Controller Design for Active Magnetic Bearing Systems,* Zurich: Diss. ETH. Nr. 14474, 2002.

[29] H. M. N. K. Balini, I. Houtzager, J. Witte and C. W. Scherer , "Subspace identification and robust control of an AMB system," in *American Control Conference*, Baltimoer, MD, USA, 2010.

[30] C. Gahler, M. Mohler and R. Herzog, "Multivariable identification of active magnetic bearing systems," *JSME International Journal Series C Mechanical Systems, Machine Elements and Manufacturing,* vol. 40, no. 4, pp. 584-592, 1997.

[31] A. Noshadi, J. Shi, W. S. Lee, P. Shi and A. Kalam, "System Identification and Robust Control of Multi-Input Multi-Output Active Magnetic Bearing Systems," *IEEE Transactions on Control Systems Technology,* vol. 24, no. 4, pp. 1227-1239, 2016.

[32] A. Wroblewski, J. Sawicki and A. H. Pesch, "Rotor Model Updating and Validation for an Active Magnetic Bearing Based High-Speed Machining Spindle," *ASME Journal of Engineering for Gas Turbines and Power,* pp. 120-136, 2012.

[33] A. Sahinkaya and J. T. Sawicki, "System identification of AMB systems: Steps towards automated Commissioning," in *ISMB16*, Beijing, China, 2018.

[34] A. Sahinkaya and J. T. Sawicki, "Application of Genetic Algorithm for Synthesis of H_∞ Controllers for Active Magnetic Bearing Systems," in *IFToMM 2018*, Rio de Janeiro, 2018.

[35] R. P. Jastrzebski, K. M. Hynynen and A. Smirnov, "H_\infty control of active magnetic suspension," *Mechanical System and Signal Processing,* vol. 24, pp. 995-1006, 2010.

[36] R. Bhattacharya and G. J. Balas, "Control in Computationally Constrained Environment," *IEEE Transactions on Control System Technology,* vol. 17, pp. 589-599, 2009.

[37] P. J. Goddard and K. Glover, "Controller Reduction: Weights for Stability and Perfromance Preservation," in *32nd IEEE Conference on Decision and Control*, San Antonio, TX, USA, 1993.

[38] D. Enns, *Model Reduction for Control Systems Design,* Stanford, CA, USA: Stanford University, 1984.

[39] N. J. M. Van Dijk, N. van de Wou, E. J. J. Doppenberg, H. A. J. Oosterling and H. Nijmeijer, "Robust Active Chatter Cotnrol in the High-Speed Milling Process," *IEEE Transactions on Cotnrol Systems Technology,* vol. 20, no. 4, pp. 901-917, 2012.

[40] R. Fittro and C. Knospe, "Rotor Compliance Minimization Via mu-Control of," *IEEE Transaction on Control System Technology,* vol. 10, no. 2, pp. 238-249, 2002.

[41] A. Pesch, A. Smirnov, O. Pyrhonen and J. T. Sawicki, "Magnetic bearing spindle tool tracking through μ-synthesis robust control," *IEEE/ASSME Transaction on Mechatronics,* vol. 20, pp. 1448-1457, 2015.

[42] P. M. R. Wortelboer and O. H. Bosgra, "Frequency Weighted Closed-Loop Order Reduction in the Control Design Configuration," in *Proceedings of 33rd IEEE Conference on Decision and Control*, 1994.

[43] R. Vuduc, "Automatic Performance Tuning of Sparse Matrix Kernels," University of California, California, Berkley, 2003.

[44] G. Goumas, K. Kourtis and N. Anastopoulos, "Understanding the Performance of Sparse Matrix-Vector Multiplication," in *Proceeding of 16th Euromicro Conference on Parallel, Distributed and Network-Based Processing*, Toulouse, France, 2008.

[45] E. Im, K. Yelick and R. Vuduck, "Sparsity: Optimization Framework for Sparse Matrix Kernels," *International Journal of High Performance Computing Applications,* 2004.

[46] J. Ding, F. Marcassa, S. Wu and M. Tomizuka, "Multirate Control for Computation Saving," *IEEE Transactions on Control Systems Technology,* vol. 14, no. 1, pp. 165-169, 2006.

[47] J. Salt and M. Tomizuka, "Hard Disk Drive Control by Model Based Dual-Rate Controller. Computation Saving by Interlacing," *Mechatronics,* vol. 24, pp. 691-700, 2014.

[48] S. Wu and M. Tomizuka, "Multi-rate Digital Control with Interlacing and Its Application to Hard Disk Drive Servo," in *Proceeding of the 2003 American Control Conference*, Denver, CO, USA, 2003.

[49] T. Chen and B. Francis, Optimal Sampled-Data Systems, New York: Springer-Verlag, 1995.

[50] S. Lopez-Lopez, A. Sideris and J. Yu, "Two-stage H-infinity Optimization Approach to Multirate Controller Design," *International Journal of Autonomous Systems,* vol. 10, no. 4, pp. 675-683, 2012.

[51] S. Rai, G. Cavalier, J. Simonelli and T.-C. Tsao, "MIMO Repetitive Control of an Active Magnetic Bearing Spindle," *IFAC-PaperOnLine,* vol. 49, no. 21, pp. 192-199, 2016.

[52] A. Noshadi, J. Shi, W. Lee, P. Shi and A. Kalam, "Repetitive Disturbance Observer-Based Control for an Active Magnetic Bearing System," in *5th Australian Control Conference (AUCC)*, Gold Coast, QLD, 2015.

[53] P. Cui, S. Li, Q. Wang, Q. Gao, J. Cui and H. Zhang, "Harmonic Current Suppression of an AMB Rotor System at Variable Rotation Speed Based on Multiple Phase-Shift Notch Filters," *IEEE Transactions on Industrial Electronics,* vol. 63, no. 11, pp. 6962-6969, 2016.

[54] Q. Chen, G. Liu and B. Han, "Unbalance Vibration Suppression for AMBs system using Adaptive Notch Filter," *Mechanical Systems and Signal Processing,* vol. 93, pp. 136-150, 2017.

[55] A. Noshadi, J. Shi, W. S. Lee, P. Shi and A. Kalam, "Robust Control of an Active Magnetic Bearing System using Hinfinity and Disturbance Observer-based Control," *Journal of Vibration and Control,* vol. 23, no. 11, pp. 1857-1870, 2017.

[56] Y. Yu, Z. Yang, C. Han and H. Liu, "Disturbance-observer Based Control for

Magnetically Suspended Wheel with Synchronous Noise," *Control Engineering Practice,* vol. 72, pp. 83-89, 2018.

[57] M. Ahrens and L. Kucera, "Cross Feedback Control of a Magnetic Bearing System," in *3rd Internationl Symposium on Magnetic Suspension Technology*, Tallahassee, FL, USA, 1995.

[58] M. Hutterer, M. Hofer and M. Schrödl, "Decoupled Control of an Active Magnetic Bearing System with a High Gyroscopic Rotor," in *IEEE International Conference on Mechatronics*, Nagoya, Japan, 2015.

[59] A. Sahinkaya and J. T. Sawicki, "Cancelling Gyroscopic Effects in AMB Systems with Flexible Rotors via Modal Feedback," in *International Mechanical Engineering Congress and Exposition IMECE 2019-10515*, Salt Lake City, UT, 2019.

[60] A. Sahinkaya and J. T. Sawicki, "Robust Control of AMB Systems with an Add-on Controller to Cancel Gyroscopic Effects, Is It Worth It?," *under review, Journal of Vibration and Control,* 2020.

[61] ISO 14839-3, "Mechanical vibration - Vibration of rotating machinery equipped with active magnetic bearings - Part 3: Evolution of stability margin," International Organization for Standardization ISO, 2006.

[62] M. I. Friswell, J. E. Penny, S. D. Garvey and A. W. Lees, Dynamics of Rotating Machines, Cambridge,UK: Cambridge University Press, 2010.

[63] C. Hatch, G. W. Skingle, C. H. Greaves, N. Lieven, J. E. Coote, M. I. Friswell, J. E. Mottershead, H. Shaverdi, C. Mares, A. McLaughlin, M. Link, N. Piet-Lahanier, M. H. Van Houten, D. Goege and H. Rottmayr, "Methods for Refinement of Structural Finite Element Models: Summary of the GARTEUR AG14 Collaborative Programme," in *32nd European Rotorcraft Forum*, 2006, 2006.

[64] W. K. Gawronski, Dynamics and Control of Structures: A Modal Approach, New York: Springer, 1998.

[65] Y. A. Khulief and M. A. Mohiuddin , "On the Dynamic Analysis of Rotors Using Modal Reduction," *Finite Elements in Analysis and Design,* vol. 26, no. 1, pp. 41-55, 1997.

[66] Y. Wentao, L. Hongwei and L. Shuqin, "The Development of Power Amplifier for the High-Power Magnetic Suspension Bearing Blower," in *International Power, Electronics, and Materials Engineering Conference (IPEMEC 2015)*, Dalian, China, 2015.

[67] R. Khatri, L. Hawkins, M. O. Neri, F. Cangioli and D. Biliotti, "Design and Prototype Test Data for a 300 kW AMB-Supported Turbine Generator for Natural Gas Pressure Letdown," in *ASME Turbo Expo 2019: Turbomachinery Technical Conference and Exposition*, Phoenix, Arizona, USA, 2019.

[68] A. Wroblewski, J. Sawicki and A. H. Pesch, "High-Speed AMB Machining Spindle Model Updating and Validation," in *SPIE Smart Structures/NDE*, San Diego, CA, USA, 2011.

[69] A. Wroblewski, *Model Identification, Updating, and Validation of an Active Magnetic Bearing High-Speed Machining Spindle for Precision Machining*

Operation, Cleveland, OH, USA: Cleveland State University, 2011.

[70] J. C. Doyle, "Analysis of feedback systems with structured uncertainties," *IEEE Proceedingds D - Control Theory and Applications,* vol. 129, no. 6, pp. 242-250, 1982.

[71] M. G. Safonov, "Stability margins of diagonally perturbed multivariable feedback systems," *IEEE Proceedingds D - Control Theory and Applications,* vol. 129, no. 6, pp. 251-256, 1982.

[72] B. C. Moore, "Principal Component Analysis in Linear Systems: Controllability, Observability, and Model Reduction," *IEEE Transactions on Automatic Control,* vol. 26, no. 1, pp. 17-32, 1981.

[73] *MATLAB, Robust Control Toolbox Release 2017b, and Control System Toolbox Release 2017b, The MathWorks, Inc., Natick, Massachusetts, United States.*

[74] S.-C. Wu and M. Tomizuka, "Performance and Aliasing of Multi-rate Digital Controllers with Interlacing," in *Proceedings of the 2004 American Control Conference*, Boston, MA, USA, 2004.

[75] A. Sahinkaya and J. T. Sawicki, "Computationally Efficient Implementation of Robust Controllers in Active Magnetic Bearing Systems," *Mechanical Systems and Signal Processing,* vol. 144, 2020.

[76] A. Sahinkaya, L. Hawkins and J. T. Sawicki, "Computational Cost Reduction of MIMO Controller for Active Magnetic Bearing Systems," *Journal of Engineering for Gas Turbines and Power,* (in press).

[77] Z. Wang, R. S. Schittenhelm and S. Rinderknecht, "Observer Design for Unbalance Excited Rotor Systems with Gyroscopic Effect," in *Proceedings of 2012 IEEE International*, Chenhdu, China, 2012.

[78] S. Battilotti, "Robust Observer Design Under Measurement Noise with Gain Adaptation and Saturated Estimates," *Automatica,* vol. 81, pp. 75-86, 2017.

[79] R. Zhao, Y. Shen, D. Wu and Z. Zhao, "Reduced-Order Set-Valued Observer Design for High Order Uncertain Linear System with Disturbance," in *Proceedings of the 36th Chinese Control Conference*, Dalian, China, 2017.

[80] N. J. M. Van Dijk, N. van de Wouw, E. J. J. Doppenberg and H. A. J. Oosterling, "Robust Active Chatter Control in the High-Speed Milling Process," *IEEE Transactions on Control Systems Technology,* vol. 20, no. 4, pp. 901-917, 2012.

[81] W. M. H. Heemels, J. Daafouz and G. Millerioux, "Observer-based Control of Discrete-Time LPV Systems with Uncertain Parameters," *IEEE Transactions on Automatic Control,* vol. 55, no. 9, pp. 2130-2135, 2010.